



**Search for New Massive Long-Lived Neutral Particles  
decaying to Photons in  $pp$  Collisions at  $\sqrt{S} = 8$  TeV**

A DISSERTATION  
SUBMITTED TO THE FACULTY OF THE GRADUATE SCHOOL  
OF THE UNIVERSITY OF MINNESOTA  
BY

Tambe Ebai Norbert

IN PARTIAL FULFILLMENT OF THE REQUIREMENTS  
FOR THE DEGREE OF  
Doctor of Philosophy

Prof. Yuichi Kubota

June, 2015

**© Tambe Ebai Norbert 2015  
ALL RIGHTS RESERVED**

# Acknowledgements

There are many people that have earned my gratitude for their contribution to my time in graduate school.

I want to thank my supervisor Prof. Yuichi Kubota, who gave me countless failure-tolerant opportunities throughout my PhD. Before I knew him, the fear of failure always did paralyzed me, not anymore.

*The universe is unbiased, she chooses to reveal herself to all who have the correct attitude.*

Tambe E. Norbert

*So I would claim you are profoundly misled by thinking about physics as similar to logic or number theory. Its not! its dynamical evolution, and most results of physics problems are not nice numbers like 1 or  $\pi$  or even  $e^\pi$ .*

by Prof. Matt Strassler

# Dedication

*No, I have nothing against Mr. Einstein. He is a kind person and has done many good things, some of which will become part of the music. I will write to him and try to explain that the ether exists, and that its particles are what keep the Universe in harmony, and the life in eternity.*

Nikola Tesla

*The Universe is unbiased, she chooses to reveal herself to whomever she wants.*

Tambe E. Norbert

## Abstract

We performed a search for delayed photons produced during proton-proton collisions with center of mass energy,  $\sqrt{S} = 8$  TeV. We use timing measurements made using the electromagnetic calorimeter to search for these delayed photons. In the absence of excess events over standard model prediction, we produce limits on the cross section,  $\sigma_{\tilde{\chi}_1^0} > 0.02$  pb, for the production and decay of the lightest neutralino,  $\tilde{\chi}_1^0$ , with mass,  $m_{\tilde{\chi}_1^0} \geq 235$  GeV/ $c^2$ , and lifetime,  $\tau_{\tilde{\chi}_1^0} \geq 35$  ns, as described in supersymmetry. We also show that using only timing information of the CMS electromagnetic calorimeter as observable, the CMS detector is sensitive to neutralino with lifetime up to 30 ns and mass,  $m_{\tilde{\chi}_1^0} \approx 260$  GeV/ $c^2$ . Description of how the electromagnetic calorimeter is used to make timing measurements and its performance is presented.

# Contents

<b>Acknowledgements</b>	<b>i</b>
<b>Dedication</b>	<b>ii</b>
<b>Abstract</b>	<b>iii</b>
<b>List of Tables</b>	<b>vii</b>
<b>List of Figures</b>	<b>ix</b>
<b>1 Introduction</b>	<b>1</b>
<b>2 Phenomenology of Long-Lived Particles</b>	<b>6</b>
2.1 The Standard Model of Particle Physics . . . . .	6
2.1.1 Main Components of the SM . . . . .	7
2.1.2 Spontaneous Symmetry Breaking . . . . .	13
2.1.3 Limitations of the Standard Model . . . . .	16
2.2 Beyond Standard Model Physics . . . . .	17
2.2.1 Supersymmetry . . . . .	18
2.2.2 Minimal Supersymmetric Standard Model . . . . .	19
2.3 Gauge Mediated Supersymmetry Breaking Models . . . . .	23
2.3.1 Phenomenology . . . . .	23
2.3.2 Long-Lived Particles in GMSB Models . . . . .	25
2.4 Previous Search Experiments . . . . .	33

<b>3 Hadron Collider and Detector</b>	<b>34</b>
3.1 Large Hadron Collider . . . . .	34
3.1.1 Overview . . . . .	34
3.1.2 Colliding Energy . . . . .	35
3.1.3 Luminosity . . . . .	36
3.1.4 LHC Bunch Structure . . . . .	37
3.2 Compact Muon Solenoid . . . . .	41
3.2.1 Overview . . . . .	41
3.2.2 Calorimeter . . . . .	43
3.2.3 Muon Chambers . . . . .	48
3.2.4 Triggering . . . . .	50
<b>4 Time Reconstruction and Resolution</b>	<b>51</b>
4.1 Electromagnetic Calorimeter Readout Electronics . . . . .	52
4.2 Time Reconstruction . . . . .	54
4.3 ECAL Time Performance from Test Beam . . . . .	55
4.3.1 ECAL Time Resolution . . . . .	55
4.4 ECAL Time Performance from Collision . . . . .	58
4.4.1 Time Calibrations . . . . .	58
4.4.2 Time Bias . . . . .	64
4.4.3 ECAL Time Performance With Z Events . . . . .	66
<b>5 Event Reconstruction</b>	<b>70</b>
5.1 Event Reconstruction Overview . . . . .	70
5.2 Supercluster Reconstruction . . . . .	70
5.3 Track and Vertex Reconstruction . . . . .	72
5.4 Photon and Electron Reconstruction . . . . .	73
5.5 Muon Reconstruction . . . . .	76
5.6 Jet Reconstruction . . . . .	78
5.7 Missing Transverse Energy Reconstruction . . . . .	79
5.8 Anomalous Signals . . . . .	80

<b>6 Search Analysis for Long-Lived Particles</b>	<b>82</b>
6.1 Analysis Strategy . . . . .	82
6.1.1 Signal and Background Modelling . . . . .	84
6.1.2 Datasets . . . . .	85
6.2 Event Selection . . . . .	87
6.2.1 Trigger . . . . .	89
6.2.2 Offline Selection . . . . .	90
6.2.3 ECAL Time . . . . .	93
6.3 Background Estimation . . . . .	98
6.3.1 Non-Collision Backgrounds . . . . .	100
6.3.2 Collision Backgrounds . . . . .	106
6.3.3 Event Cleaning, Veto Performance and Fake Rate . . . . .	106
6.3.4 Background Estimation Cross Check . . . . .	111
6.4 Results . . . . .	116
6.5 Systematic Studies . . . . .	117
<b>7 Statistical Analysis</b>	<b>119</b>
7.1 Limit Computation . . . . .	119
7.1.1 CLs Technique . . . . .	120
7.1.2 Statistical Test Formalism . . . . .	121
7.1.3 Test Statistics and $p$ -values . . . . .	123
<b>8 Limit Interpretation</b>	<b>127</b>
8.1 Signal Efficiency and Acceptance . . . . .	127
<b>9 Conclusion</b>	<b>132</b>
<b>Bibliography</b>	<b>133</b>
<b>Appendix A. Glossary and Acronyms</b>	<b>138</b>
A.1 Glossary . . . . .	138
A.2 Acronyms . . . . .	138

# List of Tables

2.1	SM particles and their gauge multiplets(representation) with quantum numbers. the numbers for example ( <b>3</b> , <b>2</b> , $\frac{1}{6}$ ) means ( <i>triplet, doublet, Y = 1/6</i> ) representations. . . . .	13
2.2	Supermultiplets and particle spin in SM and Supersymmetry. . . . .	19
2.3	Chiral supermultiplets and representation in Minimal Supersymmetric SM (MSSM). Super symmetric particles (sparticles) have a $\sim$ on them. Spin -0 fields are complex scalars while spin-1/2 fields are left-handed two component Weyl fermions. . . . .	20
2.4	Gauge supermultiplets and representations in Minimal Supersymmetric SM (MSSM). Super symmetric particles (sparticles) have a $\sim$ on them. . . . .	20
3.1	LHC operation parameter conditions during RUN 1, 2010-2013 . . . . .	40
3.2	CMS detector material, Ref.[22], and resolution(Time resolution: $N \approx 35$ ns, $\bar{C} \approx 0.070$ ns Ref. [39]) . . . . .	43
4.1	ECAL timing resolution absolute time and single precision for 2011 and 2012 of LHC Run 1 . . . . .	69
5.1	Simple cut-based selection criteria for electron and photon identification. . . . .	76
6.1	Dataset and corresponding integrated luminosity totaling $19.1 \text{ fb}^{-1}$ used in this analysis . . . . .	86
6.2	The signal GMSB SPS8 MC samples for difference $\Delta$ and Branching Ratios used in this analysis . . . . .	87
6.3	The $\gamma +$ jets samples used in this analysis . . . . .	87
6.4	The photon identification and selection criteria used in this analysis . . . . .	91
6.5	The Jet ID selection used in this analysis . . . . .	92
6.6	Fake rates for different non-collision cleaning. . . . .	107

6.7	ABCD Control Regions (CRs) for estimating non-collision background. . . . .	109
6.8	$A' B' C' D'$ and $I' I''$ CRs for estimating collision background. . . . .	109
6.9	Result from closure test of background estimation technique using 0 and 1-jet events. Numbers in bracket represent our expected background estimate using ABCD method. . . . .	111
6.10	Result of observed events and estimated background from signal sample, events with at least 2-jets. Numbers in bracket represent our observed number of events while numbers not in bracket are our expected number of background events estimated using ABCD method. . . . .	116
6.11	Final number for $\Lambda = 180$ TeV GMSB SPS8 MC signal events events passing our selection cuts. . . . .	117
6.12	Summary of systematic uncertainties used in this analysis and applied to our cross-section upper limit, $\sigma_{UL}$ calculation. . . . .	118
A.1	Acronyms . . . . .	139

# List of Figures

2.1	Higgs boson ‘‘Mexican hat’’ potential, $V(\phi^*\phi) = \mu^2(\phi^*\phi) + \lambda(\phi^*\phi)^2$ , which leads to spontaneous symmetry breaking with choice of parameters $\mu^2 < 0, \lambda > 0$ . . . . .	15
2.2	SM particles and their interactions with vector bosons as mediators. . . . .	15
2.3	Higgs mass contributions from its coupling to fermions (a) and scalar (b) fields. . . . .	17
2.4	Supersymmetry particle mass spectra in the SPS8 or minimal GMSB (mGMSB) model. . . . .	22
2.5	Feynman diagrams of gravitino/golstino, $\tilde{G}$ , gaugino and scalar interactions with superpartner pairs $(\psi, \phi)$ scalar (a) and $(\lambda, A)$ gaugino (b) decay to gravitino. . . . .	24
2.6	Supersymmetry production cross-section against sparticle mass for different modes of supersymmetry production at a proton-proton collider. $pp \rightarrow \tilde{g}\tilde{g}$ processes have the dominant production cross section. . . . .	26
2.7	Feynmann diagrams for neutralino production from the cascade decay of a produced gluino ( <i>top</i> ) and squark ( <i>bottom</i> ). The final event has a single ( <i>left diagrams</i> ) or double photons ( <i>right diagrams</i> ) neutralino decay at LHC. . . . .	28
2.8	Neutralino transverse momentum distribution( <i>top left</i> ) and proper decay length( <i>top right</i> ) with its decayed photon transverse momentum distribution( <i>bottom left</i> ) and time of arrival at ECAL( <i>Bottom right</i> ) for GMSB SPS8 model. . . . .	32
2.9	Neutralino lifetime and mass upper limit from ATLAS(left) and CMS(right) 7 TeV analysis with non-pointing photons and MET. . . . .	33
3.1	Schematic diagram showing the full Large hadron Collider. . . . .	35

3.2	Cumulative luminosity versus day delivered to (blue), and recorded by CMS (orange) during stable beams and for p-p collisions at 8 TeV center-of-mass energy in 2012. . . . .	37
3.3	Longitudinal Profile taken with Longitudinal Density Monitor (LDM) detector showing definition of Ghost/Satellite bunches with respect to main bunches. . . . .	38
3.4	(left)Arrival time distribution(red) of ATLAS MBTS for LHC fill 1533 during 2010 Pb-Pb run and LDM profile(black) for Beam2(same for Beam1). (Right) Timing of Clusters in the CMS endcap calorimeters for fill 1089:Left: EEP detector(left side of IP $z > 0$ ) Right: EEM detector( right side of IP, $z < 0$ ). Plots from ATLAS Ref.[30] and CMS, Ref.[31] . . . . .	39
3.5	CMS Detector showing the different subdetectors and their material. . .	42
3.6	CMS detector schematic view with definition of $x - y - z$ coordinates. .	42
3.7	Schematic diagram of CMS calorimetry system with HCAL enclosing ECAL in the Barrel and Endcap regions. . . . .	44
3.8	Layout of the CMS electromagnetic calorimeter showing the arrangement of crystal modules, supermodules in the barrel with the preshower in front of endcap with supercrystals. . . . .	49
3.9	Cross section view showing the coverage range of CMS sub-detectors and their longitudinal distance from the IP. . . . .	49
4.1	Schematic diagram of the CMS ECAL electronics readout. . . . .	53
4.2	(a) A measured ECAL pulse shape for a single channel. (b) $T - T_{MAX}$ Vs $R(T)$ showing the distribution of $T(R)$ . Solid line is pulse shape from test beam while dots are the 10 discrete samples corresponding to signal from proton-proton collision. . . . .	54
4.3	Deviation of the time difference as a function of $A_{eff}/\sigma_n$ of two crystals sharing an energy and belonging to the same electromagnetic shower obtained during electron testbeam measurements. The single crystal energy scales for barrel (EB) and endcap (EE) is overlaid. The fitted results give $N = (35.1 \pm 0.2)$ ns and $\bar{C} = (20 \pm 4)$ ns. . . . .	57

4.4	<i>Top 3:</i> Time calibration maps showing the distribution of mean time for each channel/PbWO <sub>4</sub> crystal in EB (top) and EE (below: EE-(left), EE+(right)) before calibration. <i>Bottom 3:</i> Time calibration maps showing the distribution of mean time after calibration. After calibration most crystals have an average time of zero(GREEN). . . . .	61
4.5	<i>Top:</i> The mean time distribution obtained from laser of crystals in a single FED i.e. EB±8. <i>Bottom:</i> Clock and Control Unit (CCU) mean time shift distribution of FEDs EE+ and EE-. $\Delta t_{CCU}$ distributions after the global shift has been removed. The adjustment for global time shift per FED due to difference in light source for each CCU has been shown to reduce the possibility of CCU showing false time shift. . . . .	64
4.6	Distribution of mean time ( $\mu$ , <i>top row</i> ) and time deviation ( $\sigma$ , <i>bottom row</i> ) as a function of crystal energy for EB prior (left) and after (right) time bias corrections depending on energy have been applied. . . . .	65
4.7	Distribution of the time standard deviation ( $\sigma$ ) against crystal geometrical position, $\eta$ , in the ECAL barrel. Almost flat distribution of $\sigma$ with $\eta$ . . . . .	66
4.8	Ecal time difference between the two reconstructed electrons in $Z \rightarrow e^-e^+$ decay. The electron time is the seed (crystal with highest energy deposit) time with additional correction due to the time of flight of the electron in EB and EE . . . . .	67
4.9	Ecal absolute time of a single reconstructed electron in $Z \rightarrow e^-e^+$ decay. The electron time is the seed (crystal with highest energy deposit)time of the electron in EB and EE . . . . .	68
4.10	Timing resolution from: <i>left:</i> Two most energetic crystals in the same readout unit, <i>right:</i> Two most energetic crystals belonging to different readout units, as a function of effective amplitude( $A_{eff} = A_1 A_2 / \sqrt{A_1^2 + A_2^2}$ ) normalized to noise in EB. Both crystals are from reconstructed electrons in $Z \rightarrow e^-e^+$ events. . . . .	69
5.1	Superclustering algorithm direction in the $(\eta, \phi)$ plane in EB and fraction of electromagnetic shower energy coverage in a crystal energy matrix. . .	71

5.2	Z mass distribution from $Z \rightarrow e^+e^-$ decay showing improvement in the measurement of the Z mass after performing energy adjustments to account for intrinsic spread in crystal, photo-detector response and time-dependent corrections to compensate for channel response loss for EB (right) and EE (left) . . . . .	74
5.3	Z mass reconstructed using electron superclusters shows improvement in Z mass measurement after applying energy adjustment at superclusters for EB (right) and EE (left). . . . .	75
5.4	Illustration of muons from proton-proton collision, cosmic rays and beam halo. (a) Muons from collision propagating from the center and moving outwards, (b) Cosmic muons traveling through the detector leaving signals in opposite hemispheres of the muon system, (c) Cosmic muons leaving signals in the tracker and opposite hemispheres, (d) cosmic muons entering and leaving the detector without passing through the muon detector layers, (e) beam halo muons penetrating the detector and leaving signals in the endcaps and (f) Cosmic muons entering the detector through the endcap and leaving through the barrel and which can happen in a <i>vice-versa</i> manner. . . . .	77
6.1	Schematic diagram showing $\tilde{\chi}_1^0 \rightarrow \gamma + \tilde{G}$ decay topology within the ECAL volume of the CMS detector. Proton beams are also shown showing the possible production of collision and non-collision delayed photons . . . . .	89
6.2	Trigger efficiency turn-on curves for photon $p_T$ and $E_T^{\text{miss}} > 25$ GeV (left) and for $E_T^{\text{miss}}$ with photon $pt > 80$ GeV/c (right). The $\gamma +$ jets samples require photon $p_T > 170$ GeV/c for selecting events with true $E_T^{\text{miss}}$ . . . . .	90
6.3	Pulse shape profile showing a spike (solid line) and a real photon (dashed line) from data. . . . .	93
6.4	Timing distribution of photons showing timing measurements using seed crystal (black) and using Weighted Average basic cluster time (blue). Resolution ( $\sigma$ ) from seed time is better compared to that for cluster time which is computationally intensive. Together with the $\chi^2$ , the seed time performs better in identifying anomalous timing objects. . . . .	94

6.5	Timing distribution of photons showing timing of data and MC $\gamma+$ jets (blue) samples and data (red) before (left) and after (right) timing Calibration is applied to MC. . . . .	95
6.6	ECAL timing distribution of photons in barrel ( <b>EB</b> ), endcap ( <b>EE</b> ) and all of ECAL (ALL ECAL) with $p_T > 50$ GeV from data. A 2.5 ns delay timing structure is observed in endcap subdetector. . . . .	96
6.7	Sources of delayed photons produced from neutralino decay in the SPS8 model with $\Lambda = 180$ TeV and $c\tau = 6000$ mm arriving at ECAL. . . . .	97
6.8	ECAL time against $\eta$ (left) and ECAL time against $\phi$ (right) for photons with $p_T > 60$ GeV from data. The lower plot shows the photon timing distribution for events with different jet multiplicity. . . . .	99
6.9	ECAL time Vs $\eta$ (left) and ECAL time Vs $\phi$ (right) and $CSC(Seg, \gamma)\Delta\phi$ for photons with $p_T > 80$ GeV from data. Halo photons show a clear matched between CSC segments and ECAL cluster in $\Delta\phi$ with their distribution peaking at $\phi = 0, \pm\pi$ and also the shape of their expected time. . . . .	103
6.10	2 dimensional plot showing $DT\Delta\eta(Seg, \gamma)$ against $DT\Delta\phi(Seg, \gamma)$ for photons with $p_T > 80$ GeV, ECAL Time, $t_\gamma > 2$ ns and ECAL Time $t_\gamma < -3$ ns from proton-proton collision data (left) and pure cosmic muon data (right). Small $\Delta\eta$ and $\Delta\phi$ are cosmic photon candidates. . .	104
6.11	Plot showing <i>number of crystals</i> in photon supercluster for photons from the region with ECAL Time, $t_\gamma < 0$ ns. Figure shows the timing distribution of candidate true photons(black), spike candidate photons (magenta) and halo candidate photons (red). The toplogical swiss-cross variable ( $1-E_4/E_1$ ) distribution is shown comparing true photons ( $ t_\gamma  < 1.0$ ) to spike populated sample. . . . .	105
6.12	Residual Background after tagging the different non-collision background sources using the methods described in text. . . . .	108

6.13 ECAL time, $t_\gamma$ Vs $\eta_\gamma$ (top) and $t_\gamma$ Vs $\phi$ (bottom) for photons from <b>SinglePhoton</b> dataset (left) compared to electron candidates from the <b>DoubleElectron</b> dataset (right). All photons or electron candidates are in barrel subdetector. Most of the photons with $\phi = 0, \pm\pi$ are halo photons which are not observed in the $Z$ boson candidate sample. . . . .	112
6.14 Di-electron candidate mass distribution and the time of both electrons for the signal $76 < m_Z < 100$ GeV/ $c^2$ $Z$ boson sample(left) and similar distributions from the Control ( $50 < m_Z < 76$ GeV/ $c^2$ and $100 < m_Z < 130$ GeV/ $c^2$ ) sample (right). Candidates events from the DoubleElectron dataset. . . . .	113
6.15 <i>Top</i> : Control sample (left) and signal sample (right) of di-electron candidate mass distribution. <i>Bottom</i> : Figure showing definition of scale factor use in estimating the contributions from control sample in signal sample.	115
6.16 Timing distribution of genuine $Z$ bosons after background contribution has been subtracted. . . . .	116
7.1 Sampling distributions for $f(t_\mu \mu)$ showing how one extracts the $p$ -vlaues. left: is the using a analytic of the Asymptotic method and right: is from the HybridNew method. . . . .	124
7.2 Distribution of $p$ -vlaues showing how upper limit on $\mu$ is extracted for a given threshold probability. . . . .	126
8.1 The reconstruction and selection efficiency (left) $\times$ Acceptance ( $t > 3$ ns) (right) against transverse decay length in laboratory frame for different $c\tau$ points. . . . .	128
8.2 Neutralino production cross section against proper delay length upper limit interpretation in SPS8 model. (Left) $\Lambda = 100$ TeV, (Right)(left) $\Lambda = 180$ TeV . . . . .	129
8.3 Neutralino production cross section against neutralino mass upper limit at 95% confidence levels interpretation in SPS8 model.(Left) $C\tau = 11000$ mm, (Right) $C\tau = 6000$ mm . . . . .	130
8.4 Neutralino two dimensional exclusion limit of neutralino mass ( $\Lambda$ ) against proper delay length upper limit interpretation in SPS8 model in the decay $\tilde{\chi}_1^0 \rightarrow \gamma + \tilde{G}$ with limits from previous experiments shown. . . . .	131

# Chapter 1

## Introduction

Many indirect observations at astronomical and cosmological scales[1], indicate the presence of a new form of matter in the universe, which only interacts significantly through gravity. This illusive matter which cannot emit or scatter electromagnetic radiation is called *Dark Matter* (DM). The supposed existence of dark matter is one of the strongest indications for a new kind of physics beyond the standard model of particle physics, as no known particles can be attributed to dark matter. Visible matter make up only 4.5% of the total matter in the universe and is best described using simple symmetries known as gauge symmetries. These gauge symmetries are expressed in a mathematical model called the *Standard Model* (SM). The SM describes with unmatched precision, the interactions and properties of the entire visible matter. Despite the unprecedented success of the SM amongst scientific models, it cannot describe dark matter which make up the larger percentage of the matter in our universe. There have been numerous experimental reports on the discovery of particles predicted by the SM. On the other hand, there have been no reports on direct detection of the particles which make up dark matter. On the nature of DM, results from theoretical models and numerical N-body simulations [2], support speculation that dark matter could be made up of particles which are neutral and stable i.e. have lifetime comparable to the age of our universe. There are also suggestions that dark matter particles could be produced from the disintegration (decay) of other meta-stable particles called *Long-Lived* (LL) particles [3]. Long-lived particles can either be charged or neutral (i.e cannot interact with light in the context of the SM).

There is significant interest towards neutral dark matter particles, since dark matter does not interact with light. A good amount of effort is directed towards the search for dark matter particles produced from the decay of *neutral long-lived* particles[4]. Experimental techniques for detecting neutral particles is limited and so new methods to search and detect dark matter particles are constantly being developed.

The search for dark matter particles covers a wide range of experiments, from deep space search experiments like the Hubble and James Webb Space Telescope experiments, the Alpha Magnetic Spectrometer detector on board the International Space Station of NASA, ground based particle detector experiments like the Super Cryogenic Dark Matter Search experiment which try to detect dark matter particles produced in cosmic rays, to collider experiments like the Large Hadron Collider (LHC) of the European National Laboratory for Nuclear Research in Geneva, Switzerland, where dark matter particles can be produced during particle collisions. The interest in collider experiments is base on theoretical model predictions that dark matter particles or particles which decay into dark matter particles can be produced in a collider like the LHC, provided there is sufficient center-of-mass energy. These models are extensions of the standard model to allow for the existence of new fundamental particles. The models are called *Beyond Standard Models* (BSM) and there are several of them. *Supersymmetry* is a BSM which extends the gauge symmetries to a much larger family of symmetries and allows for the doubling of the particles in the SM to include a wide variety of new fundamental particles which can be dark matter particles[3, 4]. A particular branch of supersymmetry models called Gauge Mediating Supersymmetry Breaking (GMSB) models, predict the production of new, massive, meta-stable, neutral, weakly interacting and long-lived particles which can decay into a candidate dark matter particle and isolated energetic photons. The candidate dark matter particle is stable and also neutral and weakly interacting. It has a lifetime comparable to the age of the universe. Detecting photons from the decay of a supersymmetry neutral and weakly interacting long-lived particle will be an indication of new particles, as there are no neutral, weakly interacting and long-lived particles which decay into photons in the SM. Numerous previous experiments have searched for these photons. Often, the results from these experiments have been negative. Nevertheless, new experiments with new detection techniques and clever search

methods depending on the manner of production and decay of these new particles are continuously being developed. We will refer to such new, massive, weakly interacting and neutral long-lived particles which decay into isolated photons and candidate dark matter particles as *Neutral Massive Long-Lived Particles* (NMLLP).

Our search analysis is motivated by the classic signature of a delayed photon from the decay of a NMLLP in GMSB models, produced in the LHC proton collider. The decay products of the NMLLP are detected using the multi-purpose Compact Muon Solenoid (CMS) particle detector. We consider the NMLLP to be the Next-To-Lightest Supersymmetric Particle (NLSP) called the *lightest neutralino* ( $\tilde{\chi}_1^0$ ). This lightest neutralino decays into a photon and the Lightest Supersymmetric Particle (LSP) called the gravitino ( $\tilde{G}$ ). The gravitino is neutral and weakly interacting with visible matter, and being the LSP makes it stable. These properties make the gravitino a good dark matter particle.. The neutralino decay can in general be instantaneous (prompt) or *delayed* depending on the choice of parameters in the neutralino decay model. In a subset of models called *R-Parity Conserving* (RPC) GMSB models, supersymmetry particles are pair produced either, directly during particle collisions, or from the cascade decay of higher massive supersymmetry particles produced also in particle collisions. As a result, in these models, the LSP is very stable and automatically a dark matter candidate particle while the NLSP (neutralino) is often long-lived and the photons are energetic, isolated and often delayed in their arrival time at a detector. These often delayed photons can be detected using the electromagnetic calorimeter (ECAL) of the CMS detector. The ECAL has an excellent timing resolution better than a *nanosecond* (ns). In cases where the neutralino is produced from the cascade decay of higher massive particles, large transverse momentum ( $p_T$ ) spray of hadronic particles collectively called jets are also part of the neutralino production and decay event. Since the gravitino is weakly interacting with the detector material, it is undetected. The gravitino presence is inferred using *missing transverse momentum* which in combination with the transverse momenta of the jets and photons should conserve the total momentum of the event in the transverse plane of the detector. In the decay scenario of the neutralino where its lifetime is large, say above, 3 ns, the photon is delayed and its

measured arrival time is large (many nanoseconds (ns)). This is because of the inherently long neutralino lifetime and the extra distance it has to travel inside the detector before it decays. Finding an event, with the combination of jets, missing transverse momentum and at least a delayed photon is a clear signal for new particles not known in the standard model (SM). The CMS detector is located in the LHC tunnel at one of the proton bunch crossing points also known as *Interaction Point* (IP). We measure the arrival time of the photon from the IP to the surface of the ECAL. Relying on the excellent timing and energy resolution of the ECAL, we can distinguish between high energy photons from the decay of a NMILP from those produced by the SM which are often prompt and not delayed. To ensure this excellent timing resolution, the ECAL detector is continuously time calibrated throughout the entire LHC proton-proton collision year. We will describe in future chapters how the ECAL timing alignment is done to realize this excellent timing resolution. Observation of a delayed photon event at the LHC using ECAL timing measurements, will confirm the existence of NMILPs and will help answer important questions in particle physics like: What is the source and nature of dark matter?, Is there any reason why known SM particles are classified into 3 generations and have very different masses as known? Why do we observe so much matter compared to anti-matter in our universe? Is there a single universe or multi-verses? Answers to these questions will provide a clear understanding and direction for future research in physics beyond the SM.

In this thesis, we have described our search for a NMILP decaying to a photon using arrival time information of the photon to the ECAL and use this information to distinguish between the signal from new long-lived particles and background from SM interactions. Our search analysis uses data recorded using the CMS detector produced from proton-proton ( $pp$ ) collisions at the Large Hadron Collider (LHC) with a center-of-mass energy  $\sqrt{S} = 8 \text{ TeV}$ . The contents of this thesis is arranged beginning with this introduction as chapter 1, followed by chapter 2, which gives a brief description of the SM, highlighting its strengths and weaknesses which motivates why we need to go beyond the SM in our efforts to understand the universe. The study *supersymmetry* as our BSM physics model, paying particular attention to GMSB models which allows for the existence of NMILP which can decay into a photon and a gravitino with jets

in the associate event. In Chapter 3, we describe the LHC and CMS particle detector, dueling only on the sub-detectors which have been used in our search analysis. How timing measurements of a particle are made by the ECAL sub-detector is described in chapter 4. The reconstruction of a full event with its constituent particles is described in chapter 5 with the definition of quantities like jets and missing transverse energy ( $E_T^{\text{miss}}$ ) according to the CMS standards is described. Anomalous signals called *spikes* observed in the ECAL is mentioned. Our search strategy is described in chapter 6 with details of which datasets and triggers we have used, what is trigger efficiency, our choice of search observable, event selection and background estimation techniques used. We describe the various systematic sources considered and their contribution to our search result is presented in this chapter. Chapter 7 presents the statistical and analysis methods used with clear meaning of  $p$ -values as used in our analysis. The cross section times branching ratio limits depending on the lifetime and mass of the production and decay of a NMILP using the minimal *Gauge Mediating Supersymmetric Model*, with *Snowmass Signal Point 8* (SPS8) as our benchmark model is presented in chapter 8. The interpretation of our results in terms of exclusion regions reached by our analysis is also presented in this chapter. Chapter 9 covers the conclusion.

## Chapter 2

# Phenomenology of Long-Lived Particles

### 2.1 The Standard Model of Particle Physics

The Standard Model (SM) of particle physics provides a thorough and experimentally verified mathematical model description of the fundamental constituents of visible matter and its interactions (except gravity) in the universe. Predictions of particle properties and interactions by the SM agree with most of the available experimental data with unmatched precision.

Despite the numerous success of the SM, there are some theoretical and experimental inconsistencies with the SM such as the observation of Dark Matter (DM) in the universe which is indescribable by the SM, the observation of neutrino oscillation and neutrino masses unexplained by the SM and the absence of gravitational interactions in the SM. These shortcomings of the SM, promotes the believe that the SM is part of a more general model. A candidate mathematical model beyond the SM which provides possible explanations for the above observations is *supersymmetry*.

In the next sections, we briefly describe the major components of the SM, its strengths and limitations and also introduce supersymmetry as a leading candidate for models beyond the SM.

### 2.1.1 Main Components of the SM

Mass, charge, spin and lifetime can be used to identify and categorize fundamental particles of nature. Particles with the same charge, mass and spin but opposite charge are called *Anti-particles* while particles with equal amounts for positive and negative charge are said to be neutral. A interesting classification of particles and anti-particles is using their *spin* ( $s$ ). A particle's spin is an *internal quantum number* expressed as  $n\hbar$ , where  $n$  can be *integer* or *half-integer*. Half-integer spin ( $\frac{1}{2}, \frac{3}{2}, \dots \times \hbar$ ) particles obey a *Fermi-Dirac* distribution or statistics and are called *fermions*. Integer spin particles ( $0, 1, 2, \dots \times \hbar$ ) obey *Bose-Einstein* statistics and are called *Bosons*. No two identical fermions can occupy the same quantum state but any number of bosons can occupy a given quantum state.

Fermions are the fundamental building blocks of matter while bosons mediate interactions between fermions. No particle with spin,  $s = 0\hbar$ , had ever been experimentally observed until the 4th of July 2012 when the *Higgs* boson with spin,  $s = 0\hbar$ , was observed[7]. The Higgs boson is responsible for providing mass to both fermions and bosons. Its discovery completes the SM.

The particle spin set,  $S$ , shown in Equation 2.1.1, shows the spins of particles discovered and yet-to-be-discovered in the universe.

$$S = \left\{ s = \left( \dots 0, \frac{1}{2}, 1, \frac{3}{2}, 2 \dots \right) \cdot \hbar \right\}$$

Looking at the set  $S$ , our present and possibly future understanding of particles in the universe can be summarize as follows:

- $\mathbf{S = \frac{1}{2}\hbar}$  Particles which make up visible matter in the universe.
- $\mathbf{S = 1\hbar}$  Particles mediating gauge interactions.
- $\mathbf{S = 0\hbar}$  Particle responsible for giving mass to other particles.
- $\mathbf{S = 2\hbar}$  Yet-to-be-discovered particle mediating gravitational interactions.
- $\mathbf{S = \frac{3}{2}\hbar}$  Yet-to-be-discovered particle likely to make up **Dark Matter?**

It is interesting to note that the set particles with spins,  $s = \{0, \frac{1}{2}, 1\} \hbar$ , describes precisely only 4.6% of the entire matter in the universe through the SM. The SM is

a *relativistic quantum field theory* in which particles are represented as *quantum fields* and their dynamics and interaction with other particles is expressed using a mathematical functions called *Lagrangian density*,  $\mathcal{L}$ . The Lagrangian density is invariant under certain transformations or symmetries and carries the description of the dynamics of fermions, bosons and their interactions with the Higgs boson. Fermions and bosons obtain their mass by interacting with the Higgs boson through a process crucial to the SM called *Higgs Mechanism*. Our brief description of the SM, will be divided into the following sections:

- **Fermions:** All of visible matter is described using fermion fields.
- **Interactions:** Fermions interact either through electromagnetic, weak and strong interactions with vector bosons mediating the interactions. An interaction is the realization of some generic symmetry and associated with this symmetry is a conserved quantity.
- **Spontaneous Symmetry Breaking or Higgs Mechanism:** Fermions originally have no mass. They get their mass by interacting with the Higgs field through the *Higgs mechanism*. New states of matter or fermions can be formed through mixing with other states of matter or fermions.

## Fermions

The *Dirac* equation given by Equation 2.1 is part of the SM Lagrangian describing

$$\mathcal{L}(\bar{\psi}, \psi, G^\mu) = \bar{\psi} (i\gamma^\mu \mathcal{D}_\mu - m) \psi. \quad (2.1)$$

fermion dynamics with its electromagnetic interaction through the  $\mathcal{D}_\mu$  term. In the full SM Lagrangian, including the description of electromagnetic, weak and strong interactions, fermions participate in these interactions as pairs or *doublets* called a representation. According to the SM, fermions exists as either leptons ( $\ell$ ) or quarks ( $q$ ) and come in 3 *generations*. The SM provides no explanation for the existence of only 3 generations. Leptons can participate in electromagnetic and weak interactions but not in strong interactions while quarks can participate in both interactions and strong interactions. Leptons have integer charge while quarks have fractional charge. The 3

generations of quarks and leptons also known as *flavors* are arranged in a mass hierarchy with the third generation being the heaviest. The second and third generations are meta stable can disintegrate or *decay* into the first generation through weak interactions. A lepton pair consists of a particular lepton flavor and its corresponding neutral neutrino type. There is a corresponding neutrino for each lepton generation. For example, an **electron** ( $e$ ) and its corresponding electron **neutrino** ( $\nu_e$ ) make the first generation pair, ( $e, \nu_e$ ). Other lepton flavors include **muon** ( $\mu$ ) and **muon neutrino** ( $\nu_\mu$ ) pair ( $\mu, \nu_\mu$ ) and **tau** ( $\tau$ ) and **tau neutrino** ( $\nu_\tau$ ) pair ( $\tau, \nu_\tau$ ). In the SM, neutrinos are described as having no mass, however, numerous experiments have confirmed that neutrinos have a very tiny mass (order of electronvolts (eV)) and can oscillate from one generation into another over sufficiently large distances.

For quarks, a first generation pair of quarks consists of an “*up-type*” and a “*down-type*” quark. In addition to the electric charge, quarks also carry a *color* charge and as a result can equally participate in strong interactions. *Up-type* quarks like **up** ( $u$ ), **charm** ( $c$ ), **top** ( $t$ ) have charge of  $+\frac{2}{3}$  and *down-type* quarks such as **down** ( $d$ ), **strange** ( $s$ ), **bottom** ( $b$ ) have a charge of  $-\frac{1}{3}$ . Charges are expressed in units of elementary charge  $e$ . The quark include ( $u, d$ ) is the first generation and ( $c, s$ ) and ( $t, b$ ) are respectively, the second and third generations. Quarks do not exist as free particles in nature but are found bound forming composite particles like *pions* and *protons* collectively called *hadrons*. Hadrons consisting of a quark and antiquark (same mass and spin as a quark but different charge) bound together are called *mesons*, e.g. pions ( $\pi^0, \pi^\pm$ ), while those with at least 3 quarks bound together are called *baryons*, e.g. protons. The distributions of these quarks inside hadrons can be modeled using *parton distribution functions* (PDF) which depends on the fraction of momentum of the given hadron carried by each quark.

One can distinguish between “Left” from the “Right” handed quarks and leptons from the nature of their interaction with electroweak bosons.

Since most particles in the second and third generation are meta-stable, and do decay into the first generation particles, it is possible to describe all visible matter in our universe using only one generation of leptons, **electron** and the **electron neutrino** ( $e, \nu$ ) and one generation of quarks, **up-quark** and **down quark** ( $u, d$ ).

## Interactions

Interaction between fermions is mediated by vector *bosons* with spin,  $s = 1\hbar$ . The SM describes the electromagnetic, weak and strong force and their force mediators. The *electromagnetic force* whose force carrier is a massless vector boson; the *photon* ( $\gamma$ ), is described using the mathematical formulation called *Quantum Electrodynamics* (QED). It is responsible for the interaction of light with matter. The *weak force* has 3 massive vector bosons;  $W^\mp$ ,  $Z^0$ , as its force mediators and it is responsible for the decay of the second and third generation quarks into the first generation. The weak force was independently developed by Sidney Glashow, Abdus Salam and Steven Weinberg [8] in the 1960s unifying it with the electromagnetic force in a mathematical formulation called the *Electro-Weak Field Theory*. The 3 massive vector bosons were predicted in the late 1960s and were eventually discovered at CERN in 1983. Finally, the *strong force* described using the mathematical formulation of *Quantum Chromodynamics* (QCD) has a massless *gluons* (g) as its force mediators. The strong force like the weak force is a nuclear force, however, the same unification of the weak and electromagnetic forces is not observed with the strong force. It remains an open question whether at much higher energies, all 3 forces become unified behaving as a single force.

It is speculated that the gravity interaction not described by the SM, is mediated by a spin-2 particle called the *graviton* which is yet to be discovered.

The formulation of the SM, relies on the concept of *symmetry* and *conserved quantum numbers*. A symmetry is a transformation which leaves invariant the dynamics (Lagrangian density,  $\mathcal{L}$ ) describing a particle interaction. Every particle interaction is associated with a symmetry and a conserved quantity. The conserved quantity is called *conserved quantum number*. Belonging to the SM, are *gauge symmetries*, meaning the SM Lagrangian remains invariant under space-time dependent gauge transformations. The gauge symmetry of the SM is a combination of 3 different gauge symmetries;  $SU(3)_C$ ,  $SU(2)_L$  and  $U(1)_Y$ , each describing a particular particle interaction type. This combination is expressed as given in equation 2.2.

$$SU(3)_C \otimes SU(2)_L \otimes U(1)_Y \quad (2.2)$$

$SU(3)_C$  is the gauge symmetry associated with strong interactions and the conserved quantum number is the *color* ( $C$ ) charge allowing the gluon to interact with itself and with quarks. There are 8 (in the *octet* representation of the  $SU(3)$  gauge symmetry) colorless and massless gluons and three different color type quarks for each quark flavor. Anti-quarks carry anti-color charges. Leptons, like electrons, do not carry the color charge and as a result cannot participate in strong interactions.

$SU(2)_L \otimes U(1)_Y$  is the gauge transformation group with conserved quantum number, *isospin* ( $T_3$ ), necessary for the electroweak interaction. Corresponding to the  $SU(2) \otimes U(1)$  gauge group, there are 4 massless gauge bosons,  $W_\mu^{1,2,3}, B_\mu$ , which combine to form the physical electroweak bosons of charged  $W^\mp$  and neutral  $Z^0$  and  $\gamma$ . The  $W^\mp$  and  $Z^0$ , through the spontaneous breaking of the electro-weak symmetry, obtain their masses. These physical mass states is responsible for quarks to be able to transform from one generation to the other. These bosons couple using the “charge” of the weak interaction called *isospin*,  $T_3$ , and the *hypercharge*,  $Y$ , to matter fields. The  $W^\mp$  only interacts with **left-handed** fermions and **right-handed** anti-fermions. This leads to a phenomenon called *parity* violation. The electromagnetic charge,  $Q$ , is the result of a combination of the third component of the weak isospin,  $T_3$  and the hyper charge,  $Y$ , through the following relation:

$$Q = T_3 + \frac{Y}{2} \quad (2.3)$$

Left handed fermions have  $T_3 = \pm \frac{1}{2}$  and form representations known as isospin *doublets*, while, right-handed fermions have  $T_3 = 0$  and form isospin *singlets* in the SM . The particles in the SM together in their representations given by the gauge symmetry as *multiplets*(*doublets*, *triplets*, etc) and the corresponding conserved quantum numbers is presented in Table 2.1. The  $SU(2)_L \otimes U(1)_Y$  guage group is a combination of two symmetry groups with coupling strengths  $g$  and  $g'$  connected to the electric charge of each fermion as  $e = g \sin \theta_w = g' \cos \theta_w$ .

The angle,  $\theta_w$ , is the *Weinberg angle*,  $\sin^2 \theta_w \approx 0.231$  is not predicted by the SM but measured from experiments. Gauge bosons can rotate from their *weak* eigen states

to physically observed states using this angle.

$$W^\mp_\mu = \frac{W_\mu^1 \mp i W_\mu^2}{\sqrt{2}}, \quad \begin{pmatrix} A_\mu \\ Z_\mu \end{pmatrix} = \begin{pmatrix} \cos \theta_w & \sin \theta_w \\ -\sin \theta_w & \cos \theta_w \end{pmatrix} \begin{pmatrix} B_\mu \\ W_\mu^3 \end{pmatrix} \quad (2.4)$$

This angle,  $\theta_w$ , also allows for the transformation of a quark from one flavor into another through the  $W^\mp$  bosons. In the lepton sector, according to formulation of the SM, such flavor transformation could in principle be possible but does not lead to any possible observable effects as neutrinos are considered to be massless in the SM. On the other hand, recent neutrino experiments have proven otherwise, as mixing between different neutrino types have been observed, indicating that neutrinos are not massless as thought but rather do have mass. The transformation of quarks into different flavors is a typical interaction happening inside the core of our sun in the decay of neutrons to protons and similarly in a nuclear reactor. The complete transformation of all quark flavors is described by the *Cabibbo-Kobayashi-Maskawa* (CKM) 3 by 3 matrix whose elements are parameters only measured from experiments and not predicted by the SM.

Particle and Their Gauge Symmetry Representation

Particle Name(Symbol)	Spin	Multiplet	$SU(3)_C \otimes SU(2)_L \otimes U(1)_Y$
Quarks ( $Q$ )	$1/2$	$(\mathbf{u}_L, \mathbf{d}_L)$	$(\mathbf{3}, \mathbf{2}, \frac{1}{6})$
$\bar{\mathbf{u}}$	$1/2$	$\mathbf{u}_R^\dagger$	$(\bar{\mathbf{3}}, \mathbf{1}, -\frac{2}{3})$
$\bar{\mathbf{d}}$	$1/2$	$\mathbf{d}_R^\dagger$	$(\bar{\mathbf{3}}, \mathbf{1}, \frac{1}{3})$
( $\times 3$ families)			
Leptons( $L$ )	$1/2$	$(\nu, \mathbf{e}_L)$	$(\mathbf{1}, \mathbf{2}, -\frac{1}{2})$
$\bar{\mathbf{e}}$	$1/2$	$\mathbf{e}_R^\dagger$	$(\bar{\mathbf{1}}, \mathbf{1}, 1)$
( $\times 3$ families)		$\nu_R^\dagger$	$(\bar{\mathbf{1}}, \mathbf{1}, 1)$
Higgs ( $\mathbf{H}_u$ )	$0$	$(\tilde{\mathbf{H}}_u^+, \tilde{\mathbf{H}}_u^0)$	$(\mathbf{1}, \mathbf{2}, +\frac{1}{2})$
Higgs( $\mathbf{H}_d$ )	$0$	$(\tilde{\mathbf{H}}_d^+, \tilde{\mathbf{H}}_d^-)$	$(\mathbf{1}, \mathbf{2}, -\frac{1}{2})$
<b>Force Carriers</b>			
Gluons	$1$	$\mathbf{g}$	$(\mathbf{8}, \mathbf{1}, 0)$
<b>(Strong Force)</b>			
W bosons	$1$	$\mathbf{W}$	$(\mathbf{1}, \mathbf{3}, 0)$
B boson	$1$	$\mathbf{B}^0$	$(\mathbf{1}, \mathbf{1}, 0)$
<b>(Electro-Weak Force)</b>			

Table 2.1: SM particles and their gauge multiplets(representation) with quantum numbers. the numbers for example  $(\mathbf{3}, \mathbf{2}, \frac{1}{6})$  means (*triplet, doublet,  $Y = 1/6$* ) representations.

### 2.1.2 Spontaneous Symmetry Breaking

*Spontaneous symmetry breaking* is the spontaneous breaking of the gauge symmetry from a parent symmetry into an entirely, new sub-symmetry. In the SM, spontaneous symmetry is realized as represented by the expression in equation 2.5.

$$SU(3)_C \otimes SU(2)_L \otimes U(1)_Y \xrightarrow{SSB \text{ into}} SU(3)_C \otimes U(1)_{QED} \quad (2.5)$$

Early attempts prior to the 1960s to construct a gauge theory of weak interactions failed because the gauge bosons were massless while experimental evidence proved otherwise.

The Higgs (or Higgs-Brout-Englert) mechanism [10], is achieved by introducing a complex weak isospin *scalar doublet*,  $\phi$ , i.e spin  $s = 0\hbar$ . During this process, the  $SU(2)_L \otimes U(1)_Y$  symmetry is spontaneously broken into a  $U(1)$  symmetry which describes electromagnetic interaction. Figure 2.1 shows a picture of the potential of the spin-0 complex Higgs field. The minimum value of the potential,  $|\phi_0| = \sqrt{\frac{-\mu^2}{\lambda}} = \nu$ , based on the choice of the parameters  $\mu^2 < 0$  and  $\lambda > 0$ , is to spontaneously break the  $SU(2)_L \otimes U(1)_Y$  symmetry into  $U(1)$  symmetry. During spontaneous symmetry breaking, both matter and gauge bosons, except the photon  $\gamma$ ), obtain masses. The process is referred to as *Higgs-Brout-Englert mechanism* or *Higgs mechanism*.

Quarks and leptons obtain their masses through their interaction with the Higgs field. A fermion's mass,  $m_f$ , is proportional to the strength of its interaction (Yukawa coupling  $\lambda_f$ ) with the Higgs field. Electro-weak interaction mediating gauge bosons,  $Z^0$  and  $W^\pm$  obtain their mass  $m_Z$  and  $m_{W^\pm}$ , respectively, by engulfing or “*eating*” the available massless components (*Nambu-Goldstone bosons*) of the complex Higgs doublet. From the four scalar fields(complex Higgs doublet), only a physically massive *Higgs boson* remains.

$$m_f = \lambda_f \frac{\nu}{\sqrt{2}}, \quad \frac{m_{W^\pm}}{m_Z} = \frac{\frac{1}{2}\nu g}{\frac{1}{2}\nu \sqrt{g^2 + g'^2}} = \cos \theta_w \quad (2.6)$$

The search for the Higgs boson was one of the purpose for building the large hadron collider at CERN. The discovery of the Higgs candidate scalar boson through its decay into two photons,  $H \rightarrow \gamma\gamma$ , and a pair of Z bosons,  $H \rightarrow ZZ$ , was presented to the public on July 04, 2012. Its measured mass was  $m_H = 125 \pm 0.21 \text{ GeV}/c^2$ .

It is important to note that there is no fundamental reason given by the SM why there should be only one type of the Higgs field to which all fermions couple to obtain their masses nor any prediction from the SM for the choice of parameters. There are other models such as supersymmetry, which allows for the possibility of more than one Higgs field. In Figure 2.2, we show a complete summary of particles and their interactions as described by the SM.

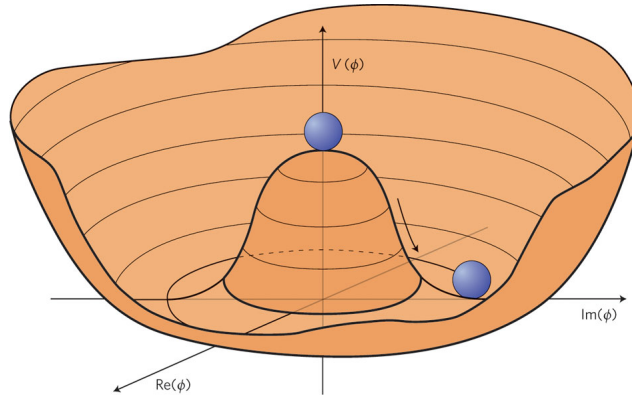


Figure 2.1: Higgs boson “Mexican hat” potential,  $V(\phi^*\phi) = \mu^2(\phi^*\phi) + \lambda(\phi^*\phi)^2$ , which leads to spontaneous symmetry breaking with choice of parameters  $\mu^2 < 0$ ,  $\lambda > 0$ .

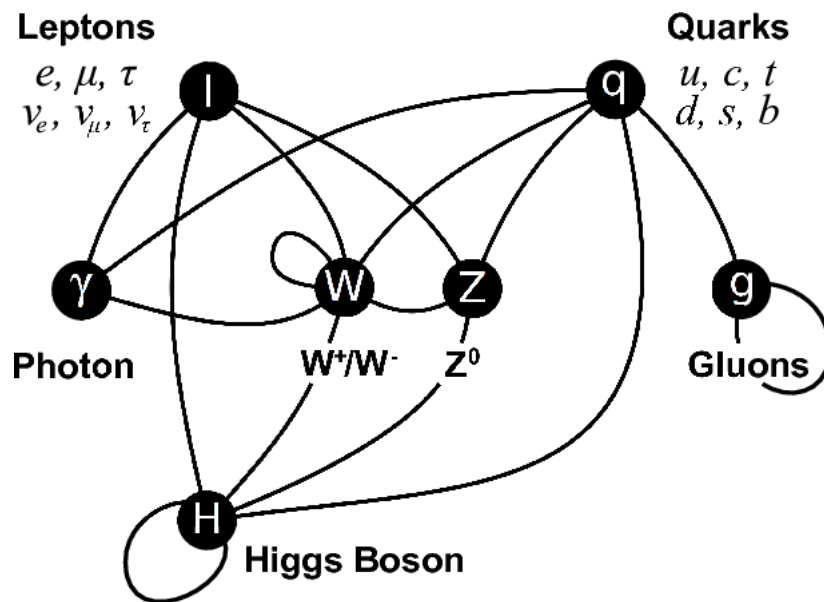


Figure 2.2: SM particles and their interactions with vector bosons as mediators.

### 2.1.3 Limitations of the Standard Model

Although numerous experiments support the SM in its description of particle properties with unmatched precision, there are many unanswered questions by the SM. We provide a summary below of those of our interest.

- **General Formalism**

Many important parameters like particle masses, Weinberg angle, the CKM matrix elements, for example, cannot not be derived from the SM. These are measured from experiments. Why only 3 generations of particles? Why the specific doublet representation of fields in the SM? These are questions to which the SM provides no answer.

- **Cosmological**

Why is there so much matter than anti-matter in the universe? *Cosmic Microwave Background* (CMB) and the *Wilkinson Microwave Anisotropy Probe* (WMAP) experimental results indicate the presence of excess matter which does not interact with light called *Dark Matter* (DM) and *Dark Energy* (DE). DE is responsible for the increase energy density causing rapid accelerating expansion of the universe. The nature of DM and DE and such observations cannot be explained using the current SM.

- **Theory**

SM description of nature does not include gravitational interactions. Observation of SM coupling constants varying with energy begs the question of whether at some higher energy scale, all the weak, strong and electromagnetic coupling constants behave as one i.e unified as a single coupling constant. If possible, at what energy scale does this force unification occur?

- **Mass Hierarchy or Naturalness**

Particle masses ranges from neutrino masses, a few eV to the top particle's mass of  $173 \text{ GeV}/c^2$ . The SM does not explain this mass hierarchy. To some physicist, the energy gap between the electro-weak symmetry breaking energy scale ( $\approx 246 \text{ GeV}$ ) and the Planck energy scale (reduced Planck mass,  $M_p = 10^{18} \text{ GeV}$ ) seems unnatural.

## 2.2 Beyond Standard Model Physics

The Higgs boson mass from SM predictions include additional corrections,  $\delta m^2$ , to the higgs mass through its couplings with fermions such as the diagram shown in Figure 2.3(a). These additional corrections are given as shown in equation 2.7.

$$\delta m_f^2 = \frac{1}{16\pi^2} |\lambda_f|^2 \left( -2\Lambda^2 + 6m_f^2 \ln \left( \frac{\Lambda}{m_f} \right) + \dots \right) \quad (2.7)$$

Where  $\lambda_f$  is the Higgs to fermion coupling,  $\lambda_f H f \bar{f}$  and  $\Lambda$  is an arbitrarily large energy scale (can be of order  $10^{18}$  GeV) called the *cut-off* energy scale. As a result of this cut-off scale being very large, these corrections can also be very large. However, large corrections to the Higgs boson's mass are not observed in experimental measurements of the Higgs boson's mass which is  $125$  GeV/ $c^2$ . The SM provides no explanation for why these corrections are not observed.

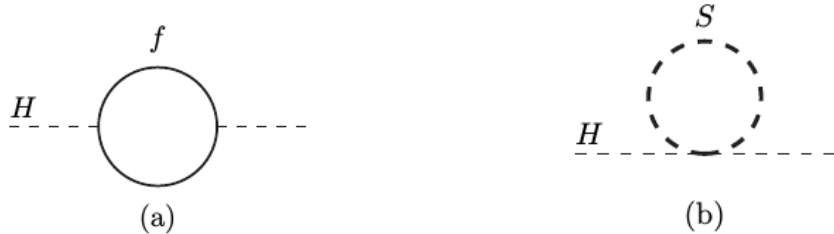


Figure 2.3: Higgs mass contributions from its coupling to fermions (a) and scalar (b) fields.

Models beyond the SM like *supersymmetry*, provide a plausible explanation as to why these corrections are not observed in experiments. The explanations is that, there are in addition to the higgs boson being the only scalar particle in the SM, new scalar particles, yet to be observed, which can also couple to the higgs field as shown in the diagram in figure 2.3(b). These scalar coupling contribution, given in equation 2.8 is of the opposite sign and as a result cancel the fermion contributions to the Higgs boson's mass. This is the explanation why the corrections to the Higg Boson's mass cannot be observed experimentally.

$$\delta m_S^2 = \frac{1}{16\pi^2} |\lambda_S|^2 \left( \Lambda^2 - 2m_S^2 \ln \left( \frac{\Lambda}{m_S} \right) + \dots \right) \quad (2.8)$$

This problem is known as the *Hierarchy problem* and is explained using supersymmetry. This cancellation is provided at all levels of the Higgs boson interaction and for whatever energy scale the cut-off value may be. Supersymmetry does not only provide an explanation to the Hierarchy problem, but also provide a good framework for the unification of fundamental forces. In addition, supersymmetry also predicts the existence of additional particles to the SM which are non interacting with ordinary matter and having very long lifetime making these particles exceptional candidates as dark matter particles. These properties motivates the study of supersymmetry as an interesting extension of the SM for understanding physics beyond the SM (BSM).

### 2.2.1 Supersymmetry

Supersymmetry is a relativistic Quantum Field Theory (QFT), relating space-time symmetries (rotation and translation) and gauge symmetries ( $SU(3)_C \otimes SU(2)_L \otimes U(1)_Y$ ). During the early period, very little was understood about supersymmetry. Progress in understanding began with the *Haag-Lopuszanski-Sohnius* theorem [11] in 1975. This led to the introduction of supersymmetry generators called *Lie-superalgebra* generators,  $Q_i$ ,  $i = 1, \dots, N$ , where  $N$  is the number of supersymmetry generators, which anti-commute with the group and space-time generators. The consequence is that fermions can be transformed into bosons and vice-versa. This boson-to-fermion and fermion-to-boson transformation is expressing using Equations 2.9.

$$Q|\text{Fermion}\rangle = |\text{Boson}\rangle, \quad Q|\text{Boson}\rangle = |\text{Fermion}\rangle \quad (2.9)$$

Thus, in supersymmetry, particles in a given state have the *same* mass but differ in their spin by half  $\hbar$  and in every irreducible representation of supersymmetry, like the chiral representation, there is an equal number of fermionic and bosonic degrees of freedom. Every particle has a supersymmetric partner with the same mass belonging to the same state representation or *supermultiplet*.

These supermultiplets are either *Chiral*, *Vector* or *Gravity* multiplets. The minimal supersymmetric extension of SM uses Chiral and Vector supermultiplets shown in Table 2.2.

<b>Supermultiplets</b>	<b>Spin in SM,</b>	<b>Spin in Supersymmetry</b>
<i>Chiral</i>	0	$\frac{1}{2}$
<i>Chiral</i>	$\frac{1}{2}$	0
<i>Vector</i>	1	$\frac{1}{2}$
<i>Gravity</i>	2	$\frac{3}{2}$

Table 2.2: Supermultiplets and particle spin in SM and Supersymmetry.

Models in supersymmetry are developed using *superfields*,  $\Phi$ . A given superfield consists of ordinary scalar real or complex fields ( $\phi$ ), a Lorentz vector field ( $A_\mu$ ) and Left-handed or Right-Handed Weyl(2 degrees of freedom) spinor fields ( $\psi$ ). *Chiral* and *Vector* superfields are used in constructing the minimal supersymmetric standard model. The simplest supersymmetric model is an extension of the SM to include supersymmetric particles with the same mass as their standard model partners. It is called the *Minimal Supersymmetric Standard Model* because it only involves the use of a single supersymmetry generator.

### 2.2.2 Minimal Supersymmetric Standard Model

In the Minimal Supersymmetric Standard Model (MSSM), the number of fundamental particles is increased. The full particle content in MSSM with this extension from SM is shown in Table 2.3 and 2.4.

The nomenclature of supersymmetric particles is derived from their SM counterparts by adding an “*s*” in front of the SM particles names. For example, a *selectron* is the supersymmetric partner of the electron, *squarks* are the supersymmetric partners of SM quarks. There are exceptions to this nomenclature which we will mentioned later. Both supersymmetry particles and their SM partners should have the equal masses, however, there have been no experimental evidence for such supersymmetric particles having the same mass as SM particles. Therefore, Supersymmetry is definitely not an exact symmetry in nature and must be spontaneously broken.

Particle Names	Symbol	spin 0	spin 1/2	$SU(3)_C \otimes SU(2)_L \otimes U(1)_Y$
squarks, quarks ( $\times 3$ families)	$Q$	$(\tilde{u}_L, \tilde{d}_L)$	$(u_L, d_L)$	$(\mathbf{3}, \mathbf{2}, \frac{1}{6})$
	$\bar{u}$	$\tilde{u}_R^*$	$u_R^\dagger$	$(\bar{\mathbf{3}}, \mathbf{1}, -\frac{2}{3})$
	$\bar{d}$	$\tilde{d}_R^*$	$d_R^\dagger$	$(\bar{\mathbf{3}}, \mathbf{1}, \frac{1}{3})$
sleptons, leptons ( $\times 3$ families)	$L$	$(\tilde{\nu}, \tilde{e}_L)$	$(\nu, e_L)$	$(\mathbf{1}, \mathbf{2}, -\frac{1}{2})$
	$\bar{e}$	$\tilde{e}_R^*$	$e_R^\dagger$	$(\bar{\mathbf{1}}, \mathbf{1}, 1)$
higgsinos, Higgs	$H_u$	$(H_u^+, H_u^\circ)$	$(\tilde{H}_u^+, \tilde{H}_u^\circ)$	$(\mathbf{1}, \mathbf{2}, +\frac{1}{2})$
	$H_d$	$(H_d^\circ, H_d^-)$	$(\tilde{H}_d^\circ, \tilde{H}_d^-)$	$(\mathbf{1}, \mathbf{2}, -\frac{1}{2})$

Table 2.3: Chiral supermultiplets and representation in Minimal Supersymmetric SM (MSSM). Super symmetric particles (sparticles) have a  $\sim$  on them. Spin -0 fields are complex scalars while spin-1/2 fields are left-handed two component Weyl fermions.

Particle Names	spin 1/2	spin 1	$SU(3)_C \otimes SU(2)_L \otimes U(1)_Y$
gluino, gluon	$\tilde{g}$	$g$	$(\mathbf{8}, \mathbf{1}, 0)$
winos, $W$ bosons	$\tilde{W}^\pm, \tilde{W}^\circ$	$W^\pm, W^\circ$	$(\mathbf{1}, \mathbf{3}, 0)$
bino, $B$ boson	$\tilde{B}^\circ$	$B^\circ$	$(\mathbf{1}, \mathbf{1}, 0)$

Table 2.4: Gauge supermultiplets and representations in Minimal Supersymmetric SM (MSSM). Super symmetric particles (sparticles) have a  $\sim$  on them.

Similar to the Higgs mechanism, supersymmetry breaking is also spontaneous and breaking supersymmetry can happen in many different ways. One of the ways in which supersymmetry is spontaneously broken is by gauge interactions. Supersymmetric models formulated using gauge interactions as the way to spontaneously break supersymmetry is called *Gauge Mediated Supersymmetry Breaking* (GMSB) models. GMSB models are interesting because they allow for only 5 fundamental parameters and still provide candidate dark matter particles. Supersymmetry breaking is realized in each model through a *superpotential* and the breaking defines the phenomenology and particle mass spectrum. In MSSM, particles interact with the Higgs bosons through a superpotential to

obtain their masses . This superpotential can be expressed as given in Equation 2.10.

$$W_{\text{mssm}} = \bar{u} \mathbf{y_u} Q H_u - \bar{d} \mathbf{y_d} Q H_d - \bar{e} \mathbf{y_e} L H_d - \mu H_d H_u \quad (2.10)$$

The objects  $H_u$ ,  $H_d$ ,  $Q$ ,  $L$ ,  $\bar{u}$ ,  $\bar{d}$ ,  $\bar{e}$  are chiral superfields of the chiral supermultiplets given in Table 2.3 above. The dimensionless couplings  $\mathbf{y_u}, \mathbf{y_d}$ , and  $\mathbf{y_e}$  are  $3 \times 3$  matrices of the Yukawa couplings. Rather than a single Higgs *doublet* which is assumed in the SM, supersymmetry breaking requires two Higgs doublets:  $H_u$  and  $H_d$ . The two Higgs give mass to **up-type** and **down-type** quarks, respectively, and to leptons, The superpartners of these Higgses are fermions and those of the gauge bosons called *gauginos* mix to produce new neutral and charged fermions called *Neutralinos* and *Charginos*, respectively. In order for GMSB models predictions of the proton lifetime to agree with experimental measurements of the proton lifetime being  $> 10^{32}$  years, a matter symmetry relating the quarks to leptons through the *baryon* ( $B$ ) and *lepton* numbers ( $L$ ), a symmetry called *R-Parity* is introduced. R-parity is defined as,  $R_P = (-1)^{3(B-L)+2S}$ , where  $S$  is the particle's spin. SM particles like quarks have an *even* R-parity,  $R_P = 1$ , while supersymmetric particles like squarks have odd parity  $R_P = -1$ . The phenomenological consequence of R-parity is that, first, in the decay of supersymmetric particles, the lightest SUSY particle (LSP) have odd parity  $R_P = -1$  and is considered to be absolutely stable. Second, every supersymmetric particle produced and is not the LSP, will eventually decay into the LSP or an odd number of LSPs. Third, supersymmetric particles can only be produced in pairs in a collider experiment. If, in addition to being stable, the LSP is neutral and interacts only very weakly with ordinary matter, then this makes it a good candidate for non-baryonic dark matter as required by cosmology, [3]-[5].

*R-parity Conserving* (RPC) models with the LSP stable are different from models without the conservation of R-parity. These R-parity non-conserving models are called *R-parity Violating* (RPV) models. In RPV models the LSP is unstable and decays to SM particles. A simplified version of GMSB models studied in this thesis is the *Snowmass Point and Slopes* (SPS8),[6], models whose phenomenological predictions are within the reach of the large hadron collider. It is possible to produce supersymmetric particles with mass of about a few TeV at the large hadron collider (LHC).

Figure 2.4 presents the mass spectrum for supersymmetric particle as predicted by the SPS8 model. The mass difference is determine by the supersymmetry breaking energy scale represented by  $\Lambda$ .

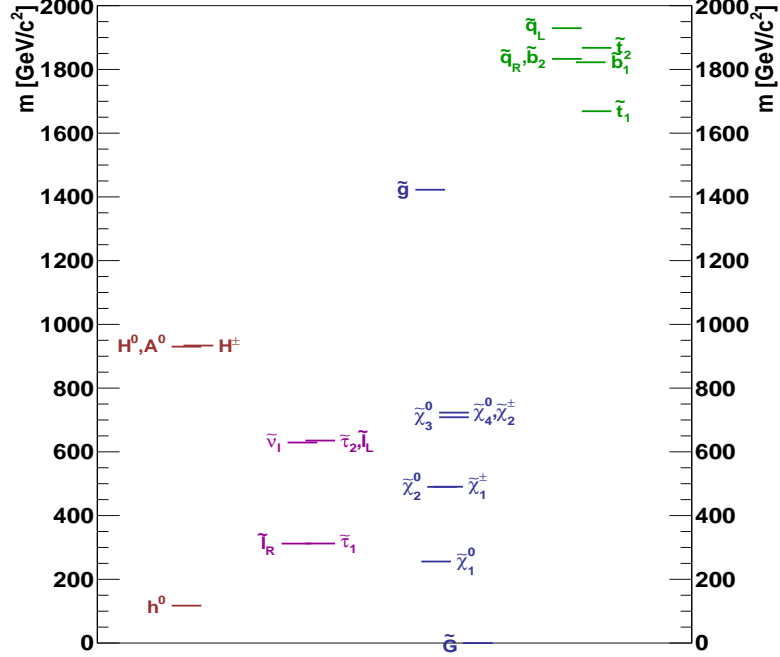


Figure 2.4: Supersymmetry particle mass spectra in the SPS8 or minimal GMSB (mGMSB) model.

In summary, MSSM predicts the existence of new particles whose spin ( $S$ ) differ from their SM counterparts by half-integer. Bosons (fermions) in the SM have superpartners which are fermions (bosons). The superpartners of SM fermions are scalars called *sfermions* ( $\tilde{l}$ ), sneutrinos ( $\tilde{\nu}$ ) and squarks ( $\tilde{q}$ ) while *gluinos* ( $\tilde{g}$ ) are the superpartners of the massless gauge bosons of strong interaction, gluons. The scalar Higgs (2 needed) bosons and the vector gauge bosons of Electro-Weak interaction have fermionic superpartners called *higgsinos*, *Winos* and *Binos*. These can mix to form a pair of mass eigenstates called *charginos* ( $\tilde{\chi}_j^\pm, j = 1, 2$ ), i.e.,  $\tilde{\chi}_{1,2}^\pm$  are mixtures of  $\tilde{W}^+, \tilde{W}^-, \tilde{H}^+, \tilde{H}^-$  and a quartet of mass eigenstates called *neutralinos* ( $\tilde{\chi}_i^0, i = 1, \dots, 4$ ), i.e.,  $\tilde{\chi}_{1-4}^0$  are mixtures of  $\tilde{B}^\circ, \tilde{W}^\circ, \tilde{h}^\circ, \tilde{H}^\circ$ .

## 2.3 Gauge Mediated Supersymmetry Breaking Models

GMSB models have 5 main parameters:

$$\{\Lambda, M_{\text{mess}}, N_5, \tan(\beta), sgn(\mu), C_{\text{grav}}\} \quad (2.11)$$

where  $\Lambda$  is the effective supersymmetry breaking scale,  $M_{\text{mess}}$  is the mass of the messenger particle involved in mediating supersymmetry breaking to the MSSM energy scale,  $N_5$  is the number of messenger particles. The other parameters,  $\tan \beta$  and  $sgn(\mu)$  are related to the two Higgs bosons necessary for supersymmetry breaking with  $\tan \beta$  being the ratio of the vacuum expectations values for both Higgs bosons. The sign of the Higgs potential is defined by  $sgn(\mu)$ . In these models, the gravitino can become very light with its mass bounded only by cosmological observations and as such is identified as the Least Stable supersymmetric particle (LSP). The mass of the gravitino is expressed in terms of the parameter  $C_{\text{grav}}$  according to equation 2.12.

$$m_{\tilde{G}} = C_{\text{grav}} \cdot \frac{\Lambda M_{\text{mess}}}{\sqrt{3} M_{pl}} \quad (2.12)$$

where  $M_{Pl} = 1.3 \times 10^{19}$  GeV/c<sup>2</sup>.  $C_{\text{grav}}$  is a scaling parameter, which determines the lifetime of the Next-to-Lightest-Supersymmetric Particle (NLSP) since the neutralino decay rate to the gravitino will depend on the mass difference between the neutralino and gravitino.

### 2.3.1 Phenomenology

Light gravitinos with unique gravitino-scalar-chiral fermion and gravitino-gaugino-gauge boson interactions shown in Figure 2.5 in GMSB models allow for the gravitino mass to be as low as a few eV and up to an upper bounded for them to provide the right amount of dark matter observed in the early universe. In addition to this, being neutral and stable makes them an excellent candidate particle for dark matter.

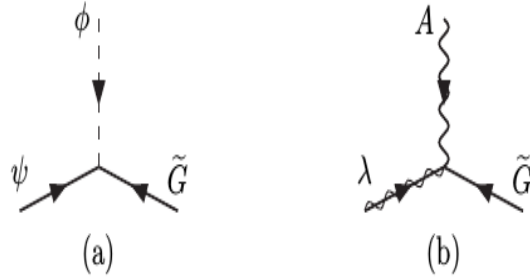


Figure 2.5: Feynman diagrams of gravitino/golstino,  $\tilde{G}$ , gaugino and scalar interactions with superpartner pairs  $(\psi, \phi)$  scalar (a) and  $(\lambda, A)$  gaugino (b) decay to gravitino.

The decay of the NLSP to the gravitino is always accompanied by the SM partner of the NLSP, in order to conserve R-parity. If the particle,  $\tilde{p}$ , is the NLSP, its decay to gravitino and its SM particle,  $p$ , is given as  $\tilde{p} \rightarrow p + \tilde{G}$ . In the SPS8 benchmark model, the choice of parameters is as follows:  $\mathbf{M}_{mess} = 2\Lambda$ ,  $\tan(\beta) = 15$ ,  $\mathbf{N}_5 = 1$ . Only  $\Lambda$  and  $C_{grav}$  are allowed to vary, [6]. The gravitino ( $\tilde{G}$ ), is the LSP. The NLSP,  $\tilde{p}$ , is the lightest neutralino ( $\tilde{\chi}_1^0$ ). There are four types of neutralinos which are a mixture of the supersymmetric particles Bino ( $\tilde{B}^\circ$ ), Wino ( $\tilde{W}^\circ$ ), higgsino ( $\tilde{H}_u^\circ, \tilde{H}_d^\circ$ ), depending on the choice of parameters  $\Lambda$ ,  $\tan \beta$ , and  $sgn(\mu)$ . The particle  $p$  could be a photon ( $\gamma$ ), Z boson ( $Z$ ) (or  $Z'$ ) and a higgs boson ( $h$ ). This thesis, for experimental convenience, will focus on the parameter space for which the particle  $p$  is a photon ( $\gamma$ ) and  $C_{grav} > 1$ . This ensures that the lifetime of the NLSP is long enough but still its decay happens within the detector volume and the resulting photon is delayed or non-prompt on length scales of size of the detector. The decay rate for a NLSP to its SM partner and a gravitino can be approximated using only the mass of the NLSP and the effective supersymmetry breaking scale,  $\mathbf{F} = C_{grav} \cdot \Lambda \cdot \mathbf{M}_{mess}$  giving in equation 2.13.

$$\Gamma(NLSP \rightarrow \gamma \tilde{G}) \approx \frac{m_{NLSP}^5}{\mathbf{F}^4} \quad (2.13)$$

This approximation is almost the same for the non-minimal GMSB models except that additional parameters are present showing explicit dependence of the neutralino life time on its states as a mixture of other supersymmetric particles.

### 2.3.2 Long-Lived Particles in GMSB Models

Measuring a particle's life time or distance travelled before it decays can be a useful method to uncover new fundamental interactions. As the lifetime is related to the decay rate which is determined by the particles interactions and available energy space.

#### Production of supersymmetric particles at Hadron Colliders

The production of a particle in a particle collider is a probabilistic process. This probability is expressed as a measurable quantity called *cross section*. For example, the cross section of producing a particle in proton-proton collider such as the LHC, is the probability that the proton beams will collide and interact in a certain way to produce that particle. Although this cross section ( $\sigma$ ) is measured in units of area as *barns* ( $1b = 10^{-24} \text{ cm}^2$ ), usually it has very little relation to the physical interpretation of area as used in everyday life. It is rather a technical term for counting the number of the particle produced when these proton beams collide. The cross section of producing the particle depends on the available energy of the proton beams compared to the mass of the particle, the type of interaction during collision which in turn depends on the coupling constants, and the flux of the proton beams. The rate or number per unit time of the particle produced at a specific particle collider is given as a product of its cross section times the instantaneous luminosity ( $\mathcal{L}$ ). The instantaneous luminosity is the number of incident particles per unit area per unit time. The typical cross section of producing a supersymmetry particle at the LHC is of the order of  $1 \text{ pb} = 10^{-12} \times 10^{-24} \text{ cm}^2$  or at times  $1 \text{ fb} = 10^{-15} \times 10^{-24} \text{ cm}^2$  for extremely rare SUSY processes. While that for a standard model process like the production of the Z or  $W^\pm$  bosons is of the order of a few  $nb = 10^{-9} \times 10^{-24} \text{ cm}^2$ . This means there are more SM processes than supersymmetry process and so the search for supersymmetric particles in the LHC is very challenging.

The rate of production of a supersymmetric particle at the LHC depends on the mass of supersymmetric particle. The masses of supersymmetric particles are much higher than those of SM particles and as a result, the cross section for producing supersymmetry particles at a hadron collider is much smaller compared to that for SM particles. The cross section of a given supersymmetric process happening at the particle collider

can be computed and compared with experimental measurements. Using diagrammatic representations called *Feynmann* diagrams of the process happening, the cross section is derived from the Feynmann diagrams as the computed probability of the process. Supersymmetry processes which leads to the production and decay of neutralino ( $\tilde{\chi}_1^0$ ) at the LHC can involve electro-weak and strong interactions. The production of supersymmetry particles in strong interactions have larger cross sections compared to electro-weak processes because of the strong coupling in strong interaction processes. Many interaction processes in the LHC are strong interactions as the LHC is a proton-proton collider. We show in Figure 2.6 a diagram showing the variation of the supersymmetry production cross section against the mass of the supersymmetric particle. From this figure, it is clear that the production of supersymmetric particle at the LHC through strong interactions like  $pp \rightarrow \tilde{g}\tilde{g}$ ,  $\tilde{q}\tilde{q}$  is higher than through electro-weak interactions like  $pp \rightarrow \tilde{\chi}^\pm\tilde{\chi}^\mp$ ,  $\tilde{\chi}^0\tilde{\chi}^\pm$ .

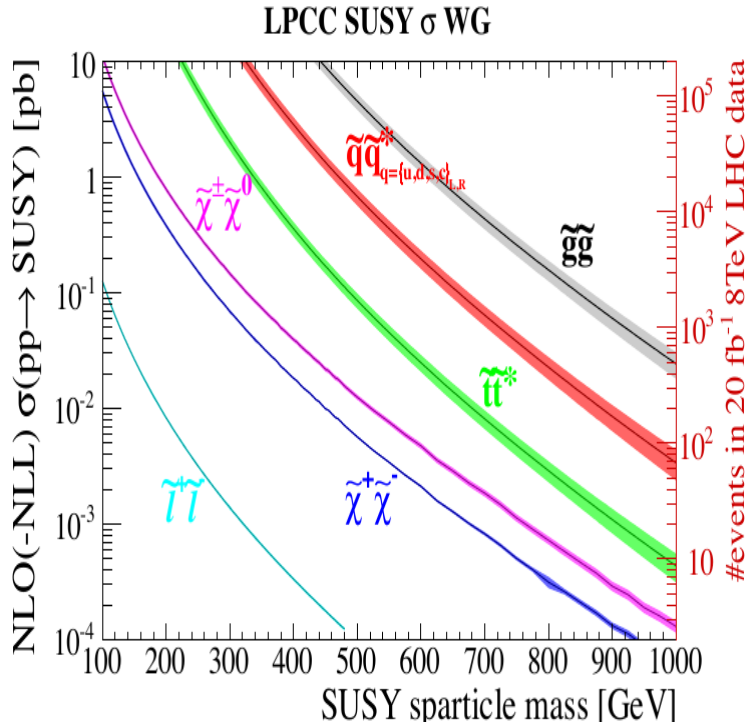


Figure 2.6: Supersymmetry production cross-section against sparticle mass for different modes of supersymmetry production at a proton-proton collider.  $pp \rightarrow \widetilde{g}\widetilde{g}$ ,  $\widetilde{q}\widetilde{q}$  processes have the dominant production cross section.

We will concentrate on the production of neutralinos from processes like  $pp \rightarrow \widetilde{g}\widetilde{g}$ ,  $\widetilde{q}\widetilde{q}$ , as these processes have a higher production cross section at the LHC. We mentioned earlier that a probable manner in which neutralinos can be produced is from the production and subsequent decay of higher massive supersymmetric particles. Some of these higher massive supersymmetric particles include squarks ( $\widetilde{q}$ ), excited squarks ( $\widetilde{q}^*$ ) and gluinos ( $\widetilde{g}$ ). In this scenario, the neutralino is produced *indirectly* or as we say from the *cascade decay* of higher massive supersymmetric particles. The Feynmann diagram for these production processes,  $pp \rightarrow \widetilde{g}\widetilde{g}$ ,  $\widetilde{q}\widetilde{q}^*$ , are given in figure 2.7. Squarks and gluinos do not directly decay into gravitinos but through neutralinos and eventually to gravitinos because their coupling to the gravitinos is not possible. The reason for this is that, in GMSB models, there are no gravitino-gluino-gauge boson or gravitino-squark-gauge boson couplings but rather gravitino-gaugino-gauge boson or gravitino-scalar-chiral fermion couplings.

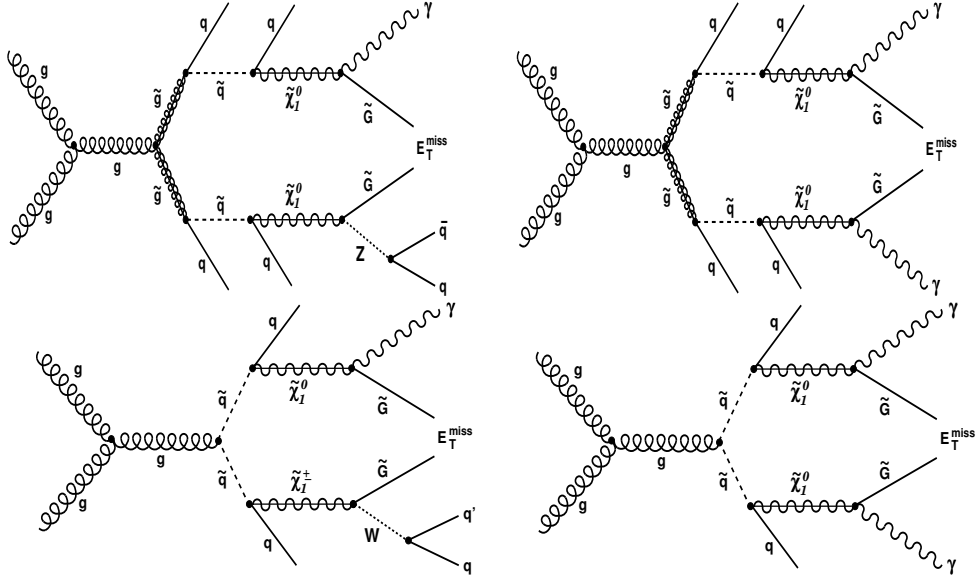


Figure 2.7: Feynmann diagrams for neutralino production from the cascade decay of a produced gluino (*top*) and squark (*bottom*). The final event has a single (*left diagrams*) or double photons (*right diagrams*) neutralino decay at LHC.

### Particle Decay Rate

When a particle is produced, say particle **A**, its coupling to other particles, say particles **B<sub>1</sub>** … **B<sub>n</sub>**, where  $n$  is total number of particles particle, allows for it to decay into these other particles. In addition to the coupling, if the mass of particle **A** is greater than the total sum of mass of particles **B<sub>1</sub>** … **B<sub>n</sub>**, i.e  $m_{\mathbf{A}} > m_{\mathbf{B}_1} + \dots + m_{\mathbf{B}_n}$ , then we say, particle **A** *decays* to particles **B<sub>1</sub>** … **B<sub>n</sub>**. Particle for which no such channel for decay is possible are termed *stable*. Our current understanding is that only the electron (e) and the proton (p) are stable( although there are theories which predict the proton to decay after  $10^{34}$  years and also theories where stable heavy or light particles will explain the nature of Dark Matter. This time through which a particle lived before it decays is called its *lifetime*. Particle decays in which the particle decays instantly as soon as they are produced are called *prompt* decays while particle decays with observable lifetime are *non-prompt* decays. Non-prompt decays might range from factors of a seconds i.e. *nanoseconds* ( $1 \text{ ns} = 10^{-9} \text{ s}$ ) to minutes. In particle decay, strong *couplings* and large *mass difference* between the parent and the daughter particle(s) leads to faster

the decay. The process of obtaining the decay rate during experiments is expressed mathematically as;  $N(t) = N(0)e^{-t/\tau}$ , where both  $N(t)$  and  $N(0)$  are the number of the particles present at time  $t$  and at the beginning,  $t = 0$ .  $\tau$  is the particle's *lifetime*. The rate at which a particle decays is its *decay width* ( $\Gamma$ ). The decay width relies on the availability of daughter particle(s) the parent particle can couple to and the mass(es) of the daughter particle(s) must be less than the mass of the parent particle. Thus, a given particle, **A** will preferentially decay to particles **C<sub>1</sub>** … **C<sub>n</sub>** with which it has stronger couplings and its mass is much larger than their masses. This preferential decay into a specific set of particles or channel brings about terms like *Branching Ratio* (BR). The BR is related to the total decay width through  $BR = \Gamma/\Gamma_{\text{Total}}$ , where,  $\Gamma_{\text{Total}}$  is the particle's total decay width and  $\Gamma$  is its decay width to a preferential channel. The decay width is related to lifetime,  $\tau$ , as the inverse of the lifetime. This relationship is expressed as given in Equation 2.14.

$$\tau = \frac{\hbar}{\Gamma} \quad (2.14)$$

$\tau$  is the particle's lifetime in a frame where the particle is not moving. It is convenient to express lifetime in units of lengths rather than time. The lifetime in units of lengths e.g. meters (m), is  $c\tau$ , where  $c$  is the speed of light in vacuum.  $c\tau$  is also called the *proper decay length* just as the lifetime,  $\tau$ , is also called the *proper lifetime*. Since most particles have mass and travel with velocity  $\vec{v}$  not equal to  $c$ , this distance travel considering  $|\vec{v}| \neq c$  is fully expressed using equation 2.15.

$$\vec{L} = \vec{\beta}\gamma c\tau \quad (2.15)$$

where  $\vec{\beta} = \frac{\vec{v}}{c}$ ,  $\vec{v}$  is the particle's traveling velocity and  $\gamma = \frac{1}{\sqrt{1-\frac{v^2}{c^2}}}$  is a factor relating the motion when it is not moving (rest frame) to a frame where it is moving. Equation 2.15 can also be expressed in as  $\vec{L} = \frac{\vec{p}}{m}c\tau$ , in terms of the particle's momentum  $p$  and mass,  $m$ . A particle with a large mass,  $m$ , produced with a small momentum, will travel slow covering some distance before it decays. Since decay rate,  $\Gamma$ , depends on the coupling, particle decaying through electromagnetic, weak and strong interactions have very different decay rates. Particles decaying through strong interactions have

the largest decay rate and equally shortest lifetime of about  $10^{-17}$  to  $10^{-25}$  seconds. Electromagnetic particle decays have lifetime which can vary from  $10^{-12}$  seconds to about  $10^{-9}$  seconds and weak interactions have lifetimes that can vary from *nanoseconds* to several minutes. Particle lifetime may also vary from a few femtoseconds ( $1 \text{ fs} = 10^{-15} \text{ s}$ ) to the age of the universe or equivalently its measured distance traveled can vary from a few  $\mu\text{m}$  to billions of km [12, 13]. The term *long-lived* particles refers to particles which live long enough to travel a distance comparable to the detector size. This distance traveled might range from a few  $\mu\text{m}$  to meters.

### Neutralino as a Long-Lived Particle

The neutralino as the next-to-lightest-supersymmetry particle (NLSP), can decay into a photon ( $\gamma$ ), Higgsino ( $\tilde{H}^0$ ), Z boson and gravitino ( $\tilde{G}$ ) [14, 15]. The probability for a neutralino ( $\tilde{\chi}_1^0$ ), produced with energy  $E_{\tilde{\chi}_1^0}$  and mass  $m_{\tilde{\chi}_1^0}$  to travel a distance  $x$  before decaying to a photon and gravitino in the laboratory frame can be expressed as  $\mathcal{P}(x) = 1 - \exp\left(-\frac{x}{L}\right)$ , where the distance traveled in a particle detector by the neutralino is given by Equation 2.16.

$$L = \left( c\tau_{\tilde{\chi}_1^0} \right) \cdot (\beta\gamma)_{\tilde{\chi}_1^0} \quad (2.16)$$

From Equation 2.16, it is clear that this distance depends on two main factors. The boost factor,  $(\beta\gamma)_{\tilde{\chi}_1^0} = \frac{|\vec{p}_{\tilde{\chi}_1^0}|}{m_{\tilde{\chi}_1^0}} = \sqrt{\left(\frac{E_{\tilde{\chi}_1^0}}{m_{\tilde{\chi}_1^0}}\right)^2 - 1}$ , which indicates how fast the neutralino is traveling before it decays. For slow moving neutralino,  $(\beta\gamma)_{\tilde{\chi}_1^0} \ll 1$ .

This means that the momentum ( $p_{\tilde{\chi}_1^0}$ ) of the neutralino during production from gluino or squarks decays must be much smaller than the its mass,  $m_{\tilde{\chi}_1^0}$ . Neutralinos, produced, with their mass and momentum satisfying the slow condition,  $p_{\tilde{\chi}_1^0}/m_{\tilde{\chi}_1^0} \ll 1$ , are definitely good candidates for detectable long-lived neutralinos. The other factor is the inherent long lifetime,  $c\tau_{\tilde{\chi}_1^0}$ , of the neutralino. Neutralinos with  $c\tau_{\tilde{\chi}_1^0} > 1$  are long-lived and would make good candidates for detectable long-lived neutralinos. This inherent neutralino lifetime can be expressed as given in equation 2.17.

$$c\tau_{\tilde{\chi}_1^0} \approx \left( \frac{m_{\tilde{\chi}_1^0}}{\text{GeV}} \right)^{-5} \left( \frac{\sqrt{F}}{\text{TeV}} \right)^4 \quad (2.17)$$

$$c\tau_{\tilde{\chi}_1^0} \approx C_{grav}^2 \left( \frac{m_{\tilde{\chi}_1^0}}{\text{GeV}} \right)^{-5} \left( \frac{\sqrt{\Lambda \cdot M_{\text{mess}}}}{\text{TeV}} \right)^4 \quad (2.18)$$

It is important to note that by changing the supersymmetry breaking scale,  $\mathbf{F}$ , the lifetime of the neutralino also changes. In the SPS8 model, the parameter  $C_{grav}$  is used to adjust the inherent lifetime of the neutralino. Thus, we re-write the neutralino lifetime as given in equation 2.18. This equation is used to simulate physics events with the production and decay of neutralino in CMS detector using Monte Carlo (MC) simulations. The supersymmetry breaking scale,  $\Lambda$ , determines the mass of gluino ( $\tilde{g}$ ), squarks ( $\tilde{q}$ ) which decay to the neutralino. Therefore the neutralino momentum,  $p_{\tilde{\chi}_1^0}$  is determined by the masses of gluino and squarks. If the gluino or squark decays to the neutralino in association with a many gluons and quarks seen in the detector as *jets*, then the neutralino momentum is small with the ratio  $p_{\tilde{\chi}_1^0}/m_{\tilde{\chi}_1^0} \ll 1$ , this means the neutralino is slow and therefore long-lived. However, if the gluino or squark is decays with less number of jets, then the neutralino momentum is not so small and the neutralino is not very long-lived. Therefore, the neutralino kinematic properties like its momentum, arrival time at the CMS detector as well as the number of associated jets can be influenced by the gluino or squark decay kinematics.

Using the LHC as the proton-proton collider and the CMS detector as the instrument for detecting and measuring the lifetime of delayed photons produced from long-lived neutralino decays. We have simulated neutralino production and decay according to the SPS8 benchmark model, where the neutralino is the NLSP decaying into a photon and the gravitino as LSP. In Figure 2.8 we show some distributions of kinematic properties like the momentum in the transverse plane of the CMS detector (transverse momentum ( $p_T$ ), since particles produced with enough momentum travel and are detected along the transverse plane of the CMS detector) of the neutralino ( $p_T^{\tilde{\chi}_1^0}$ ) and its measured lifetime ( $c\tau_{\tilde{\chi}_1^0}$ ) in the CMS detector. We also made distribution showing transverse momentum of the photon ( $p_T^\gamma$ ) and the measured arrival time of the photon ( $T_\gamma$ ). These distributions are made for different model parameters  $\Lambda$  and  $C_{grav}$ . The CMS Software (CMSSW) package has been used to simulate and study the neutralino production and decay in CMS detector while the root data analysis framework was used to performed some fit analysis on the generated and simulated distributions of the distance traveled by neutralino before decay to extract its  $c\tau_{\tilde{\chi}_1^0}$  produced during the

MC generation. The extracted  $c\tau_{\tilde{\chi}_1^0}$  value is compared to theoretical prediction values for consistency check of the simulation process.

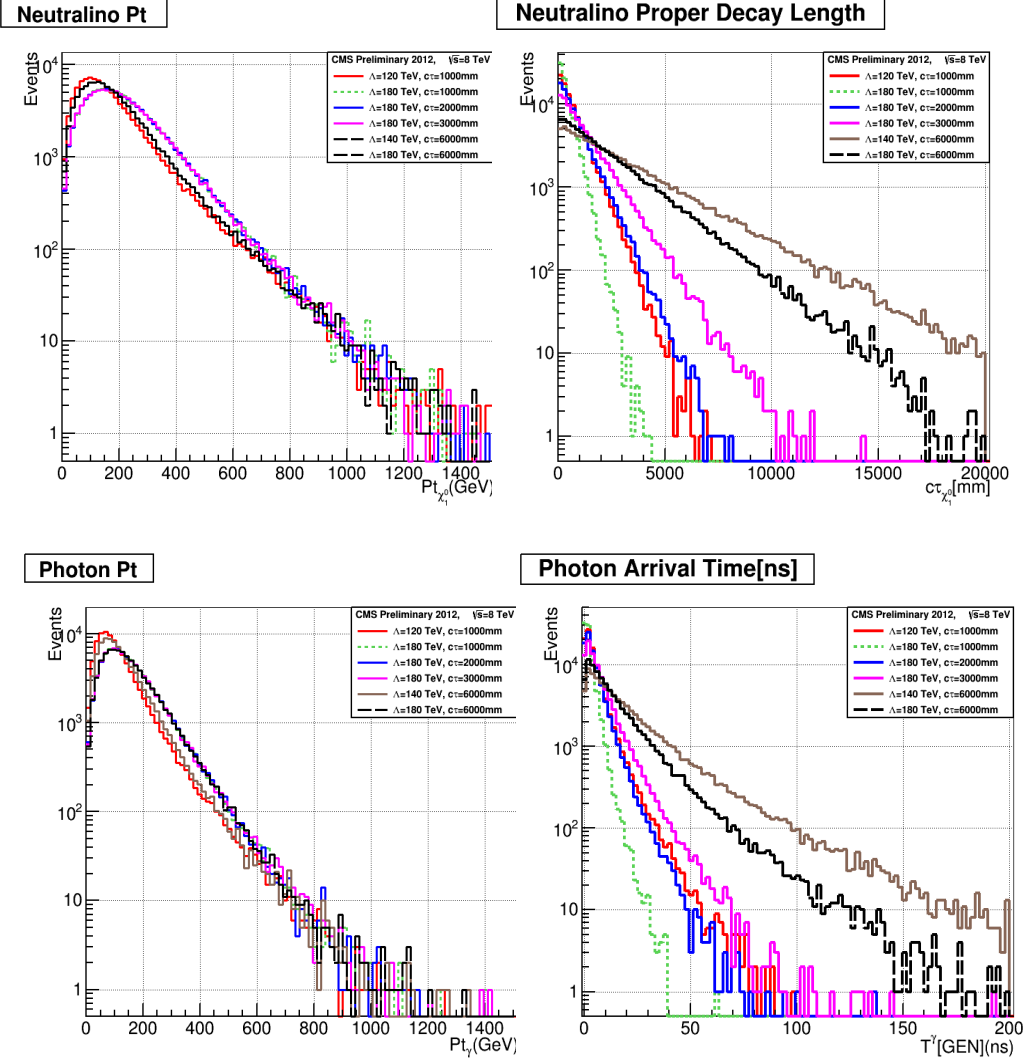


Figure 2.8: Neutralino transverse momentum distribution (top left) and proper decay length (top right) with its decayed photon transverse momentum distribution (bottom left) and time of arrival at ECAL (Bottom right) for GMSB SPS8 model.

## 2.4 Previous Search Experiments

The have been previously other search experiments for neutral long-live particles decaying to photons. Obviously, negative findings from these experiments led to possible search exclusion regions in terms of the lifetime, mass and cross section of the existence of supersymmetry particles in different supersymmetry models. Results from experiments(DO, CDF, CMS and ATLAS) [16, 17, 18, 19, 20] of the search for Neutralino NLSP decaying to photon and gravitino interpreted using the SPS8 benchmark model is shown in 2.9. These results show that within the SPS8 model, neutralinos with mass  $m_{\tilde{\chi}_1^0} \leq 245$  GeV and proper decay length  $c\tau_{\tilde{\chi}_1^0} \leq 6000$  mm have not been found at hadron colliders. The diagram on the left of figure 2.9 are exclusion results in the neutralino mass or supersymmetry breaking scale  $\Lambda$  on the horizontal axis and the nuetralino lifetime,  $c\tau_{\tilde{\chi}_1^0}$  on the vertical exis from the 7 TeV search analysis by the ATLAS experiment while the diagram on the right is that for CMS experiment. The colored regions on the plots shows the parameter space where these searches have been performed and the findings were negative.

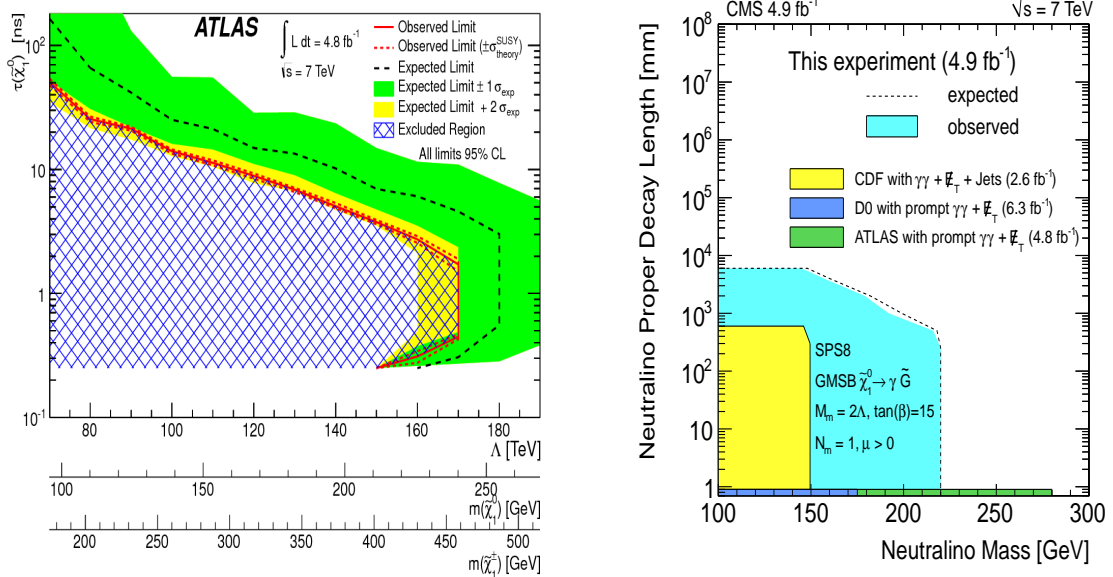


Figure 2.9: Neutralino lifetime and mass upper limit from ATLAS(left) and CMS(right) 7 TeV analysis with non-pointing photons and MET.

# **Chapter 3**

## **Hadron Collider and Detector**

This section describes the particle collider and detector. The first section describes the particle accelerator which is the Large Hadron Collider (LHC) and the next section describes the Compact Muon Solenoid (CMS) detector with emphasis to those sections directly relevant to this analysis. A detailed description of the LHC and CMS detector is found in Ref.[21] and Ref.[22].

### **3.1 Large Hadron Collider**

#### **3.1.1 Overview**

The LHC is a proton-proton and heavy ion collider designed to achieve a center of mass  $\sqrt{S}$  energy of 14 TeV. It is hosted by the European Organisation for Nuclear Research (CERN). Unlike linear colliders, the LHC is a circular collider with nearly 27 km in circumference located at the border between France and Switzerland. It is designed to smash protons and ions against each other controlled by powerful magnets at four main points. The Compact Muon Solenoid (CMS) is one of the multi-purpose particle detectors at each collision point. Fig. 3.1 shows the LHC and the different stages before particle collision.

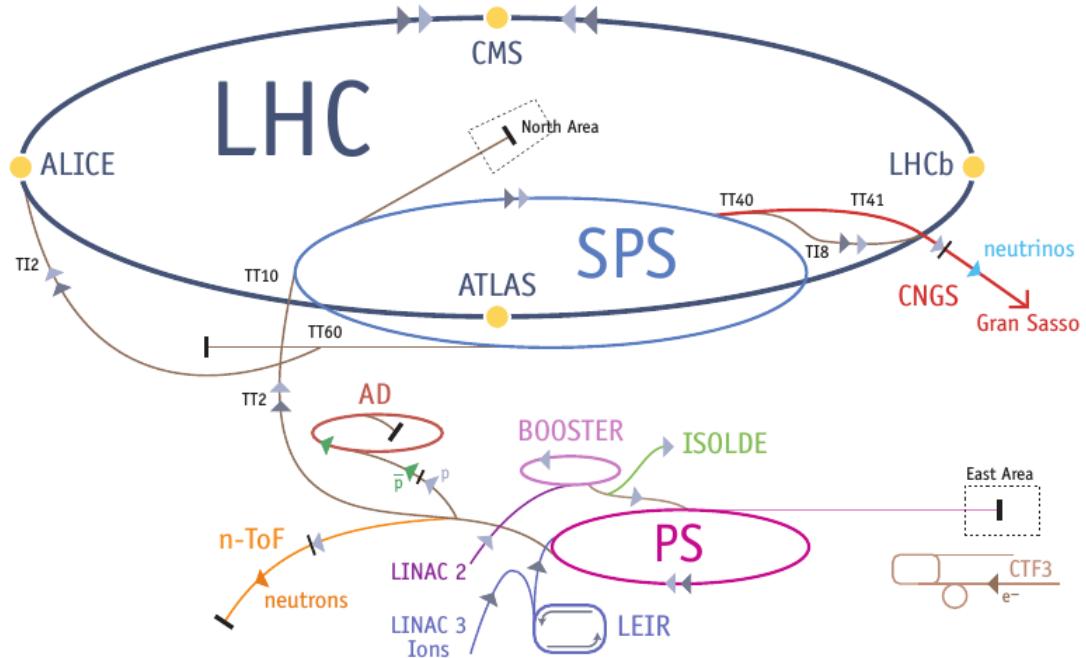


Figure 3.1: Schematic diagram showing the full Large hadron Collider.

### 3.1.2 Colliding Energy

Hydrogen ions also known as protons from hydrogen gas where the orbiting electron has been stripped away is inserted into a linear accelerator called *Linac 2*. Using electromagnetic fields in Radio Frequency (RF) cavities, these protons are accelerated to an energy of 50 MeV creating a stream of particles called *particle beams* arranged in packets known as *bunches*. Protons from the Linac2 are injected into the circular synchrotron Booster (PSB). The circular synchrotron accelerator ensures that the protons pass many times through a cavity with their energy slowly increasing each time to reach the design energy. The PSB accelerates the protons up to 1.4 GeV and inject them into the Proton Synchrotron (PS) which increases their energy to 25 GeV. These protons traveling at 99.93% the speed of light are sent to the Super Proton Synchrotron (SPS) and accelerated to an energy of 450 GeV. They are finally transferred into the LHC ring(accelerating in a clockwise and anti-clockwise direction) and accelerated for about 20 minutes to their nominal energy of 7 TeV. By now the protons are traveling with the

speed of 99.9999% the speed of light. Powerful bending magnets are used to keep the beams traveling in the circular LHC ring. The advantage of circular particle colliders over fix target is that, the energy available to make new particles called the *center of mass* (COM) energy, denoted as  $\sqrt{S}$  is simply the sum of the energy of the two beams i.e.  $\sqrt{S} = E_{\text{beam1}} + E_{\text{beam2}}$  compared to  $\sqrt{E_{\text{beam}}}$  for fix target experiments. For the LHC, each beam is designed to have energy of 7 TeV making  $\sqrt{S} = 14$  TeV. In circular colliders, synchrotron radiation (is inversely proportional to the mass of the charge particle to the fourth power) by an accelerating charge particle contributing to loss its energy. This would require a continuous addition of energy after each turn to maintain the beam energy to a stable value. However, since the proton's mass is about 0.938 GeV, and are to be accelerated to about 7 TeV, this loss of energy is not very significant unlike for electrons whose mass is about 0.000511 GeV and the energy loss is more. Thus protons are preferred to electrons for a circular collider. Then again, the debris of particles produced when electrons collide is much less compared to that of protons making analysis in a hadron collider very challenging.

### 3.1.3 Luminosity

In colliding beams experiments, the center of mass energy available for the production of new effects is very important. However, the number of useful interactions producing effects (events) is equally important, especially in cases where the probability (also known as cross section,  $\sigma$ ) of producing rare events is very small. The quantity which measures the ability of a particle accelerator to produce the events from the required number of interactions is called *luminosity*. The luminosity is also the proportionality factor between the number of events per second and the cross section. Luminosity ( $\mathcal{L}$ ) is therefore a measure of the number of collisions that can be produced in a collider per squared area per second. The cross section is calculated from theory while the luminosity depends on factors ranging from the flux i.e. number of particles per second of the beams, the beam sizes at collision, and the frequency of collision. For physics experiments, the integrated luminosity which is total luminosity over a given period of time usually a year gives the amount of data that has been recorded by a given detector.

Using the luminosity ( $\mathcal{L}$ ) and the cross section ( $\sigma_p$ ) of a given process, we can calculate event rate ( $\mathcal{R}$ ) or the number of events per second produced in proton collisions

by the given interaction process. By calculating the event rate, we are measuring a given cross section ( $\sigma_p$ ) through  $(\sigma_p = \frac{\mathcal{R}}{\mathcal{L}}$  in order to prove or disprove theories which make prediction on  $\sigma_p$ .

$$\mathcal{R} = \mathcal{L} \cdot \sigma_p \quad (3.1)$$

In CMS we have a “recorded” and “delivered” luminosity. Delivered luminosity refers to the luminosity delivered by LHC to CMS and one would expect this to be equal to the amount recorded. However, there are instances where the CMS detector is unable to take data either because the data acquisition chain (DAC) or one of the CMS sub-detectors is temporarily down and also trigger dead time. Figure 3.2 shows the total integrated luminosity delivered by LHC and recorded using the CMS detector during the 8 TeV proton-proton collision by the LHC.

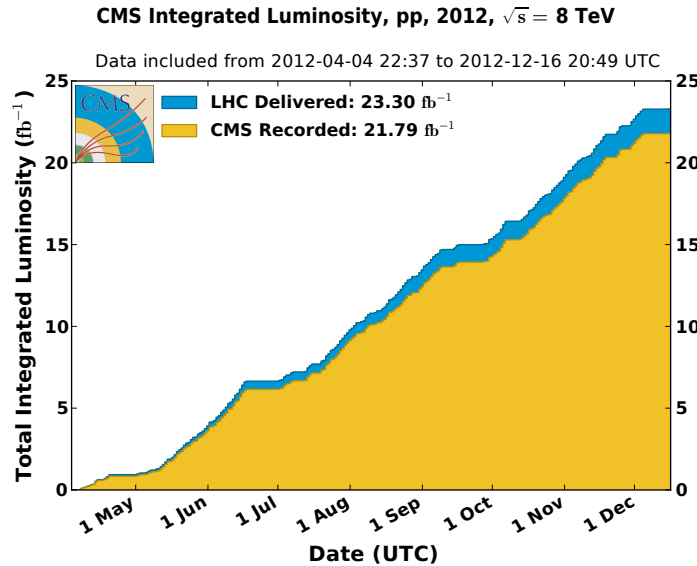


Figure 3.2: Cumulative luminosity versus day delivered to (blue), and recorded by CMS (orange) during stable beams and for p-p collisions at 8 TeV center-of-mass energy in 2012.

### 3.1.4 LHC Bunch Structure

Each LHC proton bunch is placed inside an RF buckets during beam filling. The filling scheme is such that not all RF buckets have proton bunches. Those empty buckets or beam gaps are necessary to avoid parasitic collision near IP and to make room for beam

dump and beam halos known as beam cleaning. The separation in time between two buckets/bunches filled or unfilled is approximately 2.5 ns. There are about  $10^{11}$  protons per bunch during filling and acceleration. However, during filling and eventual bunch splitting at PS, it is possible that some empty buckets are filled with a much smaller proton population compared to the main bunch. These buckets with few protons can be either trailing the main bunch by  $\Delta t = 2.5, 5.0, 7.5, \dots$  ns, or leading the main bunch by  $\Delta t = -2.5, -5.0, -7.5, \dots$  ns. If these less populated bunches are 2.5 to 3.0 ns spaced in time from each other, they are referred to as *satellite* bunches and if 5.0 ns, they are referred to as *ghost* bunches. Figure 3.3 shows ghost and satellite bunches and a main proton bunch.

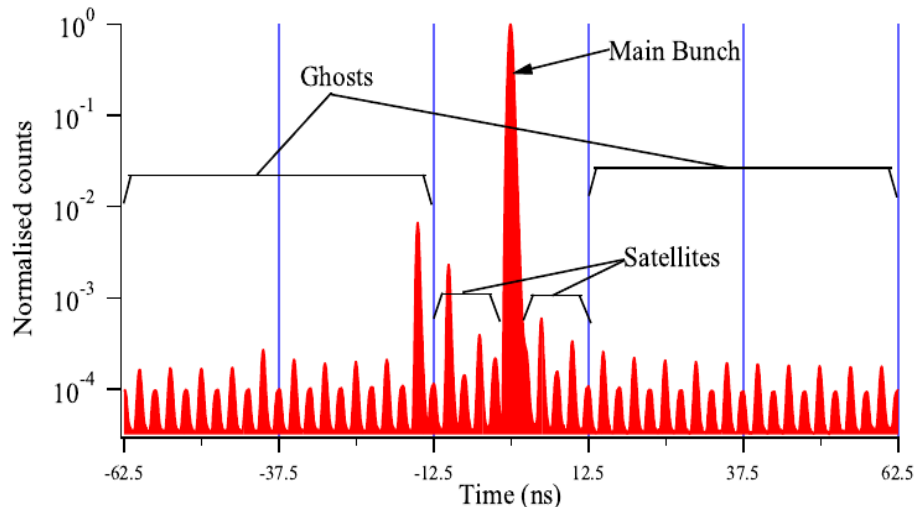


Figure 3.3: Longitudinal Profile taken with Longitudinal Density Monitor (LDM) detector showing definition of Ghost/Satellite bunches with respect to main bunches.

The presence of ghost/satellite bunches increases the uncertainty in LHC luminosity measurements and can also generate proton-proton interactions near but not at the collision region. Effects on ghost/satellite bunches on instantaneous luminosity measurements have been studied using CMS, ATLAS and ALICE detectors. Their results showing clear observation of physics events produced from ghost and satellite bunch collisions is shown in figure 3.4. CMS uses energy deposits in the endcap calorimeters to observe time space which is consistent with the expectation from ghost/satellite bunches while in ATLAS uses the Longitudinal Density Monitor (LDM) detector to

study ghost/satellite bunches.

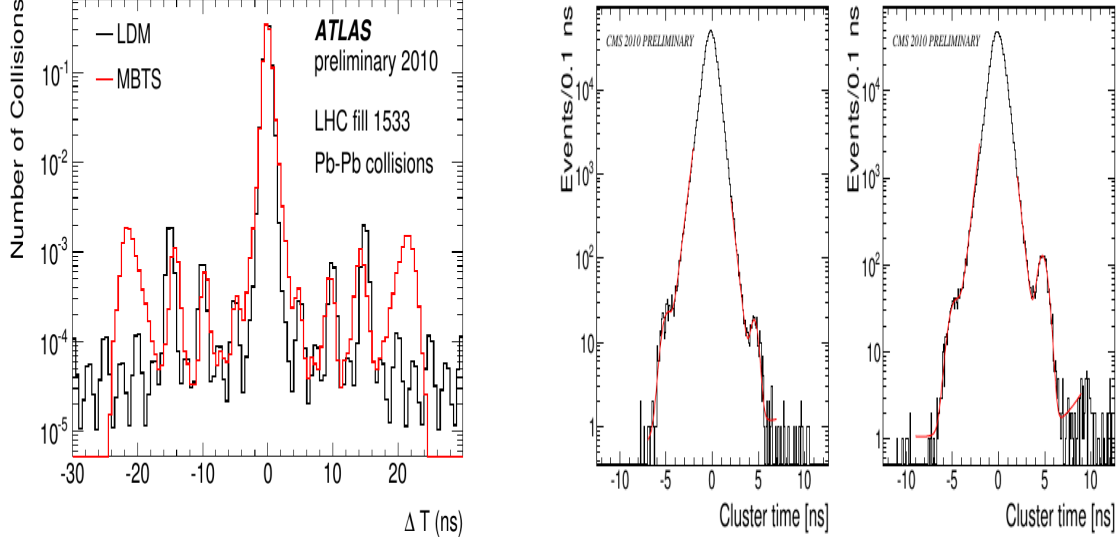


Figure 3.4: (left) Arrival time distribution(red) of ATLAS MBTS for LHC fill 1533 during 2010 Pb-Pb run and LDM profile(black) for Beam2(same for Beam1). (Right) Timing of Clusters in the CMS endcap calorimeters for fill 1089:Left: EEP detector(left side of IP  $z > 0$ ) Right: EEM detector( right side of IP,  $z < 0$ ). Plots from ATLAS Ref.[30] and CMS, Ref.[31]

Table 3.1 gives a summary of the LHC design conditions compared to the conditions used during the LHC RUN 1 operation.

LHC Operation Parameters 2010-2013					
Parameter	2010 value	2011 Value	2012/13 Value	Design	Value
Beam energy[TeV]	3.5	3.5	4.0	7	
$\beta^*$ in IP 5[m]	3.5	1.0	0.6	0.55	
Bunch spacing [ns]	150	75/50	50	25	
Number of bunches	368	1380	1380	2808	
Protons/bunch	$1.2 \times 10^{11}$	$1.45 \times 10^{11}$	$1.7 \times 10^{11}$	$1.15 \times 10^{11}$	
Normalised emittance[mm.rad]	$\approx 2.0$	$\approx 2.4$	$\approx 2.5$	3.75	
Peak luminosity[ $cm^{-2}s^{-1}$ ]	$2.1 \times 10^{32}$	$3.7 \times 10^{33}$	$3.7 \times 10^{33}$	$1 \times 10^{34}$	
Evts/bunch crossing	4	17	37	19	
Stored Beam energy(MJ)	$\approx 28$	$\approx 110$	$\approx 140$	$\approx 362$	
Int. Luminosity by CMS[ $pb^{-1}$ ]				-	
Circumference[km]	26.659	26.659	26.659	26.659	
Dipole Magnet B[T]	8.33	8.33	8.33	8.33	

Table 3.1: LHC operation parameter conditions during RUN 1, 2010-2013

## 3.2 Compact Muon Solenoid

### 3.2.1 Overview

The Compact Muon Detector (CMS) is a modern particle detector design for many different particle detection capability. It is one of the general purpose detectors located at one of the proton-proton collision points along the 27 km LHC ring. Its main feature is the presence of a superconducting solenoid of 6 m internal diameter providing a field of 3.8 T for measuring a charge particle's momentum as the particle bends under the influence of this field traveling in the detector. This magnetic field encloses an entirely silicon pixel and strip tracker detector used for vertex finding and for detecting and reconstructing the tracks of charged particles, a lead-tungstate scintillating-crystals electromagnetic calorimeter (ECAL) and a brass-scintillating sampling hadron calorimeter (HCAL). Very long lived particles like muons are measured in gas-ionization detectors embedded in the flux-return iron-yoke located at the outermost section of the detector. It has a simple cylindrical structure consisting of barrel and endcap detectors and an extensive forward calorimetry and detectors to provide a near  $4\pi$  solid angle coverage assuring good hermetic particle detection. The CMS apparatus has an overall length of 21.6 m, a diameter of 14.6 m, and weighs 12,500 tons. Figure 3.5 shows the CMS detector indicating the different sub-detectors and their material design type. We provide a performance summary and material type of each sub-detector in Table 3.2 of the CMS detector. The CMS uses a coordinate system with the origin coinciding with the center of the detector where proton-proton or nominal collision occurs. This point is commonly referred to as the *interaction point* (IP). The direction of  $x$ ,  $y$ , and  $z$ -axes are as shown in figure 3.6. However, for particle identification, CMS uses a more convenient coordinate system based on the polar coordinates. In this polar coordinate system, the azimuthal angle,  $\phi$ , is measured in the  $x - y$  plane, where  $\phi = 0$ , is the  $x$ -axis and  $\phi = \pi/2$ , the  $y$ -axis. The radial distance in this plane is denoted  $R$  and the polar angle  $\theta$  measured from the  $z$ -axis is related to *pseudo-rapidity*,  $\eta$ , through the relation;  $\eta = -\ln \tan(\frac{\theta}{2})$ . The coordinate system  $(\eta, \phi)$  and its radial distance  $R$  identifies a point in the cylindrical volume of the CMS detector. In the coming sections, we describe the geometry, material characteristics and functionality of the CMS subdetectors used in our analysis.

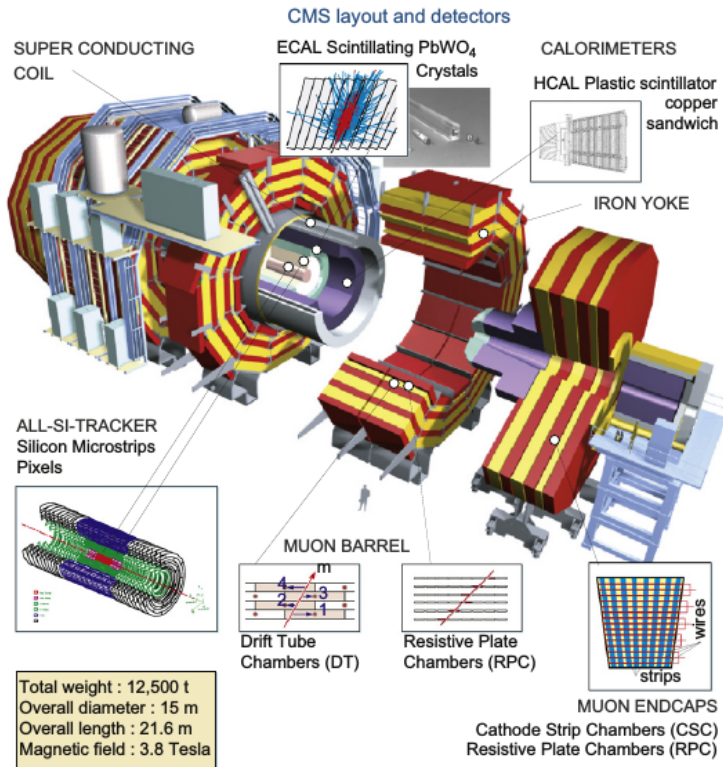


Figure 3.5: CMS Detector showing the different subdetectors and their material.

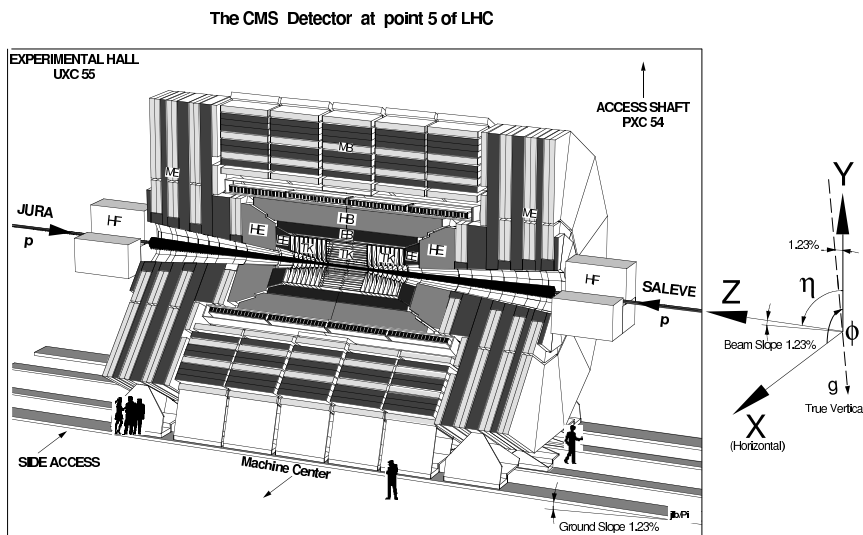


Figure 3.6: CMS detector schematic view with definition of  $x - y - z$  coordinates.

### CMS Detector and Resolution

Subdetector	Quantity	Resolution	Uses
Tracker	Momentum[GeV/c]	$\sigma_T/p_T \approx 1.5 \times 10^{-4} p_T + 0.005$	Silicon Pixels and Strips
ECAL	Energy[GeV]	$\sigma/E \approx 3\%/E + 0.003$	PbWO <sub>4</sub> Crystals
ECAL	Time[ns]	$\sigma(\Delta t) = \frac{N}{A_{eff}/\sigma_n} \oplus \sqrt{2}\bar{C}$	PbWO <sub>4</sub> Crystals
HCAL	Energy[GeV]	$\sigma/E \approx 100\%/E + 0.05$	Brass + Scintillator
Muon Chambers	Momentum[GeV/c]	$\sigma_T/p_T \approx 1\% \text{ at } 50 \text{ GeV to } 10\% \text{ at } 1 \text{ TeV}$	inner tracker + Muon Systems
Magnetic field	B-field strength[T]	3.8 T + 2 T	Solenoid + Return Yoke
Triggers	On/Off-line	Levels	L1(On-line) +HLT(Off-line)(L2+L3)

Table 3.2: CMS detector material, Ref.[22], and resolution(Time resolution:  $N \approx 35$  ns,  $\bar{C} \approx 0.070$  ns Ref. [39])

#### 3.2.2 Calorimeter

A CMS calorimeter absorbs a good fraction of energy of an incident particle and produces a signal with an amplitude proportional to the energy absorbed. This absorption is through the cascade production of secondary particles with energy of the incident particle directly proportional to the number of secondary particles produced. There are two types of calorimeters choices used in the CMS detector; the *Electromagnetic calorimeter* (ECAL); for absorbing the energy of electromagnetic particles such as photons and electrons and a *Hadronic calorimeter* (HCAL) made of more than one type of material for stopping and absorbing the energy of hadrons such as kaons and pions through strong interactions. The combined calorimeter detectors of CMS covers a region in  $|\eta| < 5$  making it nearly hermetic for good missing energy measurements. The ECAL

and HCAL are arranged in a nested fashion shown in figure 3.7 so that electromagnetic particles can be distinguished from hadronic particles by comparing the depth of the particle shower penetration in both calorimeters.

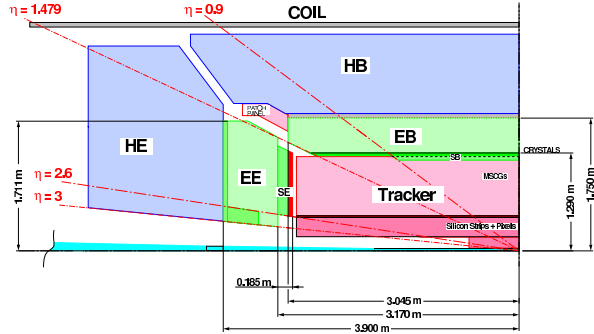


Figure 3.7: Schematic diagram of CMS calorimetry system with HCAL enclosing ECAL in the Barrel and Endcap regions.

### Electromagnetic Calorimeter

The electromagnetic calorimeter (ECAL) detects photons and electrons. High energy photons and electrons are detected through their interaction with the lead tungstate ( $\text{PbWO}_4$ ) crystals. During this interaction which happens either through electromagnetic showering or electron-positron pair production (*bremsstrahlung*), the incoming photon or electron deposit practically almost all of its energy. There are 75848 crystals in total mounted in a cylindrical geometry, with a barrel (EB) and an endcap (EE) structure. The choice of  $\text{PbWO}_4$  crystals as calorimetry material by CMS for operation in the LHC environment is because of its a high density ( $8.28 \text{ g/cm}^3$ ), short radiation length ( $X_0=0.89 \text{ cm}$ ) and a small Molière radius (22 cm). In a high radiation dose and fast timing (25 ns proton bunch spacing) environment like the LHC,  $\text{PbWO}_4$  crystals is preferred to other crystal materials for its high radiation resistance and a scintillation decay time which is comparable to the LHC bunch crossing interval of 25 ns and about 80% of the light is emitted in 25 ns. The probability of an electromagnetic object with high energy to interact either through *Bremsstrahlung* or *pair production* with the material in ECAL is proportional to the nuclear charge,  $Z$ , of the material.  $\text{PbWO}_4$  is a high  $Z$  material and this makes it once more the preferred material choice for electromagnetic calorimetry by CMS. The small Molière radius ensures that on average about

95 % of the electromagnetic shower energy is contained within a crystal crystal volume of about 9 crystals. This reduces the transverse spread of the electromagnetic cascade from multiple scattering of electrons and helps improve on the estimation of the transverse position of impact of an incident particle. It also provides a fine granularity for measuring the particle's energy by providing fewer overlap of particle signals. Its dense nature also allows for the electromagnetic shower to develop early and therefore likely to be fully contained within a compact device like CMS.

The EB section of the ECAL covers a pseudo-rapidity of  $|\eta| < 1.479$ . It has 61,200 crystals providing a granularity of 360 degree fold in  $\phi$  and  $(2 \times 85)$ -fold in  $\eta$ . The crystals are mounted in a quasi-projective geometry so that their axes make an angle of 3% with respect to a line vector from the nominal interaction vertex in  $\eta$  and  $\phi$  directions. This avoids cracks aligned with a particle's trajectory. A crystal in EB is approximately  $0.0174 \times 0.0174$  in  $\eta - \phi$  or  $22 \times 22 \text{ mm}^2$  at its front face and  $26 \times 26 \text{ mm}^2$  at its rear face. Each crystal is 230 mm long corresponding to about  $25.8 X_0$  radiation lengths. The crystal's radial distance measuring from the center of the face of the crystal to the beam line is 1.29 m. A number of crystals are placed in a thin-walled alveolar structure made with aluminum forming a *submodule*. Each submodule is arranged into 4 modules of different types according to their  $\eta$  position. There are about 400 to 500 crystals in each module and these 4 combined make one *supermodule* containing 1700 crystals. To reduce crystal reflective lost, the aluminum surface is coated to avoid oxidation leading to coloration. On the rear end of each EB crystal, two *Avalanche Photodiodes* (APD) is glued to collect the scintillating light from the crystals converting light into charge current which is further collected by the read-out electronics.

The endcap sector covers a pseudo-rapidity region of  $1.479 < |\eta| < 3.0$  with a Preshower (ES) detector made of silicon strip sensors interleaved with lead placed immediately in front of it. The purpose of the preshower is to identify photons from the decay of neutral pion,  $\pi^0 \rightarrow \gamma\gamma$  and also to help separate photons producing electrons through pair production from photons not producing electrons before their arrival at the EE. The endcap located on the  $+z$  side of the nominal interaction is denoted EE+ while the other located on the  $-z$  side is denoted as EE-. The longitudinal distance between the IP and the center of the surface of the EE crystals is 3.154 cm. Each endcap is divided into two halves called *Dees* with each Dee holding 3662 crystals. Crystals in EE with identical shape

are grouped into  $5 \times 5$  units called *supercrystals* (SC). The crystals in the SC form an  $x - y$  grid. Each crystal is 220 mm ( $24.7 X_o$ ) in length and has a front face and rear cross section of  $28.62 \times 28.62$  square mm and  $30 \times 30$  square mm, respectively. Vacuum Phototriodes (VPT) instead of APDs is glued on the rear face of each crystal for scintillating light conversion into electrical signals. The VPT is used in the EE because of its high resistance to radiation and smooth operation in a strong magnetic field environment. These APDs and VPTs are used because of their high gain relative to regular photodiodes with no gain and the fact that they are not affected by the high magnetic field. Although the light yield for  $\text{PbWO}_4$  crystals is rather low ( $\approx 70$  photons/ MeV), these photo-detectors have internal gain (50 for APDs and 10 for VPTs) and quantum efficiency of 75 % for APDs and 20 % for VPTs of the emission wavelength. This makes it possible that signals from incident particles with energies of a few to high GeV longer than noise.

The signals from the APDs and VPTs are digitized by voltage-sensitive analogue-to-digital converters and through fibre-optic links transported as light signals to the counting room located adjacent to the experimental cavern.

The energy resolution and geometry structure of the ECAL ensures that the photon or electron's arrival energy, time, position and even the direction through the shape of its electromagnetic shower in the crystals can be identified and measured with good precision.

### **Hadronic Calorimeter**

The CMS Hadron Calorimeter (HCAL) is comprised of four distinct subdetectors: the Barrel (HB), the Endcap (HE), the Outer Barrel (HO), and the Forward (HF). Unlike the ECAL, the HB, HE and HO subdetectors are scintillator-sampling calorimeters with embedded wavelength shifting fibers (WLS). HB, HE and HO uses brass plates as the inactive material and plastic scintillator with WLS as the active material. The brass plate is used for absorbing the hadronic shower which comprise of an *electromagnetic*(particles like  $\pi^0$ s,  $\eta$ s and other mesons generated in the absorption process and decay to  $\gamma$ s which develop electromagnetic (em) showers) and *non-electromagnetic* components. The plastic scintilator is divided into 16  $\eta$  sectors resulting in segmentation of  $\Delta\eta \times \Delta\phi = 0.087 \times 0.087$ . It was chosen for its long-term stability and moderate

radiation hardness. energy. The scintillating light through the WLS brings the light to hybrid photodiodes (HPDs) in the HB and HE. HPDs which have high electrical noise and will be replaced with silicon photon multipliers (SiPM) which have low noise during the current CMS detector upgrade. The HB and HE combine cover a region in pseudo-rapidity of  $|\eta| < 3$ . The HB covering the region  $|\eta| < 1.3$ , is divided into two-half barrel (HB+ and HB-) sections each composed of 18 identical  $20^\circ$  wedges in  $\phi$ . Each wedge is made of flat brass alloy and steel(only front and back plates) absorber plate. HE covers  $1.3 < \eta < 3.1$  and has plastic scintillation tiles with granularity of  $\Delta\eta \times \Delta\phi = 0.087 \times 0.087$  for  $|\eta| < 1.6$  and  $\Delta\eta \times \Delta\phi = 0.17 \times 0.17$  for  $|\eta| > 1.6$ . The HO is an extension of HB outside the solenoid and thus utilizes the solenoid coil as an additional absorber. It is used to identify the starting shower and to measure the shower energy deposited after HB. The first active layer of the scintillating tiles is situated directly behind the ECAL in order to actively sample low energy showering particles from the support material between the ECAL and HCAL.

The HF occupies a pseudo-rapidity region of  $3 < |\eta| < 5$ . Its purpose is to provide a closer to  $4\pi$  hermetic phase space coverage required for missing transverse energy calculation or MET. MET is the established signal for very weakly interacting particles like neutrino and supersymmetric particles like gravitino which travel through the detector undetected. HF consists of radiation hard quartz fibers embedded in steel absorbers running parallel to the beam axis. The signal from Cherenkov light emitted in the quartz fibers in response to charged particles makes it possible to detect all charge particles in the forward region. The HF calorimeter has long and short fibers for better sampling and to distinguish showers generated by electrons and photons from those generated by hadrons. The choice of quartz fibers is because of its high resistance to the high radiation in the forward detectors and its fast production of light through Cherenkov process.

For  $|\eta| < 1.48$ , the HCAL cells map on to  $5 \times 5$  ECAL crystal arrays to form calorimeter towers projecting outwards from near the nominal interaction point. In each tower, the energy in ECAL and HCAL cells is summed to define the calorimeter energy tower. The energy ratio of an HCAL tower to an ECAL in a calorimeter energy tower can be used to improve photons and electron identification.

### 3.2.3 Muon Chambers

Muons unlike electrons and hadrons do not deposit most of their energy in the calorimeters. They are capable of traveling across the entire CMS detector into the muon chambers. Muons produce tracks which run across the CMS detector starting from the silicon pixel and strip subdetector closest to the IP called the *Tracker* and depositing very little fraction of their energy in the calorimeters unto the muon chambers. The muon chambers use the process of ionization and a 2 T magnetic field from the return iron yokes (bending the tracks of charge particles) to measure the momentum of charged particles. The three different types of muon chambers used by the CMS are: the drift tubes (DT) chambers in the barrel, cathode strip chambers (CSC) in the endcaps and resistive plate chambers (RPC) glued to the DT and CSC chambers. Four layers or stations of DT/RPC and CSC/RPC are embedded in an interleaved style with the iron yoke for track reconstruction and triggering. Figure 3.9 is a longitudinal view of the CMS detector showing the position of the muon stations. The DT and CSC record track segments characterized by the position of the track and the bending angle. This information is used to determine the precise transverse momentum and charge of particles during particle reconstruction. The RPCs(DTs and CSC will also be used after the current detector upgrade) are dedicated L1 trigger chambers used to determine the candidate muon's approximate transverse momentum and proton bunch crossing number. The RPC has a timing resolution of about 3 ns.

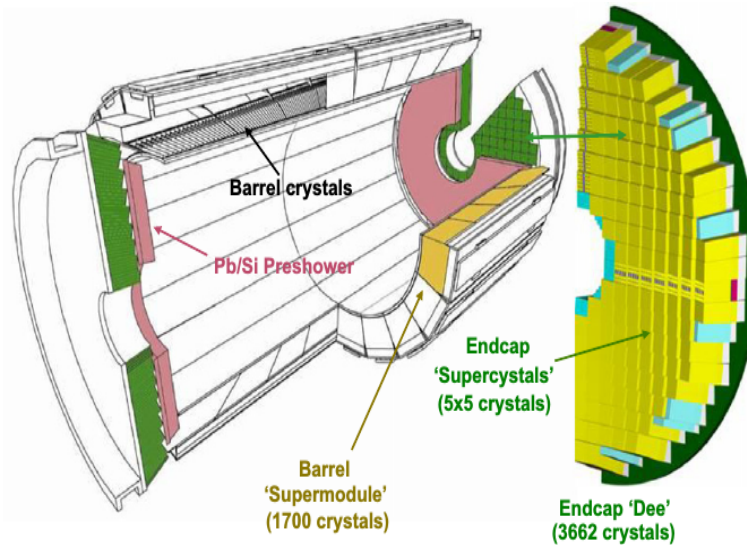


Figure 3.8: Layout of the CMS electromagnetic calorimeter showing the arrangement of crystal modules, supermodules in the barrel with the preshower in front of endcap with supercrystals.

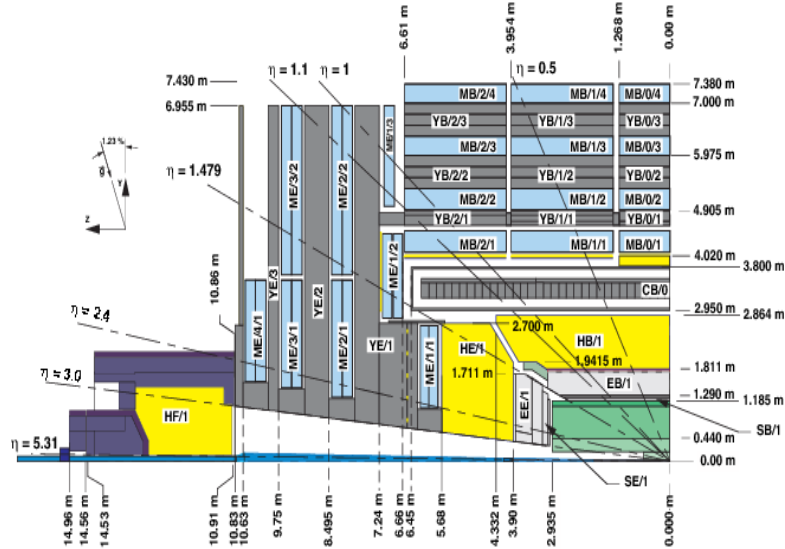


Figure 3.9: Cross section view showing the coverage range of CMS sub-detectors and their longitudinal distance from the IP.

### 3.2.4 Triggering

In CMS, there are a billion interactions including *pile up* (PU) happening each second. This means data from each 25 ns proton-proton collision has to be processed and stored before the next collision happens. Also, since not all these collisions produce interesting physics events, we have to be capable of selecting only interesting physics events produced from proton-proton collisions with sufficient energy. The process of selecting such interesting events is called *triggering*. CMS uses a two level triggering system for selecting interesting events produced with enough energy from collisions. The comprise of the *Level-1* (L1) and *High Level Triggers* (HLT) triggers.

The L1 triggers is a hardware designed electronics system implemented in FPGA and ASIC technology and uses information from the calorimeter, muon trigger and a global trigger board. The global trigger board makes the final decision based on the calorimeter and muon triggers to reject or keep an event for further processing at the HLT trigger. The L1 trigger is responsible for selecting the best 100,000 events/second from the initial 1 billions events/second produced.

The HLT is a software comprised of implemented selection algorithms running on a farm of more than 1000 standard computers. These complex algorithms include instructions like, match tracks to hits from the muon chambers, select energy deposits above a certain threshold in the calorimeters with no tracks for electromagnetic objects, and begins the first step of event selection. Just like the L1 trigger, the HLT uses assimilated and synchronized information from different parts of the CMS detector to create the entire event. By the time this selection process is complete, there are now only 100 events/second with the remaining 99,900 thrown away. Taking an average event size to be 1 Megabyte, in a stable and effective LHC proton collision period of a year or  $10^7$  seconds, CMS produces about a Petabyte of data which is stored and used later for offline physics analysis.

## Chapter 4

# Time Reconstruction and Resolution

### ECAL Time Overview

The ECAL was designed to precisely measure the energy for electrons and photons produced in proton-proton collisions, with a target barrel resolution of 0.5% for photons with energies larger than 50 GeV. In addition to energy measurements, the combination of fast scintillation for PbWO<sub>4</sub> crystals, the electronic pulse shaping and sampling rate of 40 MHz allow for excellent time measurements to be made with ECAL. A pulse shape matching of less than 1% non-linearity by the pulse shaping chip in each channel, ensures a linear and uniform pulse height from among all the channels in the ECAL.

The time measured by each channel is reconstructed from 10 discrete samples of the digitized analog pulse height of the electronics, using a time reconstruction algorithm. Since the electromagnetic shower of the electromagnetic particle normally spreads across several crystals (meaning several channels involved), a cluster of about 25 crystals (or *supercluster*) after reconstruction contains all of the particle's energy. As a result the arrival time of an electromagnetic particle is defined either using the reconstructed time ( $t_{reco}$ ) of a single channel, which is the crystal with the highest energy (*seed crystal*), or an error ( $\sigma$ ) weighted average of all the individual reconstructed time of each crystal belonging to the supercluster. A supercluster can be made of many smaller clusters called *basic clusters*, and the seed basic cluster (cluster with highest energy) time can

equally be used as the particle's measured arrival time. We write  $t_{seed}$  for the seed time and  $t_{Ave}$  for the average time defined in Equation 4.1.

$$t_{Ave} = \frac{\sum_{i=1}^N \frac{t_{reco,i}}{\sigma_i^2}}{\sum_{i=1}^N \frac{1}{\sigma_i^2}}, \quad (4.1)$$

Where  $N$  is the number of crystals of the supercluster,  $t_{reco,i}$  and  $\sigma_i$  are the time and uncertainty on the reconstructed time of each channel, respectively.

## 4.1 Electromagnetic Calorimeter Readout Electronics

The scintillating light from the PbWO<sub>4</sub> crystals is readout and converted into electric current using Avalanche Photo-Diodes (APD) and Vacuum Photo-Triodes (VPT) in the barrel and endcap detector regions, respectively.

The ECAL electronics readout and control system is made of the Front End (FE) electronics ( board consists of radiation hard ASIC chips) installed inside the detector volume at the back of ECAL and the Off Detector (OD) electronics in the upper counting room. Both electronics systems are connected by 100 m radiation hard Gigabit Optical fiber Links (GPOL) for transporting the optical data stream.

The FE follows the crystal arrangement in matrixes of  $5 \times 5$  crystals called *Trigger Towers* in barrel and *Super-Crystals* in the endcap. Each FE board hosts five Very Front End (VFE) boards with each holding five analog channels. Each channel consists of a Multi-Gain Pre-Amplifier (MGPA) and a 12 bit Analog-to-Digital Converted (ADC) used to amplify, shape and digitize the signal coming from the Photo-Diodes.

The MGPA chip uses 3 gain ranges with gain ratios of 1,6 and 12 to span the overall dynamic range of the signal. Equipped with a CR-RC filter with a pulse shaping time of 40 ns and less than 1% of non-linearity, the MGPA ensures a linearity and pulse shape matching across all three ranges which allows for precise pulse shape reconstruction.

The readout and precision performance requires a multi range 12-bit ADC chip with a sampling frequency of 40 MHz to digitize the analog pulse signal of the highest unsaturated range into 10 discrete samples, with an electronic noise of about 40 MeV.

The digitized data are stored in pipeline buffers until a Trigger Level 1 (LV1) accept

decision is made. At the same time the digitized data are sent to a digital signal processing FERNIX chip which performs trigger primitive generation (TPG) for the LV1 trigger system. The TPGs are sent to the Trigger Concentration Card (TCC) on the OD electronics at a rate of 1 word/25 ns. Upon a positive trigger LV1 decision, the data samples corresponding to a single event are transferred to primary event buffers which are eventually merged and sent to the Data Concentration Card (DCC) through Readout links at 800 Mbps.

The FE board also is also equipped with a Clock and Control Unit (CCU) chip which enables the exchange of control information between the OD and the FE electronics through a Clock and Control link.

The crystal readout data from the FE board is collected by the OD electronics DCC. In addition to the DCC is the TCC and a Clock and Control System card (CCS). The TCC finalizes the trigger primitives and transmit them to the regional Calorimeter Trigger system while the CCS is primarily task with distributing fast timing signals (LHC 40 MHz clock and trigger commands) to the FE and OD electronics and to synchronize their operation. A common clock distribution serving  $5 \times 5$  readout unit of the FE helps minimize channel-to-channel synchronization. Figure 4.1 shows a schematic view of the ECAL signal readout electronics.

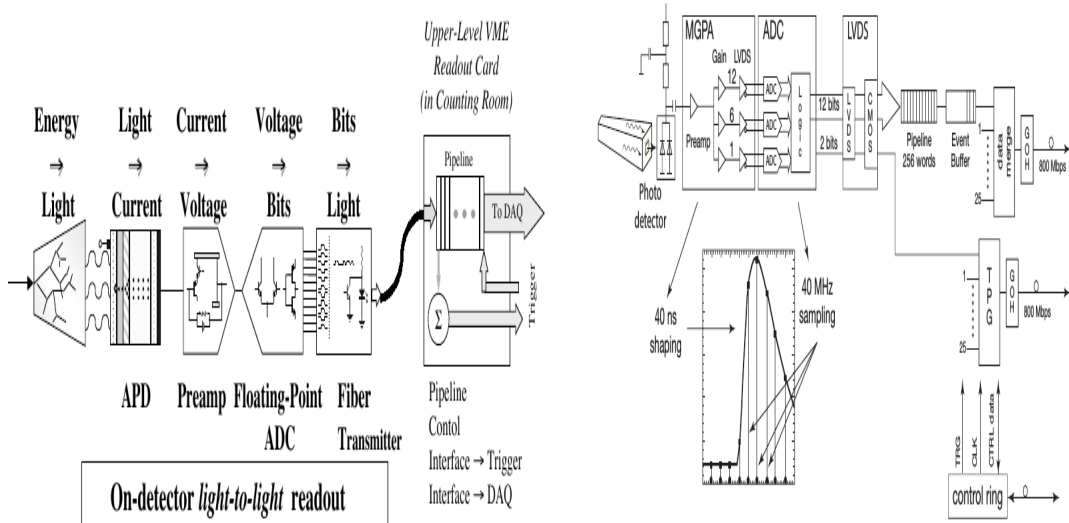


Figure 4.1: Schematic diagram of the CMS ECAL electronics readout.

## 4.2 Time Reconstruction

A typical analog pulse shape from a single channel is shown in Figure 4.2(a). Overlaying the pulse shape are the 10 digitized samples in red. The first three samples are attributed to the pedestal noise or ADC counts read in the absence of a signal. The maximum amplitude value of the pulse,  $A_{MAX}$ , and its corresponding time value,  $T_{MAX}$ , is used to reconstruct the time recorded by the channel.

We define time reconstruction as the measurement of  $T_{MAX}$  using the 10 digitized samples of the pulse amplitude. The time reconstruction procedure is implemented using an algorithm which starts by first finding the maximum amplitude of the pulse. Finding the true  $A_{MAX}$  using this representation of the pulse is not straight forward since the amplitude of each channel depends on  $A_{MAX}$ , the relative position of  $T_{MAX}$  between the time samples referred to as the “ $T_{MAX}$  phase” and the pulse shape itself. As a result, an alternative representation of the pulse shape using a ratio variable defined as  $R(T) = A(T)/A(T + 25 \text{ ns})$  is used, as  $R(T)$  is independent of  $A_{MAX}$ . The  $R(T)$  representation of the pulse shown in figure 4.2(b), can easily be described with a polynomial function.

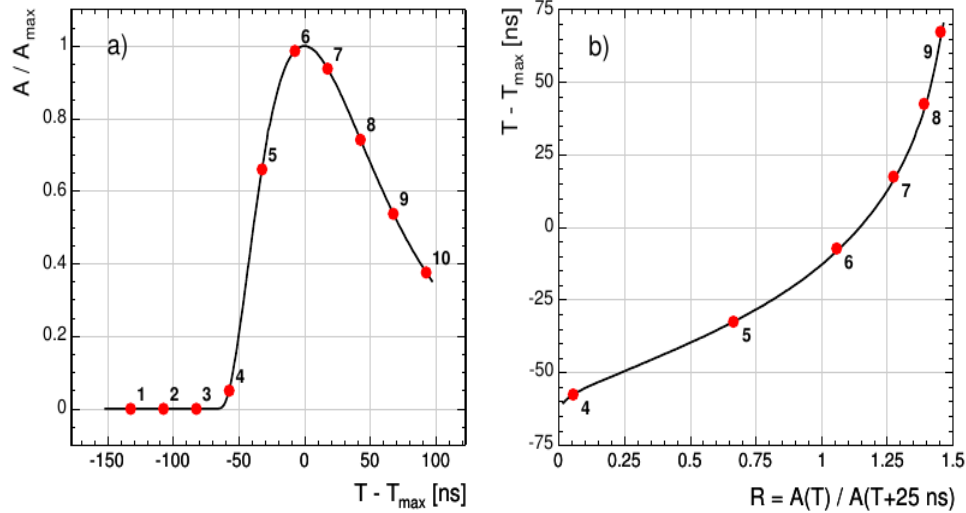


Figure 4.2: (a) A measured ECAL pulse shape for a single channel. (b)  $T - T_{MAX}$  Vs  $R(T)$  showing the distribution of  $T(R)$ . Solid line is pulse shape from test beam while dots are the 10 discrete samples corresponding to signal from proton-proton collision.

The distribution of  $T - \mathbf{T}_{\text{MAX}}$  as a function of  $R(T)$ , which we will refer to as  $T(R)$ , shows the 6 sample points (dots) obtained from the ratio  $R_i = A_i/A_{i+1}$ , of each consecutive pair of samples and the reference pulse shape (continuous line). Each  $R_i$  point gives a quick accurate measurement of  $T_{\text{MAX},i} = T_i - T(R_i)$ . The uncertainty,  $\sigma_i$ , on each measurement is a product of the derivative of the function  $T(R)$  and the uncertainty on the value of  $R_i$ . The uncertainty on the value of  $R_i$  depends on three separate uncertainties: the noise fluctuation,  $\sigma_n$  of each sample, the uncertainty in the estimation of the pedestal value which is always subtracted from the measured value and the truncation during 12-bit digitization. These uncertainties are uncorrelated and can be added in quadrature. The reconstructed time and uncertainty of a single channel or crystal is determined according to the expression given in Equation 4.2 after taking into consideration the different uncertainties,  $\sigma_i$  of each  $R_i$  point.

$$T_{\text{MAX}} = \frac{\sum \frac{T_{\text{MAX},i}}{\sigma_i^2}}{\sum \frac{1}{\sigma_i^2}} ; \quad \frac{1}{\sigma_T^2} = \sum \frac{1}{\sigma_i^2} \quad (4.2)$$

The sum is over all the 6  $R_i$  ratios and the assumption is that the weights are uncorrelated. The polynomial parameterization of the pulse shape and its parameters were obtained during electron test beam experiments by fitting to the pulse shape of the test beam data. These parameters obtained are subsequently used by the ECAL time algorithm to reconstruct time during proton-proton collisions.

## 4.3 ECAL Time Performance from Test Beam

### 4.3.1 ECAL Time Resolution

In order to quantify the performance of precise time measurement in ECAL, we study the total uncertainty or *time resolution*,  $\sigma(t)$ , in time measurement. The time resolution is expressed as a sum in quadrature (uncorrelated) of three major terms contributing to the uncertainty in time measurement. These three contributions are the noise, stochastic and constant terms. The *Noise (N)* term consists of the electronic noise, coherent movement of the baseline and effects arising in addition to the main or hard proton-proton collision, other soft or less energetic collision producing events called *pile*

*up* (PU) events. The *Stochastic* term ( $S$ ) is from fluctuations in the photon collection time because of the finite time during PbWO<sub>4</sub> scintillation. Lastly, the *Constant* term ( $C$ ) whose contribution is independent of the energy deposited but rather from effects correlated with the point of shower initiation within the crystal and systematics in the extraction of the time due to different pulse shape for each channel. The full expression for time resolution with all three contributions is given in equation 4.3,

$$\sigma^2(t) = \left( \frac{N}{A/\sigma_n} \right)^2 + \left( \frac{S}{\sqrt{A}} \right)^2 + C^2, \quad (4.3)$$

where  $A$  is the measured amplitude corresponding to the energy deposited and  $\sigma_n$  is the intrinsic noise for individual channel.  $\sigma_n$  has a value of 42 MeV and 140 MeV in the barrel and endcap, respectively.  $N = 33$  ns has been measured from Monte Carlo (MC) simulation studies. Contribution from the stochastic term, ( $S$ ) is considered small, with value of  $S < 7.9$  ns·MeV<sup>1/2</sup>.

To determine the intrinsic time resolution of ECAL and study the pulse shape, H2 and H4 test beam facilities at CERN were used. Prior to installation at the CMS detector, about 25% of the barrel and endcap crystals were exposed to electron beams with energy between 15 GeV and 250 GeV. The time resolution was obtained from the distribution of the difference in time of two crystals sharing energy and belonging to the same electromagnetic shower. The advantage of this approach is that, the contribution from poor crystal-to-crystal synchronization is minimized. If we neglect the stochastic term because its contribution to time resolution is negligible, equation 4.3 of the time resolution measured using the two crystals (in general, two superclusters can equally be used) reduces to equation 4.4. From now on, we will be using equation 4.4 to express the time resolution as it allows for a convenient comparison to results from test beam.

$$\sigma^2(t_1 - t_2) = \left( \frac{N}{A_{eff}/\sigma_n} \right)^2 + 2\bar{C}^2 \quad (4.4)$$

In equation 4.4,  $A_{eff} = A_1 A_2 / \sqrt{A_1^2 + A_2^2}$ , while  $t_{1,2}$  and  $A_{1,2}$  are the times and amplitudes of the two crystals.  $\bar{C}$  is their residual constant term contribution. The time resolution is measured from the standard deviation of a Gaussian fit to the time distribution from each slice of  $A_{eff}/\sigma_n$  of the  $A_{eff}/\sigma_n$  distribution. The resulting

distribution of  $\sigma(t_1 - t_2)$  of these standard deviations plotted against  $A_{eff}/\sigma_n$  is used to extract the noise and residual constant terms. The result presented in Figure 4.3 gives a noise factor  $N = (35.1 \pm 0.2)$  ns and  $\bar{C} = (20 \pm 4)$  ns obtained from test beam experiment.

The average time definition was not used as it is easily affected by synchronization effects. Other studies using the time difference between two basic clusters of separate electromagnetic shower was used and the results were similar

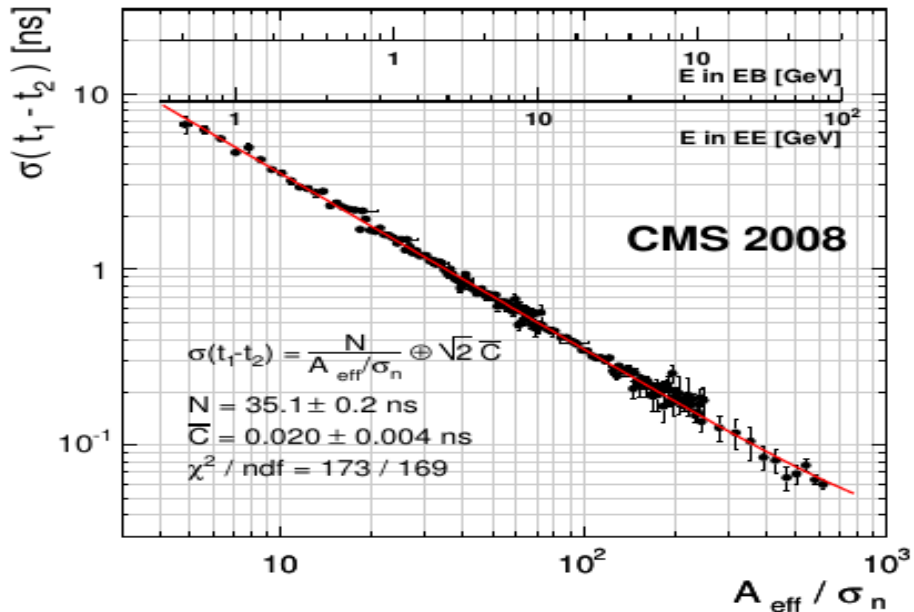


Figure 4.3: Deviation of the time difference as a function of  $A_{eff}/\sigma_n$  of two crystals sharing an energy and belonging to the same electromagnetic shower obtained during electron testbeam measurements. The single crystal energy scales for barrel (EB) and endcap (EE) is overlaid. The fitted results give  $N = (35.1 \pm 0.2)$  ns and  $\bar{C} = (20 \pm 4)$  ns.

A time resolution obtained from test beam experiment is better than 100 ps for energy  $A_{eff}/\sigma_n$  greater than 400 ADC counts. This demonstrates that for perfectly calibrated ECAL crystals and energy deposits of  $E > 20$  GeV in the barrel, a time resolution better than 100 ps can be realized during proton-proton collisions.

## 4.4 ECAL Time Performance from Collision

It is imperative to archive very precise time measurement with ECAL during proton-proton collision. As precise time measurement can be used to reject particles like cosmic rays, beam halo muons, electronic noise and out-of-time proton-proton interactions, with broad time distribution. Precise time can equally be used as a search variable for electromagnetic particles produced from the decay of trapped or long-lived particles. During proton-proton collisions, there are factors like crystal time variations over the entire LHC run, timing bias with energy, crystal-to-crystal synchronization and possibly loss in crystal transparency due to radiation, which can limit precise time measurements. Thus, a robust crystal time calibration procedure is required if we are to match the time resolution realized from test beam experiments.

### 4.4.1 Time Calibrations

Variations in crystal time maybe caused by the non-uniform response to electromagnetic showers by every crystal or time shifts introduced during machine interventions in technical shutdowns for repairs. These variations can be about 1 to 3 ns on average. To reduce these contributions, we continuously time align all 75,848  $\text{PbWO}_4$  crystals in ECAL by performing crystal *time calibration* once or twice every month. Time calibrating these crystals ensures that there is a uniform response by all the crystals to photons produced from proton-proton collisions, at interaction point, and traveling along a straight path with speeds close to the speed of light to the surface of ECAL. It equally guarantees the synchronization of all the component particles of an event and assigns each event to the correct LHC proton bunch crossing.

The presence of the “ $T_{MAX}$  Phase”, the difference in pulse shape between each crystal, variation in time of flight by a few nanosecond (ns) and the different intrinsic delays in each channel allow for time calibration at two separate levels. At the level of the front end electronics (FE) consisting of  $5 \times 5$  crystals, We perform an initial internal time synchronization by adjusting in steps of 1.04 ns among these block of crystals. Determining the values of adjustments to be made and immediately (online) performing this adjustments is done during *Hardware Synchronization*. Offline, we assign time constants to each crystal, during event reconstruction, such that the time of flight for

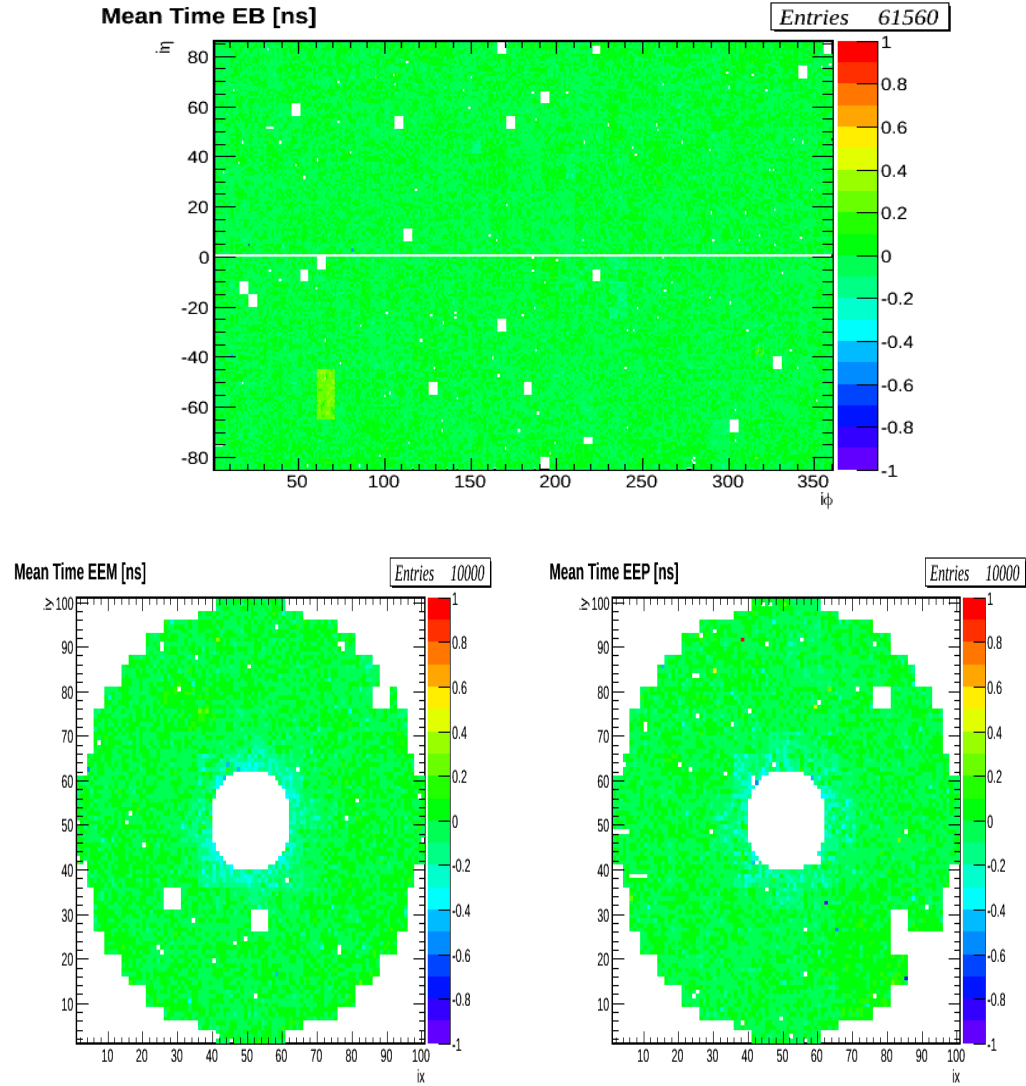
photons traveling along a straight path directly from the proton-proton interaction point to the crystals is the absolute measured time by all the crystals. The time adjustments constants are developed separately for the barrel and endcaps. There are significant benefits to having a uniform time alignment by all the crystals. With a better time calibrated detector, it is possible to distinguish between photons or electrons with significantly large arrival time from normal in-time photons produced in collisions. Large arrival time photons can be produced from the decay of slow moving particles;  $\beta \ll 1$ , or could be photons traveling along a path which significantly deviates from the obvious straight path from the proton interaction point, indicating the presence of a highly boosted particle or could be photons and electrons produced in the decay of a temporarily stopped particle inside the CMS detector.

### **Offline Time Calibration**

The purpose of the offline calibration is to provide time adjustments (calibration) constants for each channel (crystal) during event reconstruction. These constants are derived from data recorded during proton-proton collisions and are used to adjust for any global time shift in time measurements that might have occurred. The global phase shift of about 1 ns is caused by time shifts in the CMS clock relative to the LHC clock and time shifts of about 3 ns to 5 ns is caused by de-synchronizations introduced during hardware interventions. The calibration constants for each crystal is the reverse sign of the average time of all the reconstructed energy deposits (rechits) of the crystal. New sets of calibration constants are produced each month throughout the entire LHC run period. Each set of time constants produced has an *interval of validity* (IOV). A total of 17 IOV time constants were produced for the entire LHC run in 2011 and 44 IOV time constants for 2012.

In keeping with using mostly electromagnetic objects for producing the calibration time constants, datasets from proton-proton collisions containing mostly loosely triggered photon, electron and hadrons with large electromagnetic shower contribution events are used. These events are required to undergo a rigorous event selection process in order to minimize contamination from events not produced from proton-proton collisions like cosmic muons, beam halos and electronic noise. The produced constants are validated

using a closure test procedure and used during event reconstruction. The maps in Figure 4.4, show two dimensional distribution maps of the average time (time calibration constants) for each of the 61,200 crystals in EB and 14648 crystals in EE. The figure shows each crystal average time before (*top 3 plots*) and after (*bottom 3 plots*) calibration. More information about crystal time calibration for the entire LHC Run 1 is found in [36].



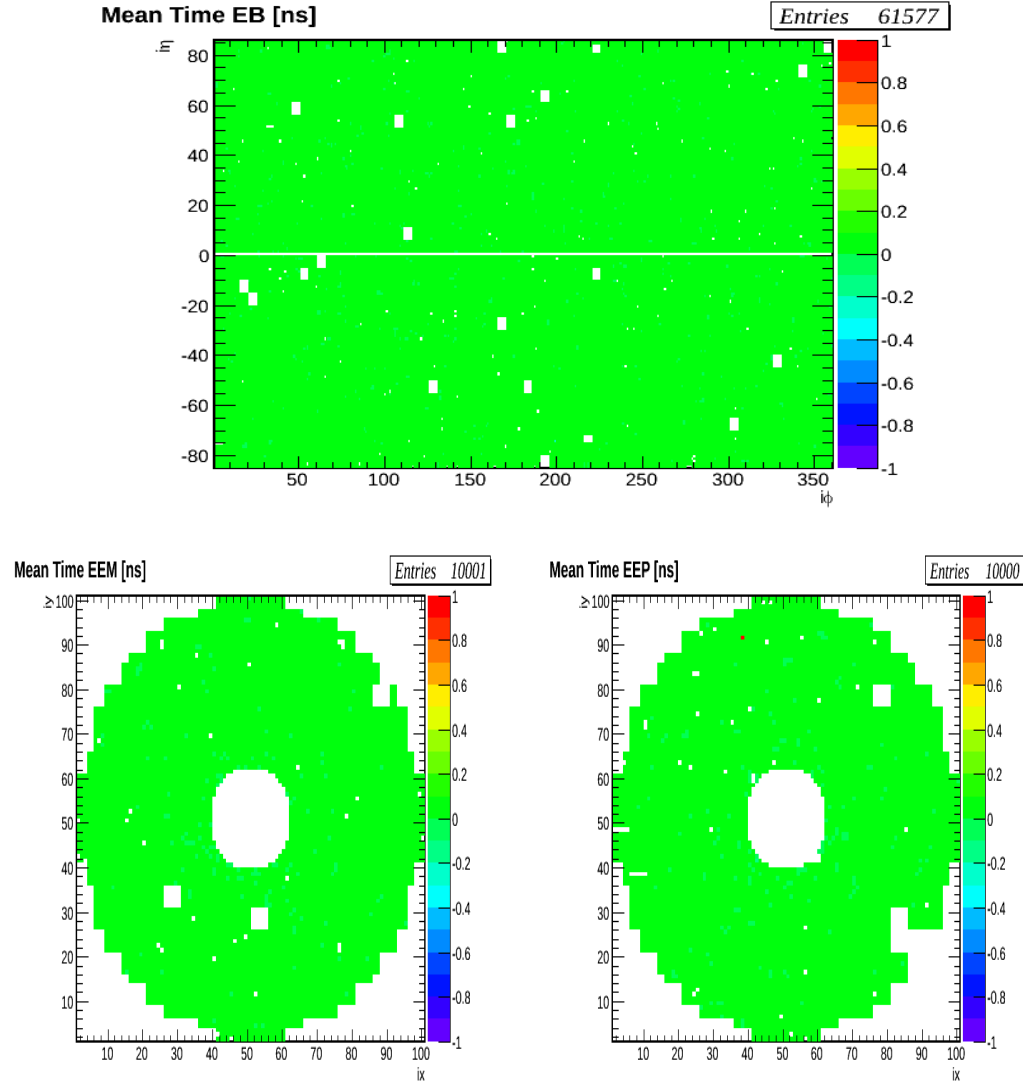


Figure 4.4: *Top 3*: Time calibration maps showing the distribution of mean time for each channel/PbWO<sub>4</sub> crystal in EB (top) and EE (below: EE-(left), EE+(right)) before calibration. *Bottom 3*: Time calibration maps showing the distribution of mean time after calibration. After calibration most crystals have an average time of zero(GREEN).

### Online Time Calibration

Time offsets are introduced during hardware interventions for ECAL front end electronics repairs. To minimize the impact of these time offsets and reduce additional rounds

of required event re-reconstruction, it is efficient and effective to adjust the time offsets or time latency directly online during CMS data recording. This adjustment can be performed using data from proton-proton collision or from laser.

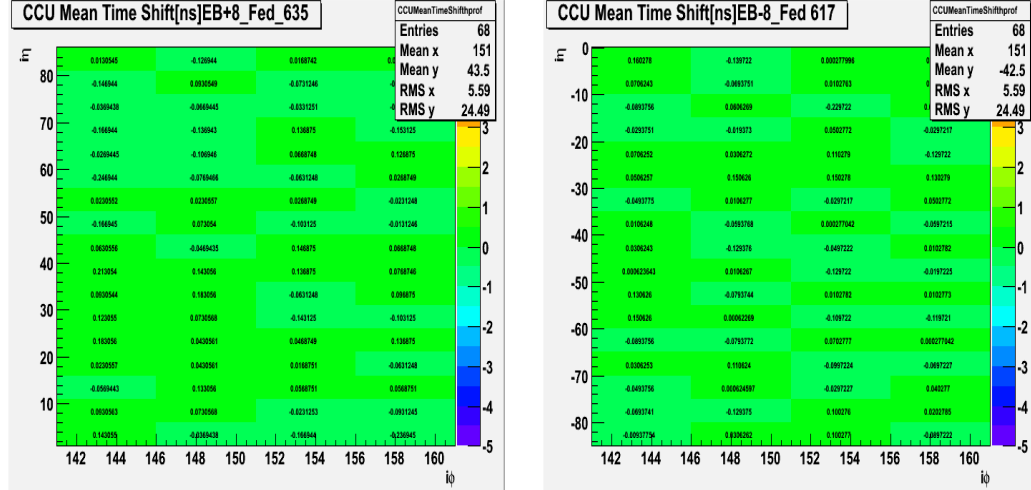
### Time Calibration With Collision

The approach for adjusting hardware time offsets immediately during data recording by CMS ECAL with stable proton-proton collision beams is to temporarily stop the entire data recording process, use the fraction of data recorded, and adjust the hardware time offsets. Data recording is resumed once the time offsets has been adjusted. The Data Quality Monitoring (DQM) and data certification services are used during this process. Stopping the CMS data recording process during LHC stable proton beams evidently leads to data lost which is one of the reasons for the large difference between the luminosity recorded by CMS detector compared to luminosity delivered by the LHC. As a result, although online or hardware time adjustment using collision data approach is efficient, however, the large CMS data recording downtime and lost of luminosity makes it unreliable especially during frequent machine interventions. To remedy the situation, a laser based time latency adjustment approach is encouraged.

### Time Calibration With Laser

The ECAL laser system comprise of two lasers, a 440 nm wavelength (close to peak emission for PbWO<sub>4</sub> crystals) laser for monitoring crystal transparency lose and a 796 nm wavelength laser for monitoring readout electronics chain from photodetectors to the electronics (i.e. APDs to ADCs). Both lasers have a jitter of less than 4 ns every 24 hours run and as a result, the time from the lasers is averaged over 600 event pulses. The time for each crystal from the laser is expected to be the same as the time from collision data and is represented as  $T_{\text{MAX}}^{\text{APD}}$ . The laser system is also equipped with a fast acquisition card called MATACQ. The time for each channel recorded using the Matacq is also averaged over 600 event pulse and denoted  $T_{\text{MATACQ}}$ . The difference,  $T_{\text{MAX}}^{\text{APD}} - T_{\text{MATACQ}}$ , of the two times, averaged over the 25 crystals of a Clock and Control Unit (CCU) is used as the time for each CCU,  $t_{\text{CCU}} = \langle T_{\text{MAX}}^{\text{APD}} - T_{\text{MATACQ}} \rangle$ . To obtain the time shift of 25 crystals belonging to the same Front End (FE) electronics, we

monitor for change of this time average before ( $t_{CCU}^B$ ) and after ( $t_{CCU}^A$ ) hardware intervention during detector maintenance. The time difference,  $\Delta t_{CCU} = t_{CCU}^A - t_{CCU}^B$ , after correcting for any global shift, and averaging over all the 25 crystals, i.e.  $\langle t_{CCU}^A - t_{CCU}^B \rangle$ , is the time shift, and the time calibration constant for the CCU is of opposite sign so that after correcting, the average time of the CCU is zero. This is done for all the 68 CCUs in a given supermodule (SM) or front end detector (FED). The global time shift of a given FED is caused by the laser light distribution in-homogeneity or evolution of the laser pulse due to different optical fiber supply of laser light to each CCU. Each FED has 1,700 PbWO<sub>4</sub> crystals and we produced laser based time calibration constant for all its crystals. The plots in Figure 4.5 show the current observation status after monitoring for time shift within each CCU using laser. It shows the distribution of the CCU time difference before and after machine intervention,  $\Delta t_{CCU}$ , with the Root Mean Squared (RMS) error for each CCU. We have subtracted the global time shift per FED to reduce the possibility of a false alarm of a time shift in a given CCU. Using laser data, we are able to measure the time shift of each CCU to within 0.2 (0.5) ns EB (EE) in precision. Compared to calibration using collision data, there are no downtime as we can adjust for any hardware time shift prior to stable proton beams. The full procedure including technical details for performing hardware latency adjustments online using collision data or laser data is well described in [37].



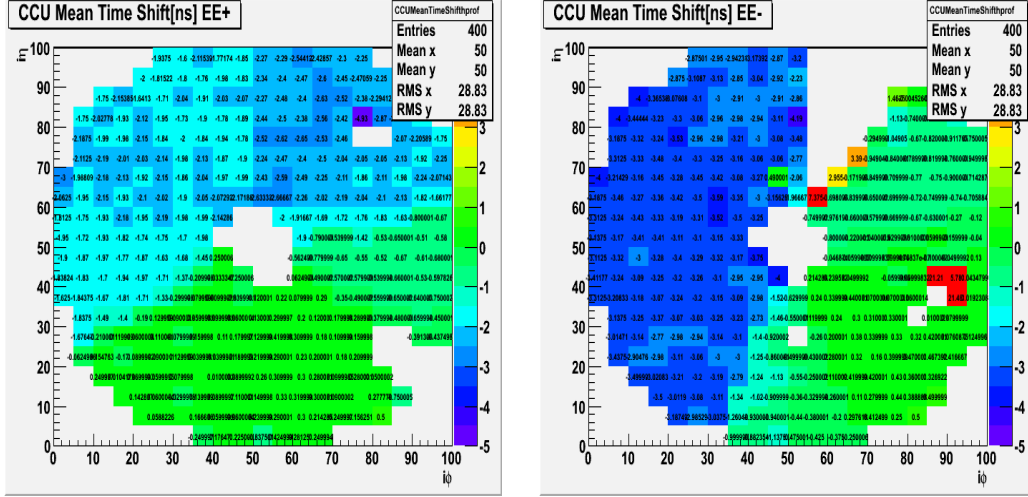


Figure 4.5: *Top:* The mean time distribution obtained from laser of crystals in a single FED i.e. EB $\pm$ 8. *Bottom:* Clock and Control Unit (CCU) mean time shift distribution of FEDs EE+ and EE-.  $\Delta t_{CCU}$  distributions after the global shift has been removed. The adjustment for global time shift per FED due to difference in light source for each CCU has been shown to reduce the possibility of CCU showing false time shift.

#### 4.4.2 Time Bias

An additional source contributing to poor time measurement arise from energy related time bias. This bias originates from the time reconstruction algorithm. It is expected that the ratio approach for time reconstruction performs efficiently for all ADC counts. However, during data recording in LHC Run 1, it was observed that for high ADC counts produced by very energetic particles, an inherent bias in the time is introduced by the multi-gain pre-amplifier electronics for electromagnetic particles with energy above certain gain transition points. The full conversion of the energy of a particle recorded by a crystal in ADC counts to GeV is expressed as;  $E_i = G \cdot S_i(t) \cdot C_i \cdot A_i$ , where  $A$  is the amplitude from the pulse shape in ADC counts,  $G$  is the ADC-to-GeV conversion factor equal to 0.039(0.063) in EB(EE),  $C_i$  is the inter-calibration coefficients accounting for individual channel response to the electromagnetic shower and  $S_i(t)$  is the correction term obtained from laser accounting for radiation-induced channel response.  $S_i$  changes over time. The first gain transition point (Gain-1) of the multi-gain pre-amplifier occurs at 4096 ADC counts corresponding to 159.744 GeV in EB and 258.048 GeV in EE. The subsequent Gain 6 and 12 transitions occur at energy values of TeV.

At these gain transition points, the ratio algorithm introduces a time bias in the time reconstruction. We correct the time bias in an energy dependent manner during event reconstruction. The corrections are made on a CMS event reconstruction software (CMSSW) release basis. Figure 4.6 shows the comparison between two CMS event reconstruction software releases, CMSSW44X, where these time bias corrections have not been made and CMSSW53X, where the the corrections have been made. Evidently, the average time displayed in both CMSS44X and CMSS53X show the disappearance of the time bias for all particle energy in CMSSW53X after the time bias corrections were made.

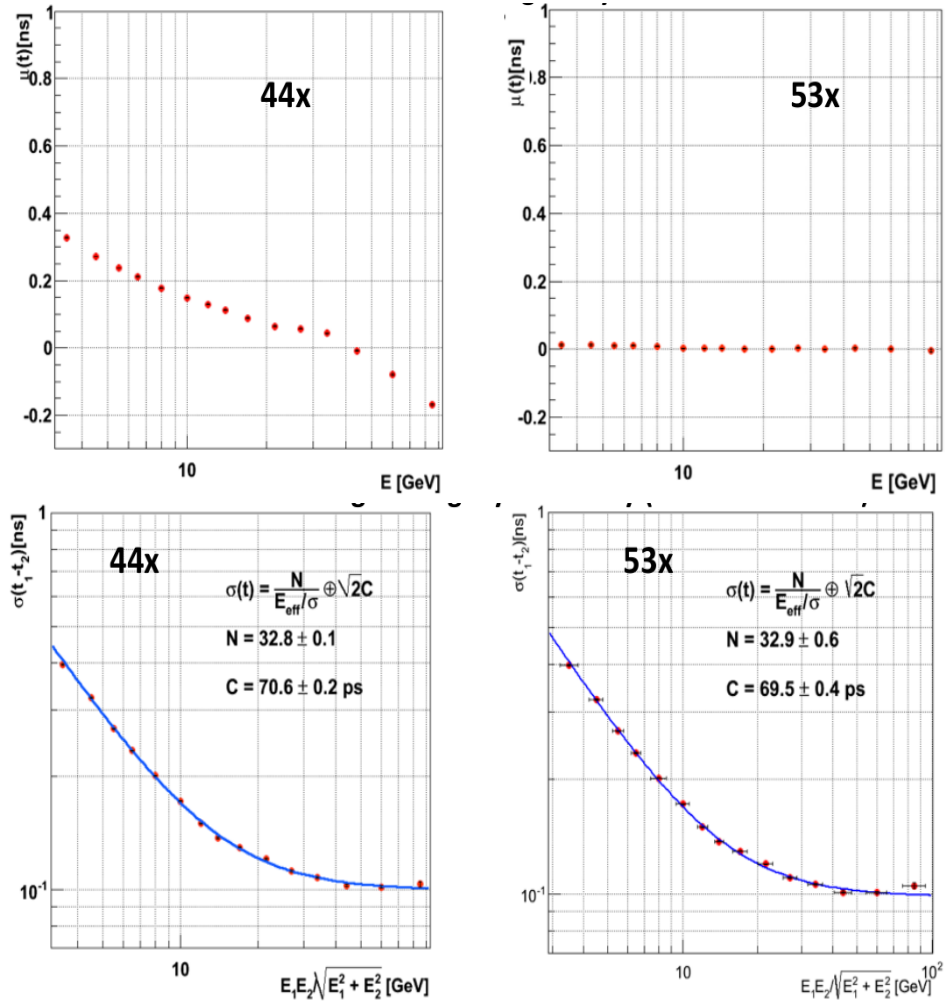


Figure 4.6: Distribution of mean time ( $\mu$ , top row) and time deviation ( $\sigma$ , bottom row) as a function of crystal energy for EB prior (left) and after (right) time bias corrections depending on energy have been applied.

To investigate further for any additional time bias un related to the particle energy, we study how the crystal geometric position in ECAL covering from  $\eta = 0$  to  $\eta = 3.142$ . The results shown in Figure 4.7 show no crystal position or  $\eta$  dependence. However, time bias of the order of 100 ps have been observed. There are efforts to understand the source of these time bias with speculations that the time bias might be caused by electronics or loss in PbWO<sub>4</sub> crystal transparency due to radiation.

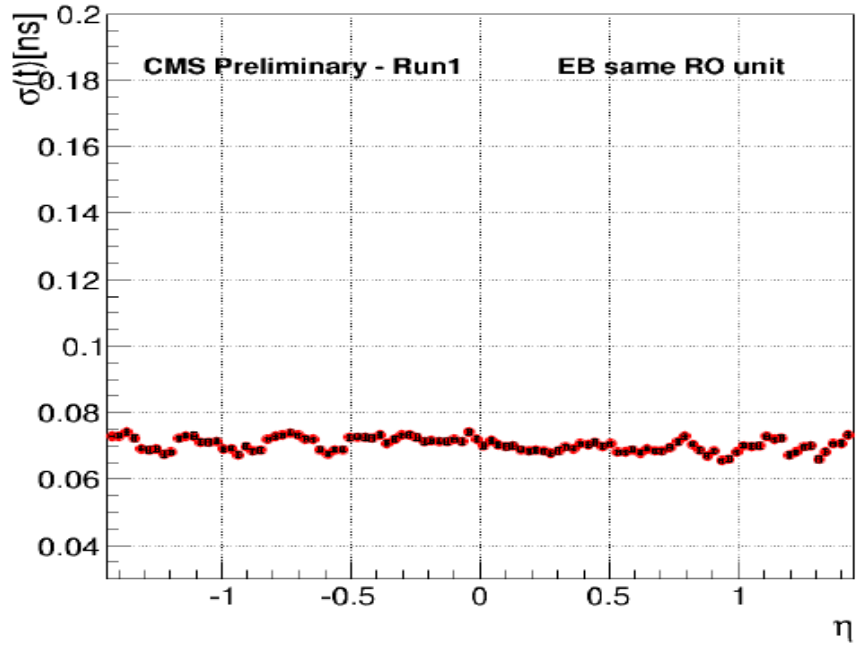


Figure 4.7: Distribution of the time standard deviation ( $\sigma$ ) against crystal geometrical position,  $\eta$ , in the ECAL barrel. Almost flat distribution of  $\sigma$  with  $\eta$ .

#### 4.4.3 ECAL Time Performance With Z Events

We evaluate the precision of ECAL time measurements during proton-proton collisions by studying the time measurement of a well understood physics process; the decay of the Z boson to an electron pair, i.e.  $Z \rightarrow e^-e^+$ . We use the standard deviation (time resolution),  $\sigma_{eff}$ , of the difference in arrival time of the two electrons to evaluate ECAL

time performance. The standard deviation is obtained from the difference in the seed time,  $t_{seed}$ , of the electron electromagnetic shower of each electron after correcting for contributions from the bending of the electron travel path inside CMS magnetic field of 3.8 T. In Figure 4.8, we present the distribution of the time difference,  $t_{electron1} - t_{electron2} = t_{seed1} - t_{seed2}$ , of both electrons adjusted for time of flight corrections and in Figure 4.9, we show the time resolution or  $\sigma_{eff}(t_1 - t_2)$ , obtained from the time distribution of the seed crystal time without correcting for the bending of the electron's flight path contributions. A time resolution of 232 ps in EB and 384 ps in EE is realized. However, if we remove the contributions from the spread in time,  $\sigma(t_{collision})$ , due to the finite time it takes for the two proton bunches of length 5.5 cm to collide; which is about  $\sigma(t_{collision}) = \sigma(t_Z) = 183$  ps, we obtain an improved time resolution of 142 ps in EB and 337 ps in EE. The selection for Z candidate events required that the electrons have a transverse energy bigger than 10 GeV and the reconstructed Z mass is within,  $60\text{ GeV} < m_{inv}(e_1, e_2) < 150\text{ GeV}$  in order to ensure mostly good Z boson candidate events are used.

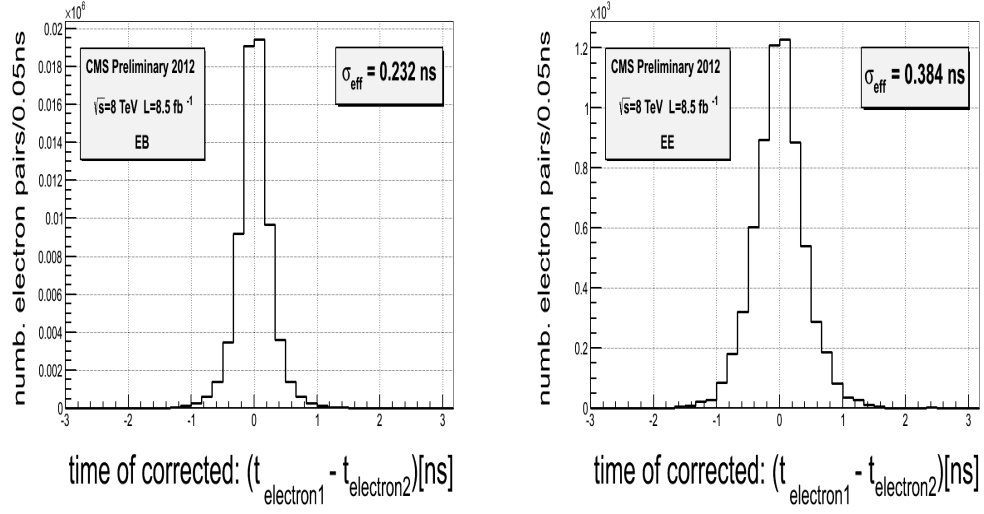


Figure 4.8: Ecal time difference between the two reconstructed electrons in  $Z \rightarrow e^-e^+$  decay. The electron time is the seed (crystal with highest energy deposit) time with additional correction due to the time of flight of the electron in EB and EE

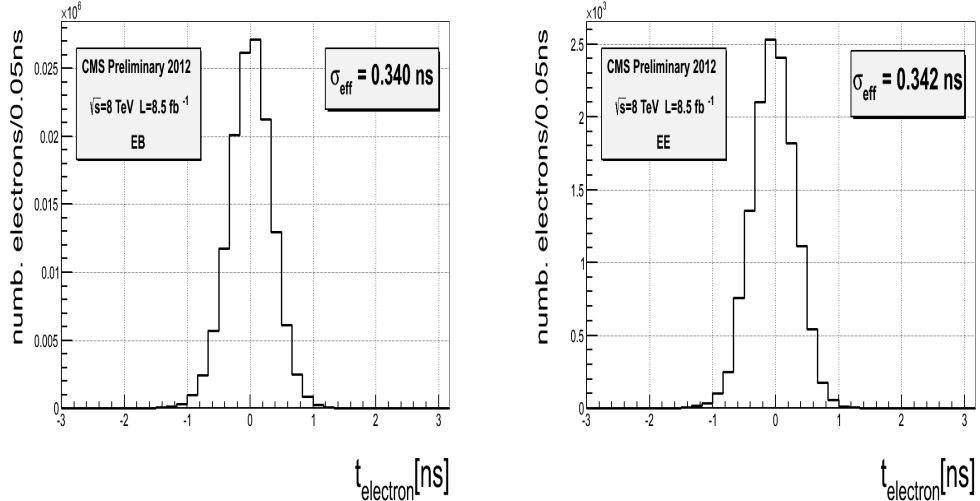


Figure 4.9: Ecal absolute time of a single reconstructed electron in  $Z \rightarrow e^-e^+$  decay. The electron time is the seed (crystal with highest energy deposit)time of the electron in EB and EE

We also investigate the contributions attributed to the readout electronics on the time resolution using events with  $Z \rightarrow e^-e^+$  decay. Figure 4.10(left), shows the time resolution obtained from measuring the electrons arrival time in the case where the seed crystal time of both electrons is read from the crystals belonging to same ReadOut (RO) electronics and compared to the other case where the seed crystal time is read from crystals belonging to two different readout electronics shown in Figure 4.10(right). The Constant term,  $C$ , for the same RO electronics is about 67 ps while that for different RO electronics is 130 ps indicating that electronic readout de-synchronization contributes to the worsening of the time resolution.

Despite, the observed 100 ps bias which seems to be related to readout electronics, we argue that, with a time resolution of  $\sigma(t) \leq 400$  ps, the ECAL subdetector is very reliable for time measurements and can be used in the search for delayed electromagnetic particles produced in the decay of long-lived particles.

The ECAL time resolution for the entire LHC Run 1 of 2011 and 2012, comparing the absolute and single precision time measurements is summarized in table 4.1.

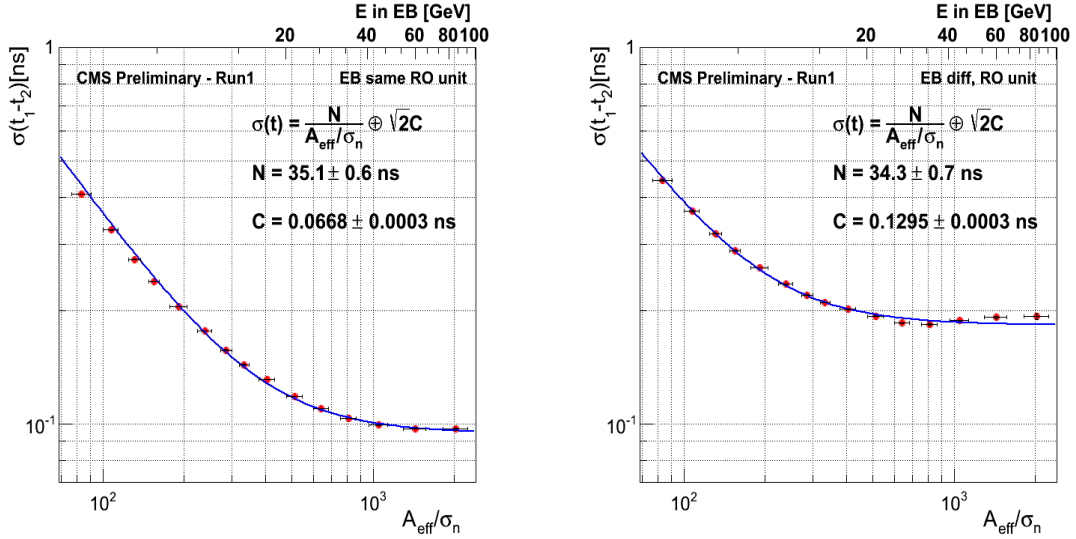


Figure 4.10: Timing resolution from: *left*: Two most energetic crystals in the same readout unit, *right*: Two most energetic crystals belonging to different readout units, as a function of effective amplitude( $A_{\text{eff}} = A_1 A_2 / \sqrt{A_1^2 + A_2^2}$ ) normalized to noise in EB. Both crystals are from reconstructed electrons in  $Z \rightarrow e^- e^+$  events.

### ECAL Timing Resolution

2011	
	Absolute Time
	$\sigma_{\text{eff}}(t_{\text{seed}})[\text{ps}]$
<b>EB</b>	376
<b>EE</b>	356
2012	
	Absolute Time
	$\sigma_{\text{eff}}(t_{\text{seed}})[\text{ps}]$
<b>EB</b>	340
<b>EE</b>	342
Single Precision	
	$\sigma_{\text{eff}}(t_{e1} - t_{e2})/\sqrt{2}[\text{ps}]$
<b>EB</b>	190
<b>EE</b>	282
<b>EB</b>	164
<b>EE</b>	272

Table 4.1: ECAL timing resolution absolute time and single precision for 2011 and 2012 of LHC Run 1

# Chapter 5

## Event Reconstruction

### 5.1 Event Reconstruction Overview

An event is comprise of one or more particles produced in a particular proton-proton collision. Event reconstruction is the process of constructing particles and their four momenta using raw data read from the electronics of the different CMS subdetectors. The process begins in each subdetector using a local reconstruction algorithm and eventually extends to all subdetectors. In the calorimeter subdetectors, an energy clustering algorithm is used to produced energy clusters and in the tracker and muon chambers, a combination of tracking algorithms is used to construct particle tracks. By matching selected tracks to energy clusters, particles like photons, electrons, muons, jets and missing transverse energy ( $E_T^{\text{miss}}$ ) are reconstructed.

### 5.2 Supercluster Reconstruction

The clustering algorithm produces a cluster of clusters called *supercluster*, of the energy of an electromagnetic shower. A supercluster is either a  $3 \times 3$  or  $5 \times 5$  crystal energy matrix. About 94% (97%) of the incident photon or electron energy is deposited in this  $3 \times 3$  ( $5 \times 5$ ) matrix of crystals in the  $(\eta, \phi)$  plane in barrel or  $(x, y)$  plane in endcap. The 3.8 T magnetic field and material in front of the calorimeter causes bremsstrahlung electrons and converted photons to deposit their energy in a cluster of crystals spread in  $\phi$ . As a result, clustering algorithms start building superclusters with

a seed crystal(crystal with the maximum energy), continue within a narrow window in  $\eta$  by summing the crystal energies along the  $\phi$  which is the direction of energy spread due to the magnetic field. Figure 5.1 is schematic picture showing the direction of the clustering process in the  $(\eta, \phi)$  plane in barrel and the fraction of electromagnetic energy coverage in a typical supercluster.

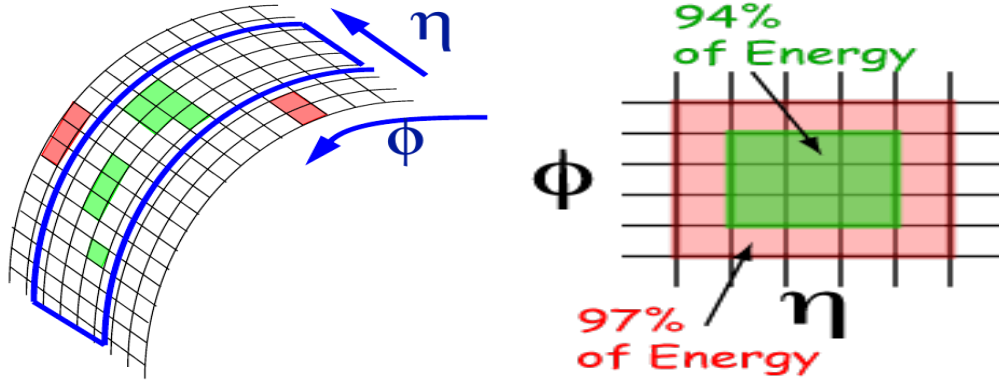


Figure 5.1: Superclustering algorithm direction in the  $(\eta, \phi)$  plane in EB and fraction of electromagnetic shower energy coverage in a crystal energy matrix.

The two major clustering algorithms used in ECAL are the *hybrid* (EB) and *island* (EE) algorithms.

- **Hybrid Supercluster Algorithm:** This algorithm is used for making super clusters in the barrel (EB). It takes advantage of the  $\eta - \phi$  geometry of barrel crystals by taking a fixed 3 or 5 crystals in  $\eta$  and dynamically search and sum separate crystals energy along  $\phi$ . The Hybrid algorithm takes advantage of our knowledge of the lateral shower shape along the  $\eta$  direction. The supercluster consists of basic clusters, usually  $3 \times 3$  crystals matrix.
- **Island Supercluster Algorithm:** This algorithm is used for making clusters in the endcap (EE). It begins by finding the seed crystal of the electromagnetic shower with maximum energy above a certain energy threshold. Using the seed crystal position, adjacent crystals are examined and added to a cluster until a rise in energy where a crystal belonging to another cluster or crystal that has no readout is reached. For each crystal to be added to the cluster, its energy read must be positive, it must not have been assigned to another cluster and the

previous crystal added in the same direction must have a higher energy. These non-overlapping clusters finally forms a “supercluster”.

### 5.3 Track and Vertex Reconstruction

Charge particle track reconstruction in CMS uses many algorithms. All these algorithms use the reconstruction positions (*hits*) during the passage of a charged particle in the silicon detectors, to determine the helix trajectories of charged tracks. These helix trajectory is used to measure the particle’s momentum and direction.

The main algorithm used for track reconstruction of proton-proton collisions is the Combinatorial Track Finder (CTF). The CTF proceeds in three stages: seeding, finding and fitting. During seeding, hits that are compatible with the interaction region above a lower  $p_T$  limit are used as possible candidates of the charge tracks. Pixel hits are the best track seeds. In the more forward region of the tracker detector,  $2 < |\eta| < 2.5$ , pixel and inner strips are used for better track finding. The track finding stage uses the Kalman Filter pattern recognition approach where, starting with the seeded parameters, the track trajectory is extrapolated to neighboring tracker layers and compatible hits are assigned to the track. During the fitting stage, the Kalman Filter algorithm is again applied where each candidate track is fitted using least-squares fitting in two stages. The first stage removes possible bias from the seeding stage while the next stage yields the best estimates of the track parameters at the original vertex. Other algorithms like the *iterative tracking algorithm* which is a general purpose tracking algorithms is used in association with customized CTF tracking algorithm to reconstruct the tracks of non-collisions events like cosmics and beam halo.

Similar to track reconstruction, vertex reconstruction involves two stages of vertex finding and fitting. During vertex finding, many tracks are grouped together into vertex candidates. The vertex finding algorithms used depends on whether it is finding primary or secondary vertex or the reconstruction of an exclusive particle decay. In vertex fitting, the best estimates of the vertex parameter like position, covariance matrix and track parameter constraint as well as the fit quality (chi-square, number of degrees of freedom, track weights) is used to distinguish among a given sets of tracks.

## 5.4 Photon and Electron Reconstruction

Photons are reconstructed from superclusters using the energy contained in a  $5 \times 5$  crystals matrix surrounding the seed crystal. Since photons are neutral, photons are identified as superclusters in ECAL not associated to any tracks or reconstructed positions in the pixel tracker. To improve photon identification, several criteria are used to distinguish true photons from other particles misidentified as photons. The criteria to identify true photons consists of tracker isolation, ECAL isolation, hadron calorimeter isolation, hadronic to electromagnetic ratio and  $R_9$ , which is the ratio of the electromagnetic energy contained in a  $3 \times 3$  matrix to the supercluster energy. The  $R_9$  variable is very useful in separating photons from the decay of  $\pi^0$  with isolated photons since the photons from  $\pi^0$  decay have a lower value of  $R_9$  compared to isolated photons.

Similar to photons, electron candidates are found when a supercluster is associated to a track reconstructed in the silicon tracker detector and in particular, its inner most layers. In electron reconstruction, the seeding approach is either driven by ECAL or by the tracker. The ECAL driven seeding approach is very efficient for electrons with  $p_T > 10 \text{ GeV}/c$ . The track driven seeding approach uses a boosted decision tree to perform a pre-selection of the tracker clusters, in order to reduced fake electrons which are light hadrons. Isolated electrons with low  $p_T$  and non-isolated electrons (electrons embedded in jets) are reconstructed efficiently using the tracker driven seeded approach. When fitting the electron tracks, we must account for the different energy loss mechanisms of the electron compared to other charged particles. Since electrons energy loss is mainly through the non gaussian nature of its bremsstrahlung, the Gaussian Sum Filter algorithm is used to provide a good estimated the track momentum both at the ECAL surface and at the interaction point.

During proton-proton collisions, in addition to events with true photons and electrons, are events produced from low energy proton-proton collisions called *minimum biased events*, events produced from the radiation of the quarks and gluons called *underlying events*, and events from multiple proton-proton interactions called *Pile Up* (PU) events, contributing to the reconstructed photon or electron energy. Additional contributions to this energy comes from poor detector calibration, poor supercluster or track

reconstruction, faulty electronics and crystal transparency loss due to radiation. The true photon or electron energy must be adjusted for these contributions during reconstruction.

An estimate of the energy deposited by an electromagnetic particle in the ECAL,  $E_{e/\gamma}$ , can be approximated using Equation 5.1;

$$E_{e/\gamma} = F_{e/\gamma} \cdot [G \cdot \sum_i S_i(t) \cdot C_i \cdot A_i], \quad (5.1)$$

where  $A_i$  is the signal amplitude in ADC counts,  $C_i$  is the inter-calibration coefficient,  $S_i(t)$  is the time-dependent corrections for response variable, usually obtain from laser,  $G$  is the global scale calibration allowing to go from energy in ADC counts to GeV and  $F_{e/\gamma}$  is the particle energy corrections for geometric, clustering and other effects. The sum is over all the crystals belonging to the photon or electron supercluster. To obtain the true electron or photon energy, energy adjustments which depend on  $\eta$  through  $F_{e/\gamma}$  are applied during supercluster reconstruction to account for detector energy mis-measurements caused by cracks between crystals and electronic noise. In Figure 5.2, we show comparisons between cases where no energy adjustments were made to those where energy adjustments (in the form of crystal inter-calibration and laser monitoring corrections for crystal transparency loss) have been made, through measuring the mass of the Z boson. We see improvements on measuring the Z mass, 91 GeV/cc, after the inter-calibration (IC) and laser monitoring (LM) corrections were made. Figure 5.3, shows the case where adjustments are made during supercluster reconstruction. Once again the Z mass is well reconstructed after introducing these corrections.

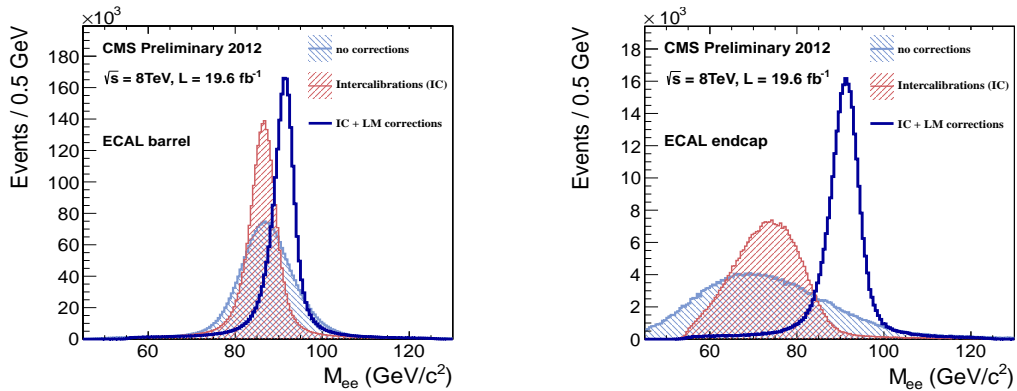


Figure 5.2: Z mass distribution from  $Z \rightarrow e^+e^-$  decay showing improvement in the measurement of the Z mass after performing energy adjustments to account for intrinsic spread in crystal, photo-detector response and time-dependent corrections to compensate for channel response loss for EB (right) and EE (left)

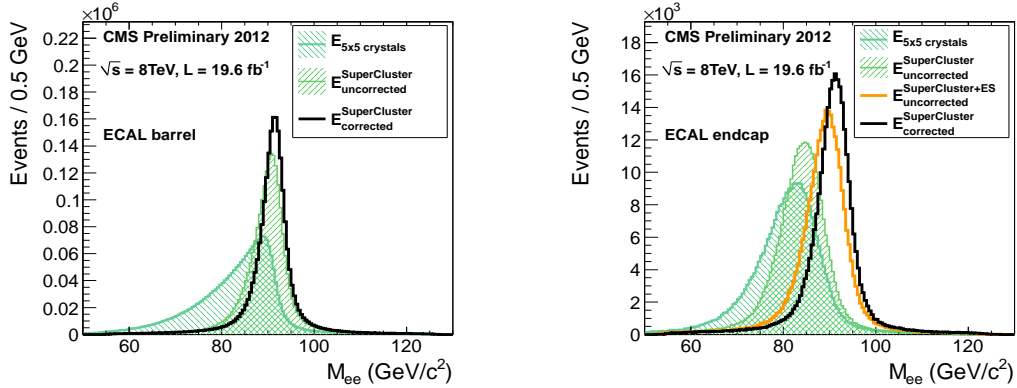


Figure 5.3: Z mass reconstructed using electron superclusters shows improvement in Z mass measurement after applying energy adjustment at superclusters for EB (right) and EE (left).

In Table 5.1, we present a summary of variables constructed using information of the spread of the electromagnetic shower in  $\eta$  and  $\phi$ , the ratio of the energy deposited in HCAL to ECAL, the track  $p_T$  and ECAL  $E_T$ , isolation in ECAL, HCAL and tracker, the ratio of the energy sums over  $3 \times 3$  and  $5 \times 5$  matrices centered on the highest energy crystal of the seed cluster;  $R_9 = E_{3 \times 3}/E_{5 \times 5}$  or  $R_9 = \sum E_9 / \sum E_{Supercluster}$  and impact parameter,  $d0$ , which is the minimum separation of the electron track computed with respect to the reconstruction vertex and track transverse momentum,  $p_T$ . Photon and electron selection using these variables, applied during electron and photon identification, have been shown to produce very good quality electron and photon candidates with efficiency above 70%.

### Simple Cut Based Electron Photon Identification

ID Variable	Electron	Photon
$H/E$	0.05(EB), 0.10(EE)	0.05
$ \Delta\eta_{in} $	0.005(EB), 0.007(EE)	0.015(EB)
$ \Delta\phi_{in} $	0.09(EB), 0.09(EE)	N/A
$\sigma_{i\eta i\eta}$	0.01(EB), 0.03(EE)	0.011(EB), 0.03(EE)
Pixel Veto	No	Yes
$ d0 (vertex)$	0.02(EB), 0.02(EE)	Veto
$ dZ (vertex)$	0.1(EB), 0.1(EE)	0.02 (cm)(Veto)
$ 1/E - 1/p $	0.05(EB), 0.05(EE)	N/A
PF isolation / $p_T$ (cone dR=0.3)	0.15(EB), 0.10(EE)	N/A
ECAL Isolation	same	$4.2 + 0.006 * E_T^\gamma +$ $0.183 * \rho(\text{EB})$
HCAL Isolation	same	$2.2 + 0.0025 * E_T^\gamma +$ $0.062 * \rho$
TRACK Isolation	same	$2.0 + 0.001 * E_T^\gamma +$ $0.0167 * \rho$
Rho corrected PF photon isolation	N/A	$1.3 + 0.005 * p_T^\gamma(\text{EB})$

Table 5.1: Simple cut-based selection criteria for electron and photon identification.

## 5.5 Muon Reconstruction

Muon tracks are reconstructed using the all-silicon inner tracker (tracker tracks) and the muon system (standalone tracks). The standalone tracks are reconstructed using reconstructed positions (hits) in the muon system consisting of the Drift Tubes (DT) in the barrel ( $|\eta| < 0.9$ ), Cathode Strip Chambers (CSC) in the endcaps ( $1.2 < |\eta| < 2.4$ ) and Resistive Plate Chambers (RPC) in the overlap region ( $0.9 < |\eta| < 1.2$ ). There are two independent muon reconstruction approaches: *Global muon reconstruction (Outside-in)* and *Tracker muon reconstruction (Inside-out)*. For Global muon reconstruction, each standalone-muon track is matched to a tracker track by comparing the parameters of

the two tracks propagated to a common surface. The global muon track is fitted combining hits from the tracker track and standalone-muon track using the Kalman-filter algorithm. For the tracker muon reconstruction, all tracks with  $p_T > 0.5 \text{ GeV}/c$  and total momentum  $p > 2.5 \text{ GeV}/c$  are considered as possible muon candidates and are extrapolated to the muon system taking into consideration the magnetic fields, the average expected energy loss in the calorimeters and multiple Coulomb scattering in the detector material to locally reconstruct segments in the muon system. A combination of different muon algorithms depending on the muon  $p_T$ , provides a robust and efficient muon identification.

Using the beam spot as constraint of the muon's vertex, it is possible to distinguish between muons produced from proton-proton collisions from those produced from cosmic *cosmic muons* and proton beams interacting with the gas in beam pipe and proton dump muon splash events produced 150 m upstream the CMS detector during proton beam dump. The proton beam related muons are referred to as *beam Halo muons*. Figure 5.4 show an illustration of trajectories of different muon sources interacting with the CMS detector.

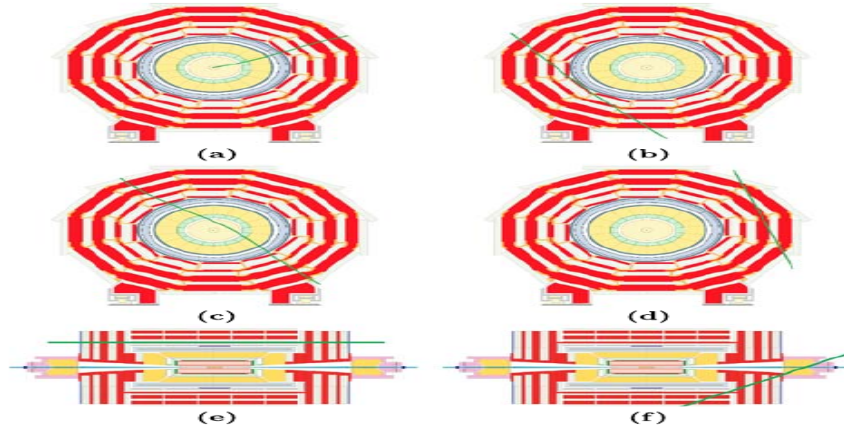


Figure 5.4: Illustration of muons from proton-proton collision, cosmic rays and beam halo. (a) Muons from collision propagating from the center and moving outwards, (b) Cosmic muons traveling through the detector leaving signals in opposite hemispheres of the muon system, (c) Cosmic muons leaving signals in the tracker and opposite hemispheres, (d) cosmic muons entering and leaving the detector without passing through the muon detector layers, (e) beam halo muons penetrating the detector and leaving signals in the endcaps and (f) Cosmic muons entering the detector through the endcap and leaving through the barrel and which can happen in a *vice-versa* manner.

### Particle Flow Algorithm

The *Particle Flow* (PF) algorithm is an algorithm for reconstructing particles combining information from the tracker, ECAL, HCAL and muon chambers of the CMS detector. It uses a combination of different algorithms comprising of calorimeter clustering, tracking and extrapolation to calorimeters, muon identification, electron pre-identification and linking of topological elements, for reconstructing a list of particles which include photons, charge hadrons, neutral hadrons, muons and electrons. The same list of particles is subsequently used to reconstruct composite “particles” like jets,  $E_T^{\text{miss}}$  and taus. The versatility of the PF algorithm is the reason why it was introduced for reconstructing Jets, missing transverse energy ( $E_T^{\text{miss}}$ ) where complete information of the event content from every subdetector is needed. The PF algorithm uses tracks, electron energy seeds, 4-momentum, super cluster energy calibration, bremsstrahlung tracks for electron and photon reconstruction making it extremely efficient at minimizing electron and photon misidentification. For  $E_T^{\text{miss}}$  reconstruction where full reconstruction of all the particles belonging to an event is necessary, the PF algorithm is very reliable.

## 5.6 Jet Reconstruction

A jet is a spray of particles arising from the hadronization of colored particles. Because jets are made of many particles like electrons, photons, hadrons, charged and neutral electromagnetic and hadronic showers, they are best reconstructed using the particle flow algorithm. Jets reconstructed using the PF algorithm are called *Particle Flow Jets*. Using calorimeter towers as input, jets can also be reconstructed using the Anti- $k_T$  clustering algorithm which combines four vectors according to their relative transverse momentum within a standard cone size of  $R = 0.5$  in the  $(\eta, \phi)$  plane. The quality of a reconstructed jet depends on the jet identification selection criteria known as the *JetID*. High quality jets are required to have an electromagnetic energy fraction (EMF)  $> 0.01$ , within the ECAL fiducial region of  $|\eta| < 2.6$ , the number of calorimeter cells containing more than 90% of jet energy ( $N_{jet}^{90}$ ) must be  $> 1$ , the fraction of jet energy in the hottest Hybrid photodetector (HPD) unit in HCAL readout within a jet ( $f_{HPD}$ ) must be  $> 0.98$ , the charge hadron fraction ( $CHF$ )  $> 0.0$  if within  $|\eta| < 2.4$ , the neutral hadron fraction ( $NHF$ )  $< 1.0$ , the charge electromagnetic fraction ( $CEF$ )  $< 1.0$ , and

neutral electromagnetic fraction  $z(NEF) < 1.0$ . These jetId selection requirements have been shown to remove mis-reconstructed jets arising from spurious energy deposition in subdetectors with good efficiency. The jet energy is often mis-measured due to cracks in the detector, non-linear responses in the calorimeters, electronic noise, poor detector calibration and additional energy from PU. Therefore, adjusting the jet energy through *jet energy corrections* (JEC) is often performed guaranteeing a reliable measurement of the jet energy during reconstruction.

## 5.7 Missing Transverse Energy Reconstruction

It is very challenging to detect particles which do not interact with the detector. Such particles include very weakly interacting particles like neutrinos ( $\nu$ ), neutralinos ( $\tilde{\chi}_1^0$ ) and gravitino ( $\tilde{G}$ ). In CMS, the presence of this kind of particles in an event is inferred through a measurable quantity called *missing transverse energy*. Measurable quantities like transverse momentum ( $p_T$ ) and cone size,  $\Delta R = \sqrt{\Delta\eta^2 + \Delta\phi^2}$ , are used to identify and distinguish particles traveling in the transverse plane,  $(x, y)$  or  $(\eta, \phi)$ , from the longitudinal plane, along the  $z$  direction. Employing the conservation of momentum in the transverse plane, we can use the imbalance in transverse momentum required to ensure conservation of total transverse momentum of an event to infer the presence of an undetectable particle traveling in the transverse plane. The amount or quantity of this transverse momentum imbalance or missing transverse momentum is called missing transverse energy (MET) or  $E_T^{\text{miss}}$ . The presence of reconstructed  $E_T^{\text{miss}}$  in an event indicates the presence of very weakly interacting particle(s) which escape the detector undetected.

We define  $E_T^{\text{miss}}$  as the magnitude of the negative vector sum of the uncorrected transverse energy deposit of all the particles in an event.

$$E_T^{\text{miss}} = \left| - \sum_n (E_n \sin \theta_n \cos \theta_n \hat{\mathbf{i}} + E_n \sin \theta_n \sin \theta_n \hat{\mathbf{j}}) \right| = |\not{E}_T^x \hat{\mathbf{i}} + \not{E}_T^y \hat{\mathbf{j}}| \quad (5.2)$$

Where,  $n$  is the sum over all calorimeter energy deposits including energy deposits in towers, reconstructed energies (hits) or generator level particle energies. In order to measure  $E_T^{\text{miss}}$  accurately, a particle detector should be as near hemispherical as possible to

allow for complete measurement of the transverse momentum of all the particles belonging to an event. The CMS detector, provides a near hemicity with its nearly  $4\pi$  solid angle coverage. This near  $4\pi$  solid angle is achieved through the hadronic forward (HF) detector with little space allowing for the passage of the proton beams. Since according to conservation of momentum, the total transverse momentum before and after collision should be the same, by measuring the  $p_T$  of every detectable particle belonging to an event after proton-proton collision, the imbalance in  $p_T$  required to ensure the conservation of transverse momentum in the event, is ascribed to the momentum carried away by undetected particle(s). This idea is used to infer the presence of neutrinos W boson decay to an electron and an anti-electron neutrino;  $W \rightarrow e + \bar{\nu}$ , where the missing transverse momentum is used to infer the presence of the undetectable neutrino.

Since particle interactions involving supersymmetry and other beyond the standard model processes involves large  $E_T^{\text{miss}}$  due to the production of undetectable particle(s) during proton collisions,  $E_T^{\text{miss}}$  is the desirable quantity to use in many particle searches involving the possible production of new very weakly interacting particles. Standard Model particle interactions produces small  $E_T^{\text{miss}}$ . In any particle search which involves the production of new weakly interacting particle, it is imperative to accurately measure  $E_T^{\text{miss}}$ , as some standard model interaction processes like machine induced backgrounds from halo muons, mis-measured energy and mis-reconstructed particles and anomalous signals like spike can lead to large  $E_T^{\text{miss}}$  mimicking the signal for new particle(s).

## 5.8 Anomalous Signals

Anomalous signals are signals read from the electronics called *spikes* with abnormally large energy deposits in the avalanche photodiodes without any scintillation in the PbWO<sub>4</sub> crystals. They are produced when neutrons or charged hadrons like protons, strike directly ionizing the silicon of the photodiode producing an electronic signal in the absence of any crystal scintillation.

Because of no scintillation, they appear much earlier (negative) in ECAL measured arrival time and often populate the earlier time of the reconstructed hit (*rechit*) time distribution. Their energy deposit range from a few GeV to ECAL saturation energy of about 1.7 TeV. Since they do not electromagnetically shower in PbWO<sub>4</sub> crystals,

their electromagnetic energy shower shape is very isolated, with only one or two crystals contributing to the energy cluster. Spikes may also have positive time appearing late or delayed in their arrival time at ECAL populating the tails of the rechit time distribution. The late arrival time is due to the slow propagation of neutrons through the CMS detector.

Numerous test beam, collision data and simulation studies,[42], have been carried out towards understanding the properties of events with spikes and how they can be tagged and removed. These studies, reveal that spikes can be identified and removed using a topological energy variable constructed as  $1 - \frac{E_4}{E_1}$  known as the “*Swiss-Cross*” (SX).  $E_1$  is the energy deposit of the central (highest energy) crystal and  $E_4$  is the sum total of the energy of the neighboring four crystals in an  $(\eta, \phi)$  plane. A selection cut in  $\text{SX} > 0.95$  rejects more than 99% of isolated spikes with transverse energy greater than 10 GeV with very little impact on the efficiency of selecting electromagnetic EM showers. Other topological variables like  $1 - \frac{E_2}{E_6}$  and  $1 - \frac{E_2}{E_9}$ , where  $E_2$  is the sum of the energy of two crystals sharing the energy deposited and  $E_6(E_9)$  is the sum of the neighboring 6(pairs-of)(9) crystals in the  $(\eta, \phi)$  plane are used. The  $1 - \frac{E_2}{E_6}$  variable is used to identify isolated spikes whose energy deposit spread in two adjacent crystals while the  $1 - \frac{E_2}{E_9}$  is used to identify non-isolated spikes i.e. spikes which are found embedded in a supercluster. It has also been shown that applying selection cuts on the rechit time of  $\pm 3$  ns leads to more than 90% efficiency for rejecting spikes. However, in this thesis, we do not require such selection cuts on the rechit time as these rechits include rechits of possible delayed electromagnetic particles with arrival time beyond 3 ns produced during proton-proton collisions.

## Chapter 6

# Search Analysis for Long-Lived Particles

### 6.1 Analysis Strategy

Our analysis performs a search for events with late arrival time isolated photons with large transverse momentum,  $p_T$ . It is possible, these photons might be produced from the decay of a lightest neutralino,  $\tilde{\chi}_1^0$ . The lightest neutralino is itself produced from the cascade decay of supersymmetry particles gluinos and squarks which are themselves entirely new particles. In the SPS8 bench mark working point supersymmetry model, the late photon is accompanied by a gravitino,  $\tilde{G}$ , which is very weakly interacting with the detector material. As a result, the gravitino's presence is indirectly inferred using missing transverse momentum with magnitude as  $E_T^{\text{miss}}$ . Using timing measurements of the photon from ECAL sub-detector to detect a neutralino decay must be handled with ultimate care as there are many different sources of late photons due to timing miss-measurements and poor event reconstruction. A few of the sources of late photons are cosmic rays and other proton beam related activities called *beam halo* muons. Beam halo and cosmic muons can produce photons in ECAL through the process of *bremsstrahlung*. Other particles like high  $p_T$  neutrons by-passing the PbWO<sub>4</sub> crystals and hitting directly the photo-detectors, can similarly be observed as isolated, late photons. These are called *spikes*. These photons can be identified as isolated, having high  $p_T$  with ECAL time measurements showing that they arrive early as well as late compared to “normal”

photons produced at the nominal proton-proton interaction region whose average arrival time at ECAL is 0 ns. These different sources of background makes it challenging to distinguish a possible signal photon from the separate background photons. Thus, estimating the background contributions to possible signal events sample requires using true proton-proton collision events rather than simulated events which do not accurately mimic proper timing measurements for this kind of background events as is normally the case in most physics analysis. Nevertheless, as it is with most hadron collider physics analysis, exploring the use of the number of jets in the event selection can most often reduce dramatically the background contamination to possible signal sample. It is not different with this analysis, where we have employed *jet multiplicity* both as a possible signal definition requirement for the production of high  $p_T$  isolated and delayed photons but also as a detector variable for reducing and at times discriminating background from possible signal events. Our motivation is to perform a model independent search while at the same time guided by SUSY models such as SPS8 benchmark model and GGM, where the production of a high  $p_T$  isolated, delayed photon in association with a number of jets and large  $E_T^{\text{miss}}$  constitutes a typical new physics event which could be produced at the LHC. Thus, our simulated events from SPS8 or GGM model, serves both as a guiding model for understanding a possibly observed event with a new physics signature and also for setting limits on some fundamental parameters with respect to these models in case we observed no significant excess over SM prediction.

A typical signal event considered in this analysis for the existence of a neutral massive long-lived particle decaying into a photon, is the detection of a late photon arriving at crystals in the ECAL sub-detector of CMS associated with jets and large  $E_T^{\text{miss}}$ . In the SPS8 model with R-parity conservation (RPC), the neutralino ( $\tilde{\chi}_1^0$ ) is the long-lived neutral particle and decays into a high  $p_T$  isolated and late arrival photon in association with at least two jets and a weakly interacting gravitino ( $\tilde{G}$ ) in a signal event. The jet multiplicity is from jets produced in the cascade decay of possibly higher mass SUSY particles into the neutralino. The gravitino ( $\tilde{G}$ ) presence is inferred using the transverse momentum imbalance whose magnitude is  $E_T^{\text{miss}}$ . Using this signal events signature, we divide our data samples into possible signal regions (SR) and control regions (CR) and use these CRs for estimating background contributions from beam related activities, miss reconstructed standard model processes and detector effects. We also use events

with negative photon time as a control sample for studying veto methods for rejecting and estimating background contribution from non-collision events.

### 6.1.1 Signal and Background Modelling

We begin generating signal events according to the SPS8 GMSB model by producing Supersymmetry Les Houches Accord (SLHA) files using the SUSY software package *ISASUSY*,[56]. *ISASUSY* contains the program *ISAJET* which is used to determine SUSY mass spectrum and decay parameters according to a given SUSY model. The input to *ISAJET* are the fundamental parameters  $\{\Lambda, M_{\text{mess}}, N_5, \tan(\beta), sgn(\mu), C_{\text{grav}}\}$ . According to the SPS8 benchmark model, we have chosen,  $sgn(\mu) = 1$ ,  $\tan(\beta) = 15$ ,  $N_5 = 1$  and  $M_{\text{mess}} = 2\Lambda$  allowing  $C_{\text{grav}}$  and  $\Lambda$  as the free parameters to study the different life time and mass of the neutralino. The output of *ISAJET* is a SLHA file that has the SUSY mass spectrum and decay rates and branching ratios according to the SPS8 model. *HDECAY* is used as the tool for simulating the decay of SUSY particles including the neutralino to gravitino. The neutralino can also decay into  $Z$  bosons, *Higgs* and  $e^+e^-$  with a gravitino but with about 83 to 94% of its decay into  $\gamma + \tilde{G}$ . 97 to 99% of all the events contain at least a single photon. These SLHA files containing information about the SUSY mass spectrum and decay rates is fed into a *PYTHIA6*, [57], proton-proton collision event generation interface of the CMS software (CMSSW) event generation and reconstruction software. In our case **CMSSW\_5\_3\_2\_patch7** version of the software is used. The center of mass energy for these proton-proton collisions  $\sqrt{s} = 7\text{TeV}$  for generating these SUSY events. Production, interaction and decay of these events in the CMS detector is simulated using the GEANT4 package,[58]. Since a possible background process to our analysis is miss-measurement of the timing of photons produced by Standard Model processes like multi-jets and  $\gamma +$  jets processes produced from strong interactions described by quantum chromodynamics (QCD), we also generate and simulate at leading order cross-sections using PYTHIA 6 and GEANT4 a small sample of these events for determining an estimate of time miss-measurement of our signal Monte carlo events. Digitization and event reconstruction in terms of its constituent objects like jets, photons, muons and electrons, after production and decay in the full CMS detector is later again performed during analysis using the CMSSW software.

## Simulated Signal Events

Our signature for signal events within the SPS8 benchmark model are events containing the following:

- at least one energetic delayed photon,
- a number of high transverse momentum jets,
- large missing transverse momentum,

## Simulated Background Events

QCD multi-jets and  $\gamma +$  jet(s) events with high  $p_T$  photons with miss reconstructed photon time is a possible background source. In order to understand and calibrate for any such miss measurements, we use simulated or Monte Carlo  $\gamma +$  jet(s) events to perform such a study and for sanity check with MC time measurements. Events with  $W$  and  $Z$  decay and  $t\bar{t}$  with large missing transverse momentum, jets and miss-reconstructed photons could also possibly contribute to background, however, these processes produced mostly in-time events with rarely any photons with large late times. Thus, we consider this background to be negligible and do not perform any MC studies for them.

### 6.1.2 Datasets

The dataset used in this analysis was produced during proton-proton collisions of LHC Run 1 in 2012 with the center of mass energy,  $\sqrt{S} = 8$  TeV. The CMS detector recorded data equivalent to total integrated luminosity of  $19.1 \text{ fb}^{-1}$ .

## Data

These datasets contain events with at least a single photon triggered. Only datasets for which the luminosity-sections are certified as GOOD are used. The *jason* file with this good luminosity sections is **Cert\_8TeV\_PromptReco\_Collisions12\_JASON.txt**. Table 6.1 shows the dataset and their corresponding integrated luminosity as used in this analysis.

<b>Dataset</b>	<b>Recorded Luminosity</b> [ fb <sup>-1</sup> ]
/Run2012B/SinglePhoton/EXODisplacedPhoton-PromptSkim-v3	5.1
/Run2012C/SinglePhoton/EXODisplacedPhoton-PromptSkim-v3	6.9
/Run2012D/SinglePhoton/EXODisplacedPhoton-PromptSkim-v3	7.1
/SingleElectron/Run2012A-22Jan2013-v1/AOD	5.2
/DoubleElectron/Run2012C-22Jan2013-v1/AOD	4.8

Table 6.1: Dataset and corresponding integrated luminosity totaling 19.1 fb<sup>-1</sup> used in this analysis

### Background and Signal Monte Carlo

The Monte Carlo (MC) samples are produced taking into account the Summer 2012 prescriptions carrying information on the calibration and alignment conditions of the CMS detector with pile up (PU) conditions at 8 TeV. We generate QCD events at leading order (LO) cross-section ( $\sigma$ ) and normalized to the 19.1 fb<sup>-1</sup> integrated luminosity. The official CMS MC production events for signal GMSB contains 50000 events. Performing a quick sanity check by measuring and comparing the generated neutralino lifetime ( $c\tau$ ) to its lifetime from SLHA files produced with ISAJET, we observed that most of the generated neutralino events had their lifetimes reduced by a factor of about 3. In order to extend our study to longer neutralino lifetimes, we produced private GMSB samples, generated and simulated with the same conditions as the official CMS samples but having correctly produced and measured neutralino lifetimes thus extending the GMSB sample to include neutralinos with long lifetimes. These combined GMSB MC samples from private and official simulations allow our search analysis to scan neutralino ( $\tilde{\chi}_1^0$ ) lifetimes,  $c\tau$  from 250 mm to 12000 mm for each  $\Lambda_m$  point with  $\Lambda_m$  ranging from 100 TeV to 180 TeV as shown in table 6.2. Table 6.3 also show the  $p_T$  range for the processed QCD samples.

$\Lambda$ [TeV]	$c\tau$ (mm)	$\sigma_{LO}$ (pb)	Number of Events	Branching Ratio
100	250-12,000	0.368	50,000	0.9444
120	250-12,000	0.133	50,000	0.9042
140	250-12,000	0.0574	50,000	0.8711
160	250-12,000	0.0277	50,000	0.8464
180	250-12,000	0.0145	50,000	0.8282
220	250-12,000	0.0044	50,000	0.8282
260	250-12,000	0.0015	50,000	0.8282
300	250-12,000	0.0008	50,000	0.8282

Table 6.2: The signal GMSB SPS8 MC samples for difference  $\Lambda$  and Branching Ratios used in this analysis

$\hat{p}_T$	$\sigma_{LO}$ (pb)	Number of Events
50 ~ 80	3322.3	1995062
80 ~ 120	558.3	1992627
120 ~ 170	108.0	2000043
170 ~ 300	30.1	2000069
300 ~ 470	2.1	2000130
470 ~ 800	0.212	1975231

Table 6.3: The  $\gamma+$  jets samples used in this analysis

## 6.2 Event Selection

The major background events to this analysis are events which are not produced from the nominal proton-proton collisions. These events can be separated into three major categories; *Halo muons*, *Spikes* and *Cosmic muons*. In addition to these events, there are also QCD events which mimic the  $\tilde{\chi}_1^0 \rightarrow \gamma + \tilde{G}$  decay due to photon miss reconstruction and measurement of fake  $E_T^{\text{miss}}$ . Contribution from  $\gamma+$  jets events can also be regarded as background events especially in cases there is a real isolated photon and a fake  $E_T^{\text{miss}}$  due to miss identification of jets as photons. Even though the event topology for most  $\gamma+$  jets events is quite different from that of GMSB signal events.

Another possible background contribution, in addition to QCD multi-jets events, events from ElectroWeak (EWK) decay including  $W \rightarrow e + \nu$  and  $t\bar{t}$  decays, where the top ( $t$ ) decays to a  $b$  quark and a  $W$  100% of the time. The electron is miss reconstructed and thus miss identified as a photon and real  $E_T^{\text{miss}}$  is measured due to the presence of the neutrinos ( $\nu$ ). We can easily reduce this background by requiring high jet multiplicity events since most of these EWK and QCD events contains low number of high  $p_T$  jets in them. In order to maintain a high background rejection and good signal selection efficiency, we select events with at least two jets. This helps to reduce EWK and other low jet multiplicity backgrounds contributions prior to additional photon quality selections based on the isolation and electromagnetic shower profile. Using ECAL time measurements, our signal acceptance regions are events with photons whose time is between  $3 < t_\gamma < 13$  ns. This cuts allows us to avoid events with high spike contamination.

In addition to collision backgrounds mentioned in the previous section, non-collision originated background events like Cosmic muons, beam halo muons and ECAL spikes contain photons with large reconstructed time and large  $E_T^{\text{miss}}$  measurements.  $E_T^{\text{miss}}$  measurements includes  $p_T$  from all reconstructed particles in an event with the assumption that these are events from the nominal proton-proton collision. However, not all events are produced from collision. Cosmic muons, beam halo muons, spikes, ECAL and HCAL noise can all contribute to the total sum of the measurable event  $p_T$  imbalance. In some events these provide the major contributions to  $E_T^{\text{miss}}$  calculations. We begin by selecting events with at least a good vertex, quality jets, satisfying ECAL spike cleaning, DT time cosmic muon cleaning and CSC tight halo-muon cleaning criteria. This event selection criteria is very useful in reducing contributions from non-collision events.

A typical diagram showing both non-collision and collision backgrounds in neutralino production and decay from LHC proton-proton collision within the CMS detector is shown in figure 6.1. A typical GMSB decay of the neutralino is also shown in this diagram indicating the two different sources for delayed photon produced from this decay.

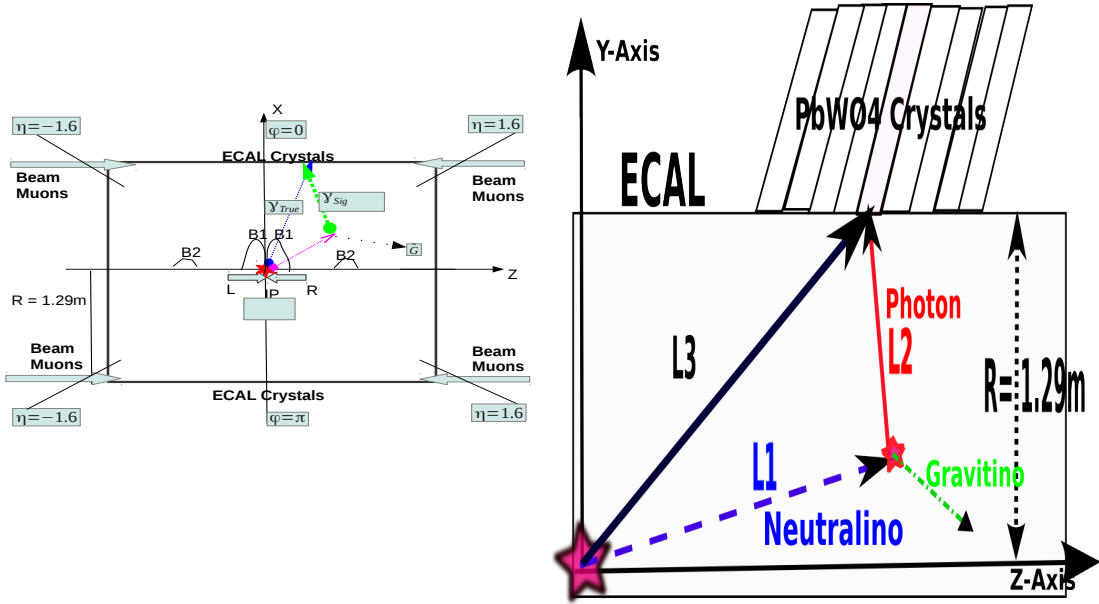


Figure 6.1: Schematic diagram showing  $\tilde{\chi}_1^0 \rightarrow \gamma + \tilde{G}$  decay topology within the ECAL volume of the CMS detector. Proton beams are also shown showing the possible production of collision and non-collision delayed photons

### 6.2.1 Trigger

Our pre-event selection begins online by selecting only events which pass our online higher level trigger (HLT). The HLT trigger used for our  $\sqrt{S} = 8$  TeV proton-proton collision analysis is the `HLT_DisplacedPhoton65_CaloIdVL_IsoL_PFMET25` seeded by `HLT_L1SingleEG12` level 1 trigger. It was developed primarily for the study of displaced photons. To avoid bias in event selection towards any particular model, this trigger only requires that an accepted event contains an isolated photon with a  $p_T$  threshold of 65 GeV/c and  $E_T^{\text{miss}}$  above 25 GeV. The photon shower shape must also satisfy  $0.1 < 0.S_{\text{Minor}} < 0.4$ . We study our trigger efficiency and turn-on curve (efficiency becomes close to 100%) for selecting events with delayed photon candidates. In order to avoid any correlation between the photon and  $E_T^{\text{miss}}$  variables, we study efficiency for each variable separately using another trigger `HLT_Photon50_CaloIdVL_IsoL`. The selected photon candidates for studying this HLT photon efficiency must pass

our offline photon selection candidate criteria shown in table 6.4. The HLT photon selection efficiency for  $p_T$  is defined as the fraction of offline reconstructed photons to those triggered by *HLT\_IsoPhoton50* photon candidates within  $\Delta R < 0.5$ . Similarly, the  $E_T^{\text{miss}}$  HLT efficiency is defined as the fraction of events containing at least a jet and  $E_T^{\text{miss}}$  more than the HLT required  $E_T^{\text{miss}}$  of 25 GeV. The results of the trigger efficiency measurements are shown in figure 6.2 against photon  $p_T$  and  $E_T^{\text{miss}}$ . These efficiency studies are made using the *HLT\_Photon50\_CaloIdVL\_IsoL* trigger which has no  $E_T^{\text{miss}}$  and jet multiplicity requirement as the denominator and the *HLT\_DisplacedPhoton65\_CaloIdVL\_IsoL\_PFMET25* as numerator. A *SinglePhoton* dataset is used to verify these efficiency while and GMSB and  $\gamma +$  jets samples is used to derive any correction factors between data and MC events.

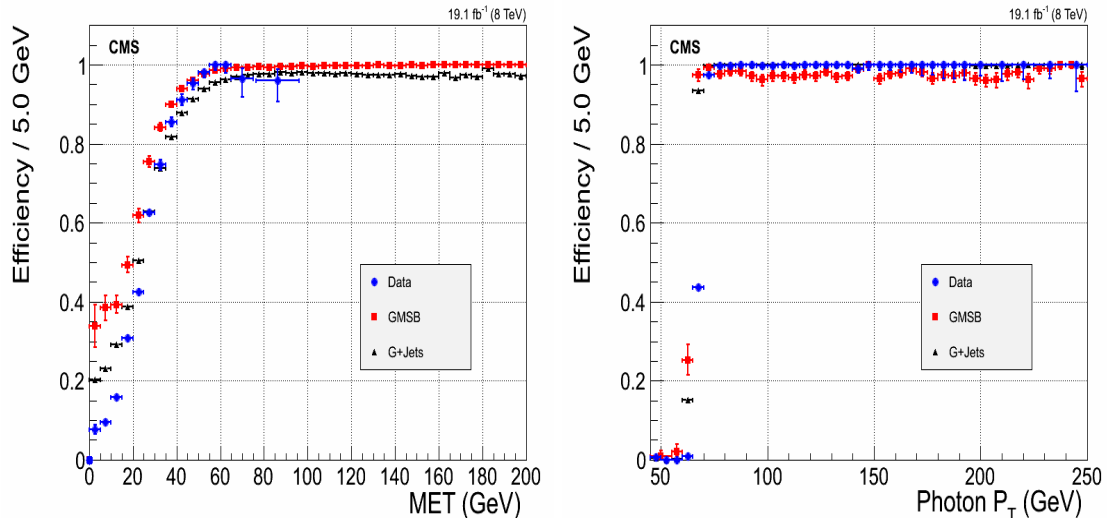


Figure 6.2: Trigger efficiency turn-on curves for photon  $p_T$  and  $E_T^{\text{miss}} > 25$  GeV (left) and for  $E_T^{\text{miss}}$  with photon  $p_T > 80$  GeV/c (right). The  $\gamma +$  jets samples require photon  $p_T > 170$  GeV/c for selecting events with true  $E_T^{\text{miss}}$ .

### 6.2.2 Offline Selection

Our offline event selection requires candidate events in addition to passing our HLT trigger, contain at least a single photon, a jet and  $E_T^{\text{miss}}$ . The photon object collection used in our analysis is an extended collection of standard CMS Egamma photon objects collections to include events classified as “*out-of-time*”. This classification was

performed during the official CMS supercluster reconstruction process. This enlarged photon sample include events like spikes, ECAL noise, photons from beam halo and cosmic muons and detector malfunctions. It is also entirely possible that this collection also contains true candidate delayed photons which is our signal events. The selected photons are required to pass the photon selections criteria in table 6.4.

<b>Photon Identification and Selection Criteria</b>	
<b>Criteria</b>	<b>Requirement</b>
Event leading photon must have $p_T(\gamma^1)$	$> 80 \text{ GeV}$
Other photons in event must have $p_T(\gamma^{>1})$	$> 45 \text{ GeV}$
$ \eta_\gamma $ , (Barrel Only),	$< 3.0 (< 1.5)$
$S_{\text{minor}}$	$0.12 \leq S_{\text{Minor}} \leq 0.38$
$\mathbf{H}/\mathbf{E}$	$< 0.05$
$\Delta R(\gamma, \text{track})$	$> 0.6$
HCAL Iso	$< 4.0$
ECAL Iso	$< 4.5$
Track Iso	$< 0.2$
Photon Isolation cone size $\Delta R(\gamma, \text{otherparticle})$	$< 0.4$
Topological Spike cuts	$1 - E_6/E_2 < 0.98, 1 - E_4/E_1 < 0.98$

Table 6.4: The photon identification and selection criteria used in this analysis

The presence of jets as associated particles from gluino cascade decay and the gravitino ( $\tilde{G}$ ) from neutralino decay,  $\tilde{\chi}_1^0 \rightarrow \gamma + \tilde{G}$  requires jet identification and  $E_T^{\text{miss}}$  or  $\cancel{E}_T$  selection criteria as well. Our jet and  $E_T^{\text{miss}}$  or  $\cancel{E}_T$  selection criteria is based on the particle-flow (PF) algorithm. Additional  $\cancel{E}_T > 65 \text{ GeV}$  due to the flatness of the HLT trigger efficiency against  $E_T^{\text{miss}}$  (see figure 6.2). Table 6.5 show a summary the jet identification and selection criteria with the threshold requirements used in this analysis.

### Jet PF identification selection criteria

Criteria	Requirement
Jet $p_T$	$> 35 \text{ GeV}$
Number of Jet constituents	$> 1$
Charge EM energy fraction (CEF)	$> 0.99$
Neutral Hadron energy fraction (NHF)	$< 0.99$
Neutral EM energy fraction (NEF)	$< 0.99$
If $ \eta $ of jet is $> 2.4$ , Charge Hadron energy fraction (CHF)	$> 0$
If $ \eta $ of jet is $> 2.4$ , Charge multiplicity (NCH)	$> 0$
$\Delta R(\gamma, \text{jet}) = \sqrt{(\phi_\gamma - \phi_{\text{jet}})^2 + (\eta_\gamma - \eta_{\text{jet}})^2}$	$> 0.3$

Table 6.5: The Jet ID selection used in this analysis

### $E_T^{\text{miss}}$ Corrections

During the official CMS electromagnetic supercluster reconstruction, timing cuts of  $|t_{RECO}| > 3.0 \text{ ns}$  in EB is used for cleaning “out-of-time” events. As a result, the  $p_T$  contribution from out-of-time photon events is not included in the calculation of  $E_T^{\text{miss}}$  or  $\cancel{E}_T$ . This introduces a difference in the calculation of  $\cancel{E}_T$  for “in-time” events ( $|t_\gamma| < 3.0 \text{ ns}$ ) and “out-of-time” events ( $|t_\gamma| > 3.0 \text{ ns}$ ). Since the out-of-time photon  $E_T$  is not included in the sum total transverse momentum of an event to derived the total transverse momentum imbalance, we correct for this, by adding the out-of-time photon  $E_T$  to the PF-MET measured during CMS  $\cancel{E}_T$  reconstruction. We defined an additional variable,  $\cancel{E}_T^\gamma$ , accounting for this correction and use this variable in our event selection criteria.

1.  $\cancel{E}_T$ : PF-MET,  $\cancel{E}_T$  from CMS standard  $E_T^{\text{miss}}$  measurements.
2.  $\cancel{E}_T^\gamma$ : PF-MET with photon  $E_T$  added i.e  $\cancel{E}_T^\gamma = \cancel{E}_T + E_T$  of the out-of-time photon.

Our signal event selection criteria is defined as events with  $\geq 1 \gamma + \geq 2 \text{ jets} + \cancel{E}_T^\gamma > 60 \text{ GeV} + \cancel{E}_T > 60 \text{ GeV}$

We use a control sample to perform a closure test of our background estimation procedure. The selection criteria is events with  $\geq 1 \gamma + \leq 1 \text{ jet} + \cancel{E}_T > 60 \text{ GeV} + \cancel{E}_T^\gamma > 60 \text{ GeV}$

### 6.2.3 ECAL Time

The photon arrival time at ECAL is our main observable for distinguishing background from signal. However, the presence of spikes, noisy crystals and pile-up events, require measuring the photon time with methods which are robust to timing bias from such events. There are different ways to measure the photon time using ECAL. The reference time is the time measured from a relativistic electromagnetic object like a photon produced from nominal proton-proton collisions arriving at ECAL in an average time of zero. The photon time is measured using either of the following methods:

- *Seed Time*: Time from the highest energy crystal, which is not a spike, of the photon supercluster.
- *Cluster Time*: Error weighted average time of all the crystals in the seed basic-cluster of the photon supercluster.

Timing reconstruction as described in chapter 4 is the extraction of time from the pulse shape through a fitting method. The  $\chi^2$  obtained from the fit determines how well the time is reconstructed. One way of rejecting fake photons which are either jets miss-identified as photons or spikes is to use the fitted  $\chi^2$ . Studies performed have shown that a  $\chi^2 < 4$  cut improves the ECAL timing resolution by rejecting spikes and anomalous photon events as possible. Figure 6.3 shows a comparison between the pulse shape profile of a spike and that of a good event.

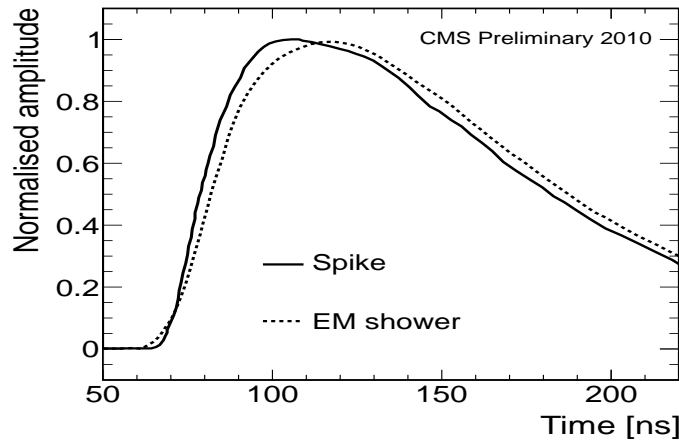


Figure 6.3: Pulse shape profile showing a spike (solid line) and a real photon (dashed line) from data.

In this thesis, we measure time using the seed crystal time approach. Our choice of seed time is based on a number of independent timing analysis performed comparing the timing resolution obtained from cluster time to the seed time. We observed the cluster timing method to be very biased towards the time of an isolated spike especially when the spike is embedded in a photon object. The timing resolution especially for large timing events is much better compared to the cluster time measurement method which is an essential region when searching for new long-lived particles. Figure 6.4 shows the timing measurements of photons using either seed time or cluster time. The seed time show an approximate timing resolution of 400 ps compared to 450 ps with a broad timing tail from using the error weighted average cluster time. The cluster time method is also computational time and resource consuming.

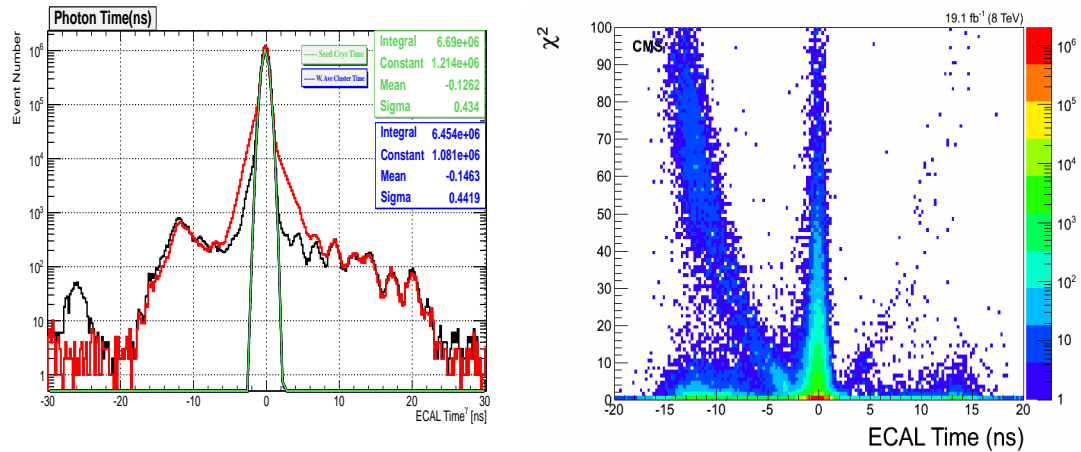


Figure 6.4: Timing distribution of photons showing timing measurements using seed crystal (black) and using Weighted Average basic cluster time (blue). Resolution ( $\sigma$ ) from seed time is better compared to that for cluster time which is computationally intensive. Together with the  $\chi^2$ , the seed time performs better in identifying anomalous timing objects.

Monte Carlo simulation of ECAL timing is challenging as the time of anomalous events such as spikes and noisy crystal channel present during data taking aren't well simulated. To account for MC and data timing measurement differences, We use QCD simulated  $\gamma + jets$  events and select events containing only one or two jets and study the

distribution of the difference between the generated time ( $T_{GEN}$ ) and the reconstructed MC event time ( $T_{RECO}$ ) in a timing window of [-2, 2] ns. Comparing this difference to data, the difference in the mean time between the data and MC  $\gamma +$  jet sample is used to smear the reconstructed time of the MC samples to be comparable to true reconstructed time in data. A difference of about 125 ps is observed between the timing from data and MC. Timing from the smeared MC sample show a close agreement with data. Figure 6.5 show this comparison before and after timing calibration (smearing adjustment) is applied on the MC samples.

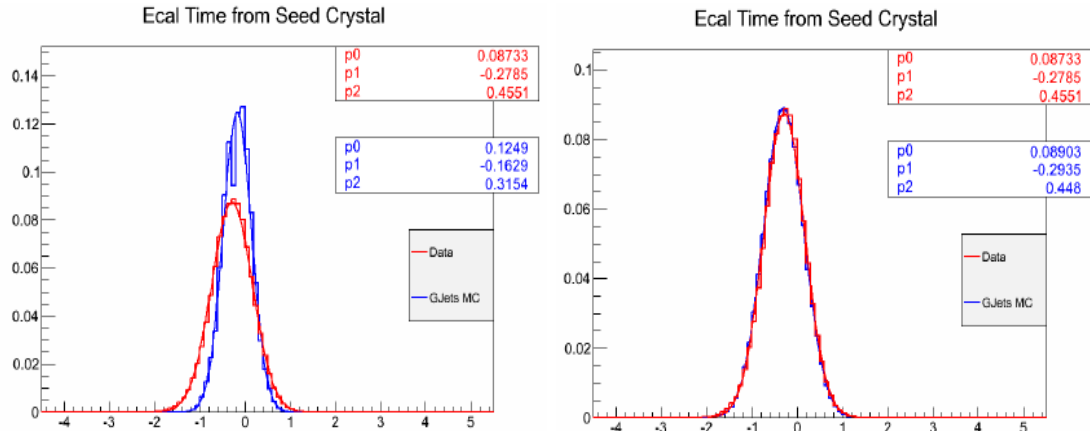


Figure 6.5: Timing distribution of photons showing timing of data and MC  $\gamma +$  jets (blue) samples and data (red) before (left) and after (right) timing Calibration is applied to MC.

It is worth noting that the difference of 125 ps between  $T_{RECO}^{MC}$  and  $T_{RECO}^{DATA}$  compared to 500 ps ECAL timing resolution is not enough to influence event selection, however event distribution in the tails remains a major concern.

The ECAL timing distribution for photons with  $pt > 50$  GeV in the ECAL (barrel and endcap inclusive i.e  $|\eta_\gamma| < 3.0$ ) show timing distributions (see figure 6.6)

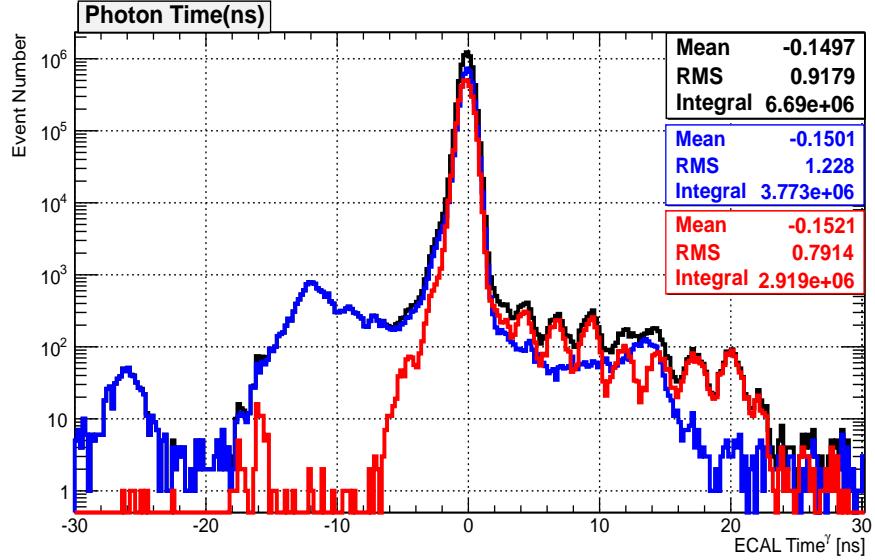


Figure 6.6: ECAL timing distribution of photons in barrel (EB), endcap (EE) and all of ECAL (ALL ECAL) with  $p_T > 50$  GeV from data. A 2.5 ns delay timing structure is observed in endcap subdetector.

with a clear 2.5 ns discrete pattern with most of these photons arriving in the endcap,  $1.47 < \eta < 3.0$  compared to the barrel,  $|\eta| < 1.47$ . These are photons produced from collisions of *Ghost* and *Satellite* bunches with either the main proton collision bunch or *Ghost/Satellite*. They contribute an irreducible amount to the photon time distribution which is very challenging to reject or estimate quantitatively. A rough estimate can be obtained by looking at ratio of the proton population in the filling profile of the LHC RF cavities as mentioned in section 3.1.5 of chapter 3 which gives a factor  $10^{-5}$  compared to contributions from the main proton-proton bunch collision. It is observed that contribution from ghost bunches is in the endcap crystals, since very few these photons are produced with enough  $p_T$  compared to those from main proton bunch collisions. And even if they do, the ratio of photons from these secondary proton collision to that of the main proton-proton collision is of the order of  $10^{-5}$  at most. As a result of this, we do not use the endcap in this analysis in addition to the fact that timing resolution in the endcap is relatively poor compared to the barrel. We check and validate this factor  $10^{-5}$  using events with  $Z \rightarrow e^+e^-$  since  $Z$  events do not require high  $p_T$  during production and must should capture the 2.5 ns timing pattern if present from

ghost/satellite collisions. We study electron candidates with time within [-2.0, 2.0] ns window. We use this in our background estimation method testing as will be discussed in future sections.

### Delayed Photon Source

With a well time calibrated ECAL and good MC to data time agreement, we can study the source of delayed photons from neutralino decay in ECAL using its decay kinematics. There are two possible sources for delayed photon from neutralino decay. From Figure 6.1, an estimated photon arrival time at ECAL can be given by the following methods:

- From slow moving neutralinos:  $\Delta t_1 = (L_1/c\beta) - (L_1/c)$
- From non-directpath traveled:  $\Delta t_2 = (L_1 + L_2 - L_3)/c$
- ECAL measured time =  $\Delta t_1 + \Delta t_2$

Figure 6.7 shows the distribution of  $\Delta t_1$  and  $\Delta t_2$  indicating that most of our late arrival photons are produced from the decay of slow moving neutralinos, i.e.  $\beta \ll 1$ , as opposed to photons from non-direct flight or travel path to ECAL. These neutralinos are produced with low  $p_T$  such that the ratio  $\frac{p_T}{m_{\chi_1^0}} \ll 1$ .

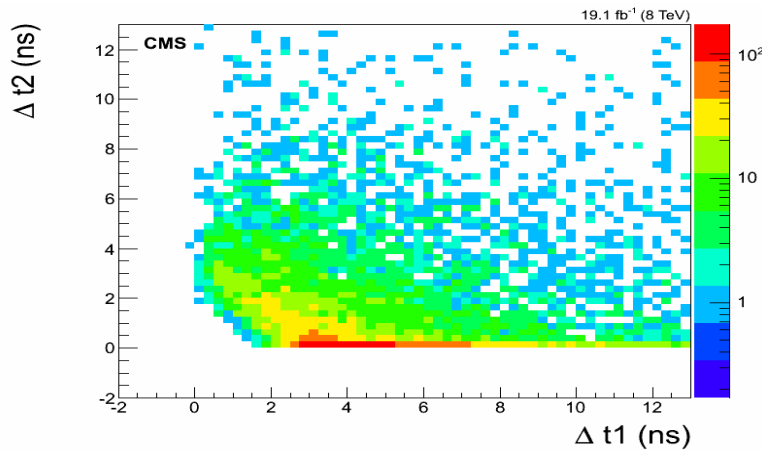
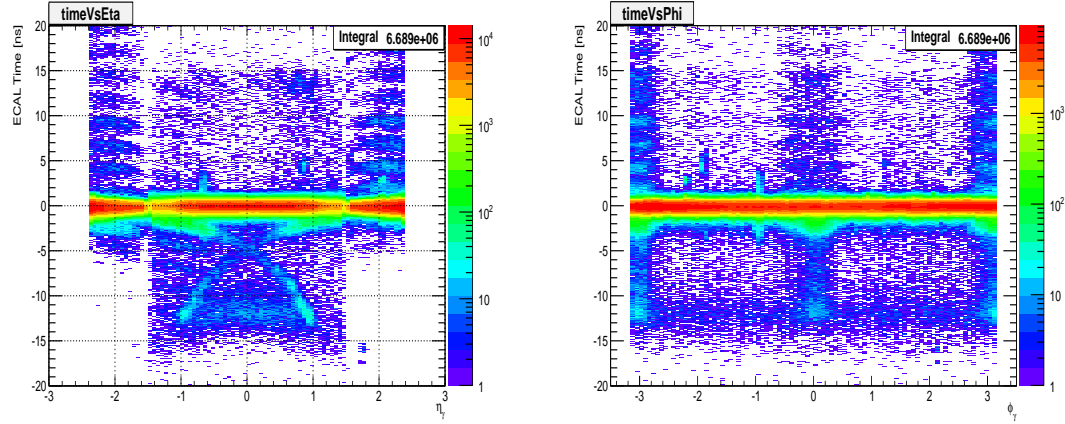


Figure 6.7: Sources of delayed photons produced from neutralino decay in the SPS8 model with  $\Lambda = 180$  TeV and  $c\tau = 6000$  mm arriving at ECAL.

### 6.3 Background Estimation

Our background estimation strategy is to first identify and reject as much non-collision background and anomalous events as possible then perform an ABCD background estimation technique on the irreducible residual background. We do this by comparing photon kinematic properties for in-time and off-time photon events. Separating our data sample into jet multiplicity and negative, in-time and positive time enable our approach to be possible. To better understand the different background sources and their contribution we make a two dimensional histogram of the photon  $\eta$  and  $\phi$  against the photon seed time and a one dimensional histogram of the timing distribution for different jet multiplicity events. These events pass the loose selection criteria for photons, jets and  $\cancel{E}_T$  already described in the previous section. The photon ECAL time Vs  $\eta$  and  $\phi$  inclusive 2-D distributions are shown in figure 6.8



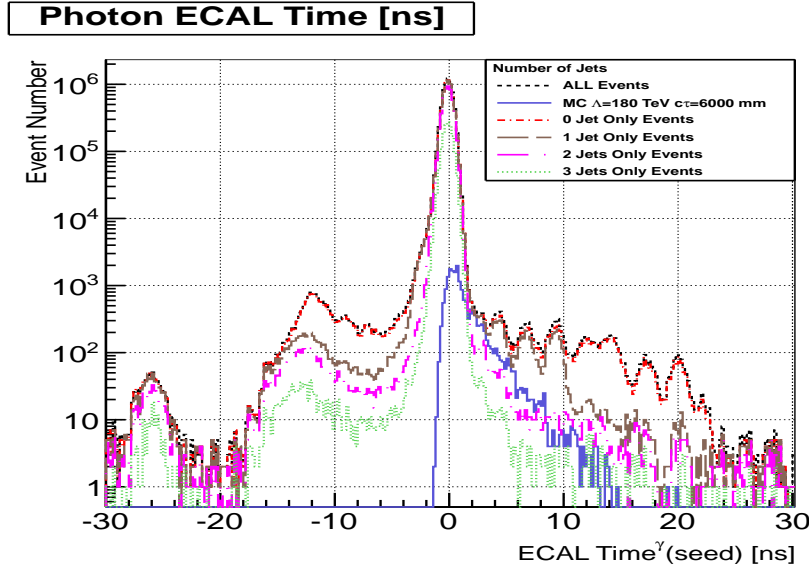


Figure 6.8: ECAL time against  $\eta$  (left) and ECAL time against  $\phi$  (right) for photons with  $p_T > 60$  GeV from data. The lower plot shows the photon timing distribution for events with different jet multiplicity.

The histograms in figure 6.8 show contributions from quite a variety of sources. The possible sources considered in this analysis include: QCD processes which we consider to be a combination of  $\gamma$ +jets, multijets and other processes producing photons from nominal proton-proton main bunch collisions. Most of the QCD processes are expected to have minimal contribution to large timing photons and  $E_T$  except due to timing miss-reconstruction and  $E_T$  miss-measurements or miss-identification of jets as photons. The events with significant contributions of possible or true large ECAL time measurements are produced from machine induced backgrounds (MIB)(arising from ghost/satellite bunch collisions) or beam halo muons, cosmic muons and anomalous events like spikes. These event do not only contribution significantly large photon times but also to large  $E_T$  which is our signal selection sample. We employ a data driven background estimation technique in this analysis described briefly as follows:

- Divide the dataset into individual samples peculiar to the expected kinematics and observation of each individual background source,
- Identify observable based on its kinematics which can be used as variables to

identify or tag and reject a particular background contribution with an acceptable amount of efficiency,

- Used alternate samples particular to each background source to calculate and verify the event tagging and miss-tag rate or efficiency,
- Use the tagging and miss-tag rates to estimate the background contribution of each individual background source in a well defined control region (CR) or sample,
- Use another CR as a closure test sample to verify our background estimation method.

All events are selected to be in the barrel i.e  $|\eta_\gamma| < 1.47$  as the overwhelming contribution of ghost/satellite bunch collisions observed in the endcap (EE)(see figure 6.6) and poor timing resolutions ( $\approx 3.0$  ns) make it very challenging to extend this analysis to include the endcap (EE). Our data driven method background estimation strategy involves splitting our single photon dataset into two major samples: Events with *Nominal or in-time* photons whose photon ECAL time is within  $\pm 2$  ns containing at least 2 jets, and events with *off-timing* photons where the photon ECAL time is  $2.0 < t_\gamma < 13.0$  ns and  $-10.0 < t_\gamma < -3$  ns with containing 0 or 1 jets. Our signal events are events containing photon(s) with ECAL time,  $2.0 < t_\gamma < 13.0$  ns, with at least 2 jets and large  $\cancel{E}_T$ . Our motivation is to avoid the observed spike overpopulated region with photon time ,  $t_\gamma \approx -12$  ns and because high jet multiplicity events are not usually MIB or non-collision events produced with  $p_T$ . On the other hand, nominal photons from QCD interaction are mostly produced in-time in association with more than 0 jets.

By comparing these two samples, we develop kinematics variables for studying and reducing contributions from collision and non-collision backgrounds.

### 6.3.1 Non-Collision Backgrounds

#### Halo Photons

##### Beam Halo

In addition to ghost/satellite bunches generating collisions events during collision, protons in ghost/satellite bunches can interact with collimators or gases such as H<sub>2</sub>, CO<sub>2</sub>

and others in the beam pipe leading to the production of high energy muons which later bremsstrahlung and shower directly in the calorimeter detectors. Main bunches due to betatron oscillations(departure of particles from nominal orbit in the transverse direction) can also through inelastic scattering with gas molecules in beam pipe about 550 m up from interaction point (IP)(since beam cleaning is not being 100% efficient), scattering on tertiary collimators (TCT) about  $z = 150$  m from IP and beam dump at about 150 m upstream CMS detector, produce through cascade decay energetic muons(sometimes muons with about 1 TeV) which bremsstrahlung in calorimeter detectors.

This kind of background from beam is referred to as *Machine Induced Background* (MIB) or *Beam-Induced Background* (BIB) and its contribution is called non-collision backgrounds as these are events observed in the detectors but not produced from the interaction point (IP). Throughout these thesis, we will refer to this kind of events as *Beam Halos or halos*. Because, they produce very high transverse momentum photons which can also be miss-identified as jets arriving in-time or out-of-time, they are a very important background in any analysis. In the later section, we will also show how we have developed new methods to identify and reject these kind of events and estimate its possible contribution to our analysis.

Muons with energy up to 1 TeV are produced when proton beam collides with collimators at  $z = 150$  m from the CMS detector interaction point or when proton beams collide with residual beam gas in the beam pipes. These are referred to as Beam-Induced Backgrounds (BIB). These muons through the process of bremsstrahlung produce high  $p_T$  photons with significantly large ECAL time, deposit their energy in ECAL crystals. The rate of BIB produced photons depend on the beam current and the operational conditions of the LHC such as machine optics, collimator settings, residual gas densities and filling scheme. These muons which travel in a near parallel flight path to the direction of main proton bunch in the beam pipe are referred to as *halo muons*. We expect halo muons to produce muon tracks in the Endcap muon systems (CSC and RPCs) with corresponding associated ECAL electromagnetic cluster in the ECAL. Halo muons can travel from one side of the detector, along the  $z$ -direction, to the other side of the detector if produced with sufficient energy. Their Time-Of-Flight (TOF) with respect to a potential hit position in the ECAL sub-detector can be estimated and

measured. The expected arrival time at ECAL of a halo muon traveling parallel along the beam line is estimated using it kinematics given in equation 6.1.

$$t_{\text{ECAL}}^{\text{expected}} = -1/c \left( \pm Z_{\text{cluster}} + \sqrt{Z_{\text{cluster}}^2 + R_{\text{cluster}}^2} \right) \quad (6.1)$$

$Z_{\text{cluster}}$  is the photon supercluster position or longitudinal distance along  $z$ -axis from nominal interaction point,  $R$  is the radial distance of the cluster from the beam line which is equal to  $R_{EB,\text{ECAL}} = 1.29$  m and  $c$  is the speed of light. One can further show that their expected arrival time in ECAL entirely depends on potential hit positions in ECAL and hence  $\eta$ . This is by reducing equation 6.1 to 6.2.

$$t_{\text{ECAL}}^{\text{expected}} = -\frac{R_{\text{cluster}}}{2c} \exp(-\eta) \quad (6.2)$$

Using this expression, we can compared halo flight path  $\eta$ -dependence as expected to what is observed from data. Our result in figure 6.9(*bottom, right*) confirm our expectation that most of the halo muons are produced from BIBs and tend to always produced photons with earlier (negative) arrival time in ECAL. In addition to using halo flight path to tag photons produced from halo muons, we also use halo muon hit positions in the Cathode Strip Chambers (CSC) matched to photon supercluster positions in the ECAL calorimeter. This is possible since halo muons are not bent in the azimuthal ( $\phi$ ) direction by the magnets and are mainly located around the  $y = 0$  plane. By measuring the difference in  $\phi$  between the CSC segment position and the ECAL photon cluster, we can associated with high percentage halo muons to photons produced from halo muons in ECAL. We call these photons *Halo Photons* and their matching to these halo muons is represented by a variable we call  $CSC(\text{Seg}, \gamma)\Delta\phi$ . A matching to within 3 deg shown in figure 6.9(*bottom, left*) provide a clear method of separating Halo photons from true photons from collision.

A distribution of the Halo photon time against the photon  $\phi_\gamma$  shown in figure 6.9(*top, right*) shows that most halo photon are distributed around  $\phi = 0, \pm\pi$  in agreement with our expectation since, the magnetic field in ECAL does not affect the flight path of Halo muons.

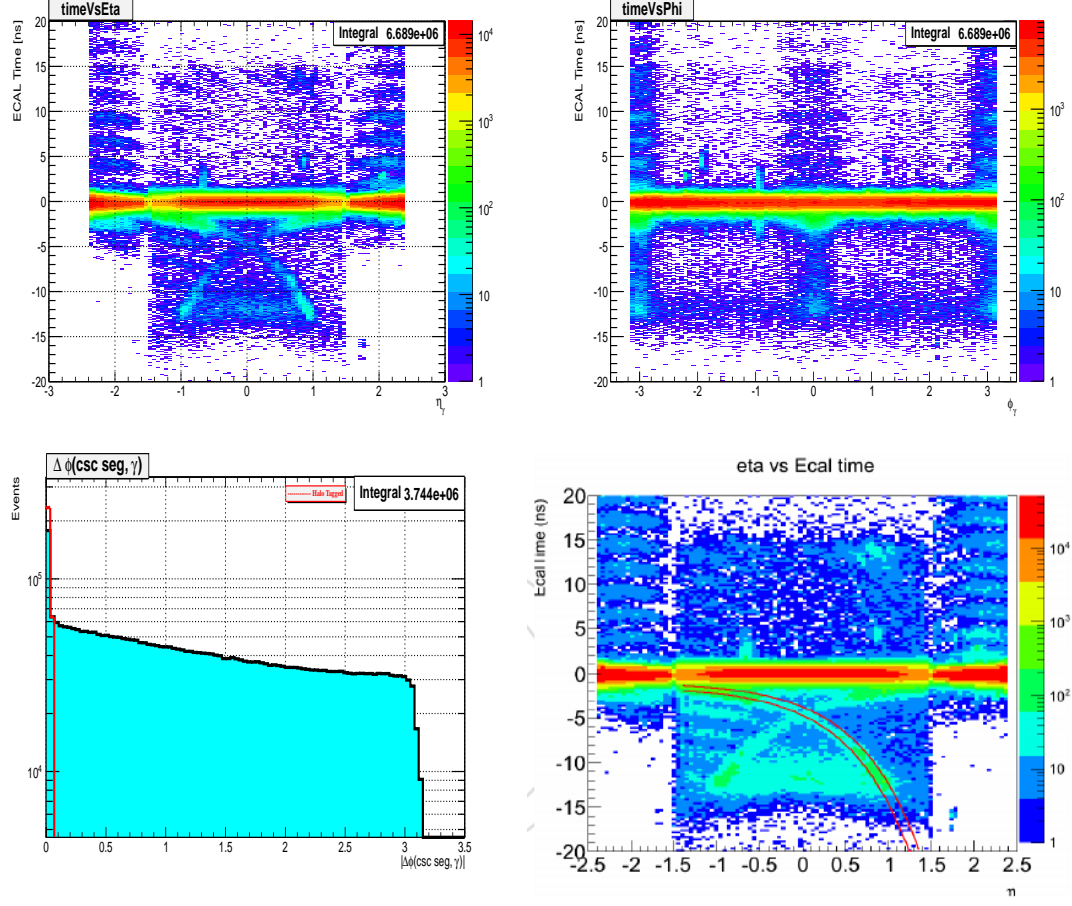


Figure 6.9: ECAL time Vs  $\eta$  (left) and ECAL time Vs  $\phi$  (right) and  $CSC(\text{Seg}, \gamma)\Delta\phi$  for photons with  $p_T > 80$  GeV from data. Halo photons show a clear matched between CSC segments and ECAL cluster in  $\Delta\phi$  with their distribution peaking at  $\phi = 0, \pm\pi$  and also the shape of their expected time.

### Cosmic Photons

Cosmic muons like beam Halo muons with sufficient energy will also bremsstrahlung in the ECAL producing photons referred here as *cosmic photons*. Unlike halo muons, cosmic muons can arrive at ECAL from any direction. Barrel cosmic photons are expected to be produced from cosmic muons with hits in the Drift Tubes (DT) segments. Using the DT hits and their corresponding photon supercluster  $\eta - \phi$  position in ECAL, we can match this hit position in DT segments to ECAL photon superclusters within  $\Delta\eta$  and  $\Delta\phi$ . The two dimensional distribution for  $DT\Delta\eta(DT, \gamma)$  and  $DT\Delta\phi(DT, \gamma)$  for

this matching for events with photon time above,  $t_\gamma > 2$  ns and time below,  $t_\gamma < -3$  ns is shown in figure 6.10. We conclude that events containing photons with small  $\Delta\eta$  and  $\Delta\phi$  to be candidate cosmic photons. Comparing this to  $\Delta\eta$  and  $\Delta\phi$  2-dimensional distributions of photons from a pure cosmic muons sample (data taken when no proton-proton collisions is happening) show these distributions to be very similar as seen in figure 6.10.

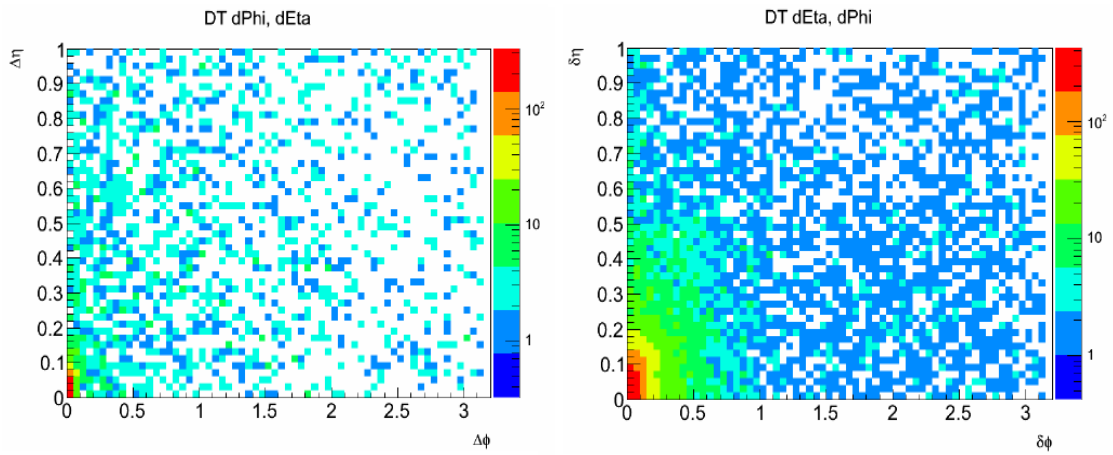


Figure 6.10: 2 dimensional plot showing  $DT\Delta\eta(\text{Seg}, \gamma)$  against  $DT\Delta\phi(\text{Seg}, \gamma)$  for photons with  $p_T > 80$  GeV, ECAL Time,  $t_\gamma > 2$  ns and ECAL Time  $t_\gamma < -3$  ns from proton-proton collision data (left) and pure cosmic muon data (right). Small  $\Delta\eta$  and  $\Delta\phi$  are cosmic photon candidates.

### Anomalous Photons: Spikes

Neutrons and some charge hadrons which deposit their energy directly to the APDs instead of the crystal scintillation are referred to as *anomalous signal* or *spikes*. Spikes can mimic the kinematics of true photons from proton-proton collisions leading to the miss-identification of spikes as true photons. Spikes like true energetic photons can be isolated and so easily pass photon isolation cuts without being identified. A spike supercluster usually consists of very few crystals and most of the time single or double crystals except when embedded in a true photon of high electromagnetic fraction jets where they consist of many crystals and are difficult to identify. However, most spikes show a different signal pulse shape to that of true photons and also have large negative

ECAL time especially at  $t_\gamma \approx -12.0$  ns region. In addition to using energy topological selection cuts, which are based on the spike crystal energy deposits, during ECAL cleaning one can also use the  $\chi^2$  fit value of the timing reconstruction to identify and reject spikes. Spike cleaning is performed during online and offline super cluster reconstruction. However, this online cleaning is not entirely very efficient. Since ECAL clusters belonging to spikes are usually made up of very few crystals compared to photons clusters with many crystals, using the number of crystals in a reconstructed super cluster can be used to distinguish true isolated photons from events with spikes. It has been observed that spike contributions increase with increase in LHC luminosity. Thus, as a selection criteria, photons passing our cosmic photons and halo photons identification and with number of good crystals less than 7 are considered to be spike candidates. Figure 6.11 shows the distribution of the number of crystals in a photon super cluster comparing photons with ECAL time,  $t_\gamma < 0$  ns, in-time photons (ECAL  $-2.0 < t_\gamma < 0$  ns) and selected spike and halo control sample. The spike control sample is selected using the spike energy topological cut “swiss-cross” variable in the region with  $t_\gamma \approx -12.0$  ns where it is observed that spike concentration is high, is used to identify and reject events with spikes during super cluster reconstruction. We observe as shown in figure 6.11(*left*) that most spikes always have fewer(< 7) crystals in their photon supercluster.

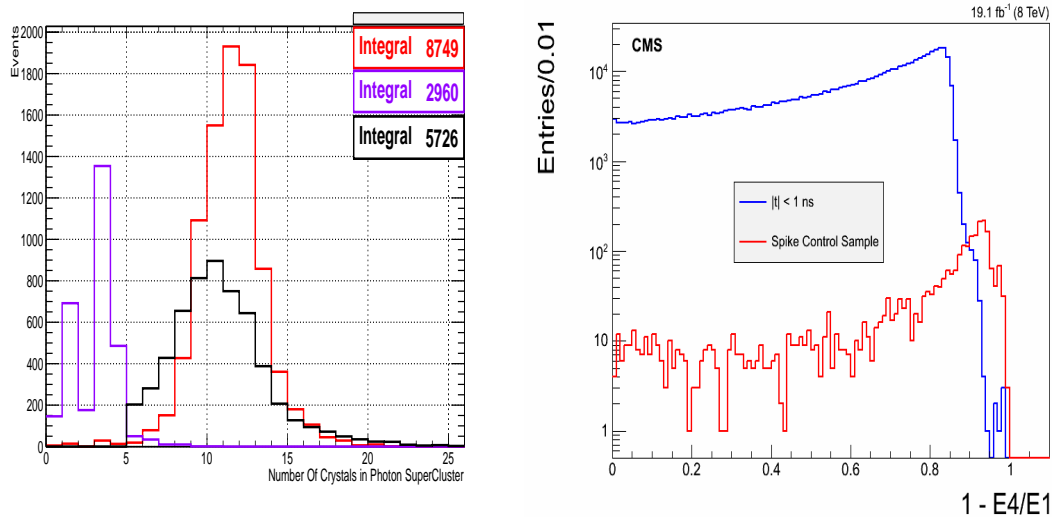


Figure 6.11: Plot showing *number of crystals* in photon supercluster for photons from the region with ECAL Time,  $t_\gamma < 0$  ns. Figure shows the timing distribution of candidate true photons(black), spike candidate photons (magenta) and halo candidate photons (red). The toplogical swiss-cross variable ( $1 - E_4/E_1$ ) distribution is shown comparing true photons ( $|t_\gamma| < 1.0$ ) to spike populated sample.

### 6.3.2 Collision Backgrounds

#### QCD Photons and Pile Up

Collisions from the main proton bunches happening every 50ns during 2012 LHC Run I are not the only collisions that can occur at the LHC. The presence of satellite/ghost bunches spaced in 5.0 ns or 2.5 ns discussed in section 3.1.5 along LHC bunch structure can also collide producing delayed photons either from collisions between these satellite/ghost bunches or with the main proton bunch. As observed in figure 6.6, photons from these events are a serious background source to delayed photons and most of these photons will pass all the above event and photon selection criteria. Thus, it is imperative to estimate delayed photon contributions from satellite/ghost bunches is it is not negligible. Since these background source is non-reducible and the kinematics of these events are very similar, we employ the standard ABCD method to for estimating these background contribution to the signal region. However, we only perform this estimation after cleaning for possibly non-collision event contamination.

#### 6.3.3 Event Cleaning, Veto Performance and Fake Rate

Using the derived kinematic variables for halo, cosmic and spike photons, we apply selection cuts on these variables for tagging and rejecting contributions from non-collision events. These cuts are applied in addition to our above event selections cuts to perform the following event cleaning:

- Veto 0-jet events as this sample is highly populated with beam halo events,
- Veto events with  $CSC\Delta\phi(Seg, \gamma) < 0.05$ ,
- Veto events with  $\Delta\eta(DTSeg, \gamma) < 0.1$  and  $\Delta\phi(DTSeg, \gamma) < 0.1$  .
- Only photons with  $|\eta_\gamma| < 1.45$  are considered,

- Veto events with photons with Number of Good crystals < 7 and  $1 - E_4/E_1 > 0.98$ .
- Remove photons tagged as halo and cosmic photons,
- Veto events with less than 2-jets.

Events which pass all these additional selection criteria make up the sample which is used to estimate our final background to our signal. Since it is very challenging to define pure control samples for each non-collision background source without possible contamination, we estimate the fake rates from the above veto or rejection conditions using in-time ( $|t_\gamma| < 2.0$  ns) photon sample where we believe non-collision contribution is small compared to true photons from collision. Our measured fake rates are shown in table 6.9.

Background Source	Fake Rate(%)
<i>Halo Photons</i>	$\approx 3$
<i>Cosmic Muons</i>	$\approx 1.4$
<i>Spikes</i>	$\approx 0.4$

Table 6.6: Fake rates for different non-collision cleaning.

After performing our event cleaning criteria, tagging and rejection of most of halo, cosmic and spike events, our residual background photon timing distribution is shown in figure 6.12 with the different sources of our background tags. We now perform an ABCD background estimation technique on this residual background to estimate possible contamination of the remaining non-collision background to signal.

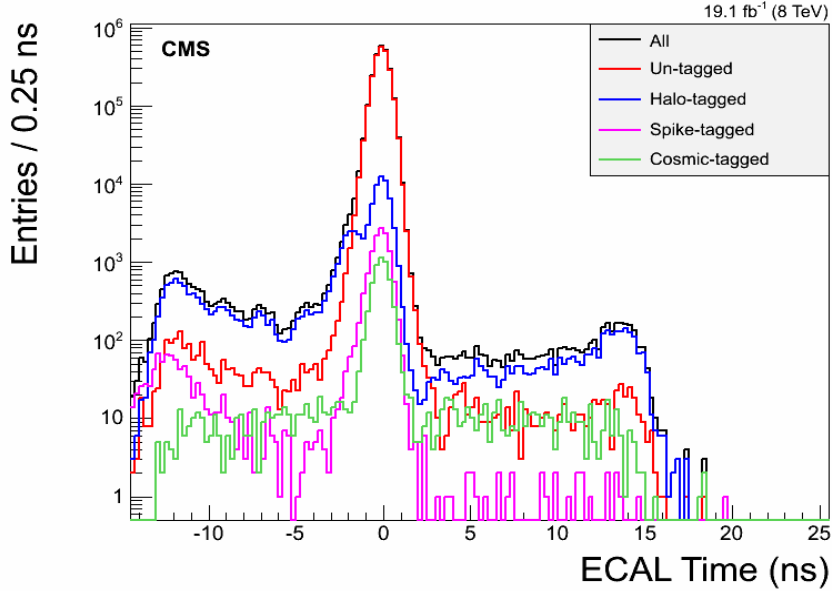


Figure 6.12: Residual Background after tagging the different non-collision background sources using the methods described in text.

### Residual Background Estimation Using ABDC Technique

In order to estimating the background contribution from collision and non-collision sources, we employ a 3-dimensional space involving  $\cancel{E}_T$ ,  $\cancel{E}_T^\gamma$  and photon ECAL time,  $t_\gamma$ . Our signal events are those with  $3.0 < t_\gamma < 13.0$  ns with large  $E_T^{\text{miss}}$ , and by large  $E_T^{\text{miss}}$ , we mean events with  $\cancel{E}_T > 60$  GeV,  $\cancel{E}_T^\gamma > 60$  GeV. Non-collision events as already seen can also have large time, since they are mostly out-of-time and by  $E_T^{\text{miss}}$  calculation and corrections(see discussion above) should have large  $\cancel{E}_T$  and small  $\cancel{E}_T^\gamma$ . Events from collision on the other hand are produced mostly in-time ( $-2.0 < t_\gamma < 2.0$  ns) except in cases of timing mis-measurements or ghost/satellite contributions where  $t_\gamma > 3.0$  ns. Collision events, mostly produced through SM interactions, cannot be produced with large correctly calculated  $E_T^{\text{miss}}$ , e.g.  $\gamma + \text{jets}$  events are produced with very small  $E_T^{\text{miss}}$ , however due to timing mis-measurements, they may appear out-of-time and assigned large  $E_T^{\text{miss}}$ . Thus we conclude that collision events will generally have small  $\cancel{E}_T$  but large  $\cancel{E}_T^\gamma$ .

We select control samples (CS) defined by  $\cancel{E}_T$ ,  $\cancel{E}_T^\gamma$  and  $t_\gamma$  according to the ABCD

technique to estimate our background contributions while remaining vigilant and taking into account the possible contamination to each background source from possible fluctuations in event rate as a result of our selection cuts in defining these CRs. The overall estimation technique is verified through a closure test procedure and the collision background estimation is validated using an extra control sample of  $Z \rightarrow e^+e^-$  events for  $Z$  candidates reconstructed from photon candidates extended to include out-of-time events.

1.  **$\cancel{E}_T > 60 \text{ GeV}$ :** CS in which collision (QCD) background is suppressed while halo, cosmic ray and spike photon is enhanced since most non-collision background photons are produced with high  $p_T$  hence large  $\cancel{E}_T^\gamma$ . Using this CS, we define four regions for estimating the non-collision background contribution using the ABCD recipe.

Non-Collision	$\cancel{E}_T < 60 \text{ GeV}$	$\cancel{E}_T > 60 \text{ GeV}$
$3.0 < t_\gamma < 13.0 \text{ ns.}$	$C$	$D$
$-10.0 < t_\gamma < -3.0 \text{ ns}$	$A$	$B$

Table 6.7: ABCD Control Regions (CRs) for estimating non-collision background.

Thus, the number of events expected in Control Region (CR)  $D$  using table 6.7 with the assumption that  $\frac{N_D}{N_B} = \frac{N_C}{N_A}$  is given as:

$$N_D = \left( \frac{N_B}{N_A} \right) \cdot N_C \quad (6.3)$$

2.  **$\cancel{E}_T > 60 \text{ GeV}$ :** CS where non-collision background (halo, cosmic and spike photons) contribution is suppressed while collision (QCD) background contribution is enhanced. Further dividing this CS and applying  $A' B' C' D'$  method to estimated collision contribution is shown in table 6.8.

Collision	$\cancel{E}_T < 60 \text{ GeV}$	$\cancel{E}_T > 60 \text{ GeV}$
$3.0 < t_\gamma < 13.0 \text{ ns.}$	$C'$	$D'$
$-2.0 < t_\gamma < 2.0 \text{ ns}$	$I'$	$I$
$-10.0 < t_\gamma < -3.0 \text{ ns}$	$A'$	$B'$

Table 6.8:  $A' B' C' D'$  and  $I I'$  CRs for estimating collision background.

Using CRs defined in table 6.8, we can estimate the contributions of collision background in both CRs  $B$  and  $D$  of our non-collision background CS as follows:

$$N_B^{col} = N_{B'} = \left( \frac{I}{I'} \right) \cdot N_{A'}, \quad N_D^{col} = N_{D'} = \left( \frac{I}{I'} \right) \cdot N_{C'} \quad (6.4)$$

where we have assumed that  $\frac{N_{B'}}{N_{A'}} = \frac{N_I}{N_{I'}}$  and  $\frac{N_{D'}}{N_{C'}} = \frac{N_I}{N_{I'}}$ .

$N_B^{col}$  and  $N_D^{col}$  are collision contributions to CRs  $B$  and  $A$ . The final combined background estimation is given by equation 6.5.

$$N_D^{Total} = \left( \frac{N_B - N_B^{col}}{N_A} \right) \cdot N_C + N_D^{col} \quad (6.5)$$

where  $N_D^{Total} = N_D^{non-col} + N_D^{col}$  is the total background estimation in our signal region.

### Closure Test

Selecting events with 0-jets and 1-jet, we performed closure test of our background estimation method. We also perform a cross-check on the assumptions used in our background estimations for small contributions for collision background using  $Z \rightarrow e^+e^-$  events. Our underlying assumption here is that background contributions to large timing from collision source referred here as QCD is very small and must be of the order of  $10^{-5}$  in comparison to in-time photons. i.e the ratio  $N_{|t_\gamma|>3\text{ ns}}/N_{|t_\gamma|<2.0\text{ ns}} \approx 10^{-5}$  with  $N$  being the number of photons. The closure test compares the number of events observed in CR  $D$  to the number expected using our ABCD background estimation method in the same CR  $D$ . We observed 10 events while from using equation 6.5, we expected  $16.78^{+2.95}_{-3.45}$ . We argue that within our statistical uncertainties, there is quite an agreement between our expectation and observed events. The complete result from our closure test is shown in table 6.9. This gives us confidence that our background estimation method is robust and reliable. We apply the same ABCD to estimate the background contribution in our signal sample. Our signal sample consist of events with at least 2-jets, at least a single photon and  $\cancel{E}_T > 60\text{ GeV}$ ,  $\cancel{E}_T > 60\text{ GeV..}$

Non-Collision	$E_T < 60 \text{ GeV}$	$E_T > 60 \text{ GeV}$
$3.0 < t_\gamma < 13.0 \text{ ns}$	C(405)	D(10) <b>16.78</b>
$-10.0 < t_\gamma < -3.0 \text{ ns}$	A(871)	B(36)
Collision	$E_T < 60 \text{ GeV}$	$E_T > 60 \text{ GeV}$
$3.0 < t_\gamma < 13.0 \text{ ns}$	$D'(4)$	D(10)
$-2.0 < t_\gamma < 2.0 \text{ ns}$	$F'(1353685)$	F(34543)
$-10.0 < t_\gamma < -3.0 \text{ ns}$	$B'(5)$	B(36)

Table 6.9: Result from closure test of background estimation technique using 0 and 1-jet events. Numbers in bracket represent our expected background estimate using ABCD method.

### 6.3.4 Background Estimation Cross Check

The main assumption in our background estimation technique is that, the contribution from collision background events to out-of-time regions ( $3.0 < t_\gamma < 13.0 \text{ ns}$ ) is negligible. In order to show that this assumption is correct, we select  $Z \rightarrow e^+e^-$  events from `SingleElectron` and `DoubleElectron` data sets of 2012. Our motivation is to use a control sample where contributions from non-collision events is very small. We select  $Z$  candidate events from an extended photon sample including out-of-time photon events according to the following selection criteria:

- The candidate two electrons for the  $Z$  bosons must have individual  $p_T > 25 \text{ GeV}$ ,
- The di-mass of these two electrons,  $|m_{e^+e^-} - 91| > 61 \text{ GeV}/c^2$ ,
- Each electron must be in the barrel,  $|\eta_{e^-}| < 1.479$  and  $|\eta_{e^+}| < 1.479$ .

At the electron super cluster level, we used the seed crystal time adjusted to account for the electron time of flight, as the electron time. The seed crystal must satisfy the recommended crystals or rechit cleaning criteria by the ECAL group which include `kWeird`, `kBad`, `kPoorCalib` used for rejecting crystals showing anomalous behavior like spikes, noisy, bad crystals or poorly calibrated crystals. In this cross-check, we define our signal region as  $Z$ -candidate events with a well defined mass from both electrons i.e  $76 < |m_{e^+e^-}| < 100 \text{ GeV}/c^2$  while the non  $Z$  events control sample are events which do not fall into this signal category. A quick look at photon  $t_\gamma$  vs  $\eta_\gamma$  and  $\phi_\gamma$  plots as

previously shown for halo photons in figure 6.9, shows that the electron candidates from the `Single/DoubleElectron` dataset when compared to the `SinglePhoton` dataset in figure 6.13 show no or very little contribution from cosmic, halo and anomalous photon events. This confirms our choice of the  $Z$  candidate events sample as a reliable sample to study collision events as it is free from non-collision events.

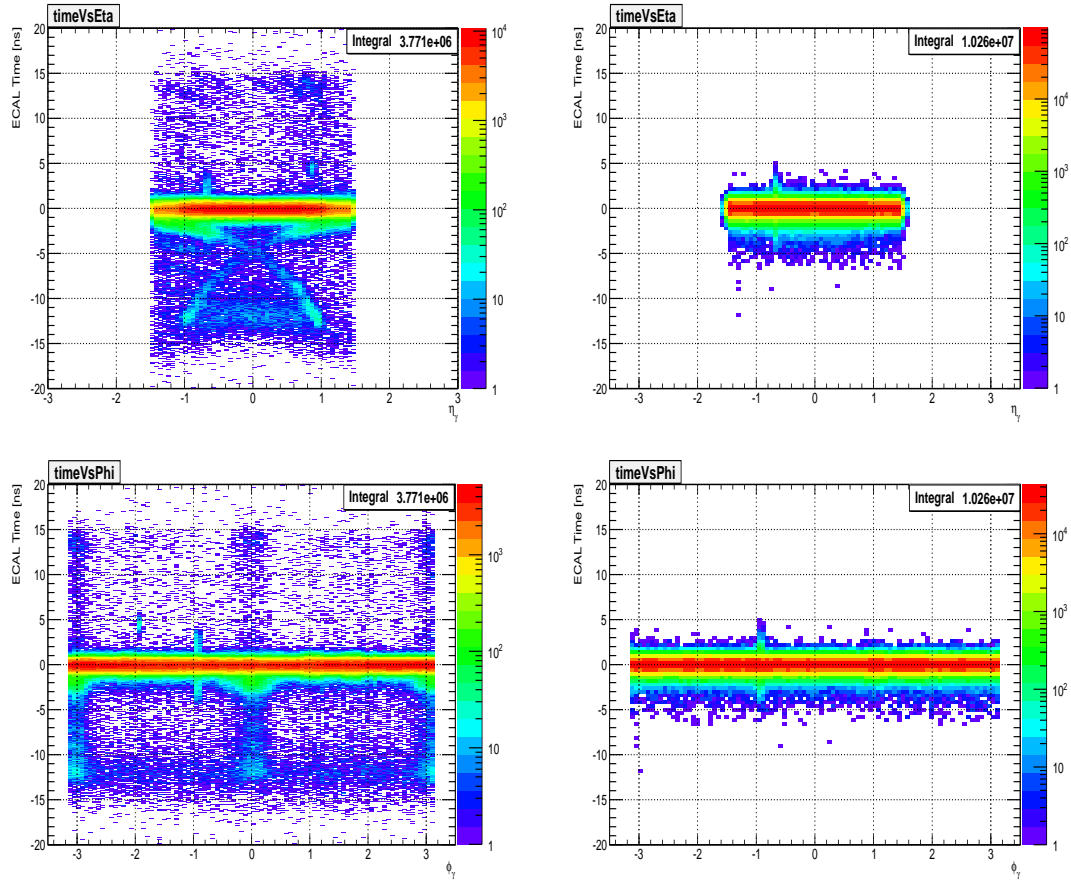


Figure 6.13: ECAL time,  $t_\gamma$  Vs  $\eta_\gamma$ (top) and  $t_\gamma$  Vs  $\phi$  (bottom) for photons from `SinglePhoton` dataset (left) compared to electron candidates from the `DoubleElectron` dataset (right). All photons or electron candidates are in barrel subdetector. Most of the photons with  $\phi = 0, \pm\pi$  are halo photons which are not observed in the  $Z$  boson candidate sample.

Figure 6.14 shows the  $Z$  boson mass reconstructed from the candidate electrons and timing of each electron for Signal (*top and blue*) and for our control sample (*bottom and*

red).

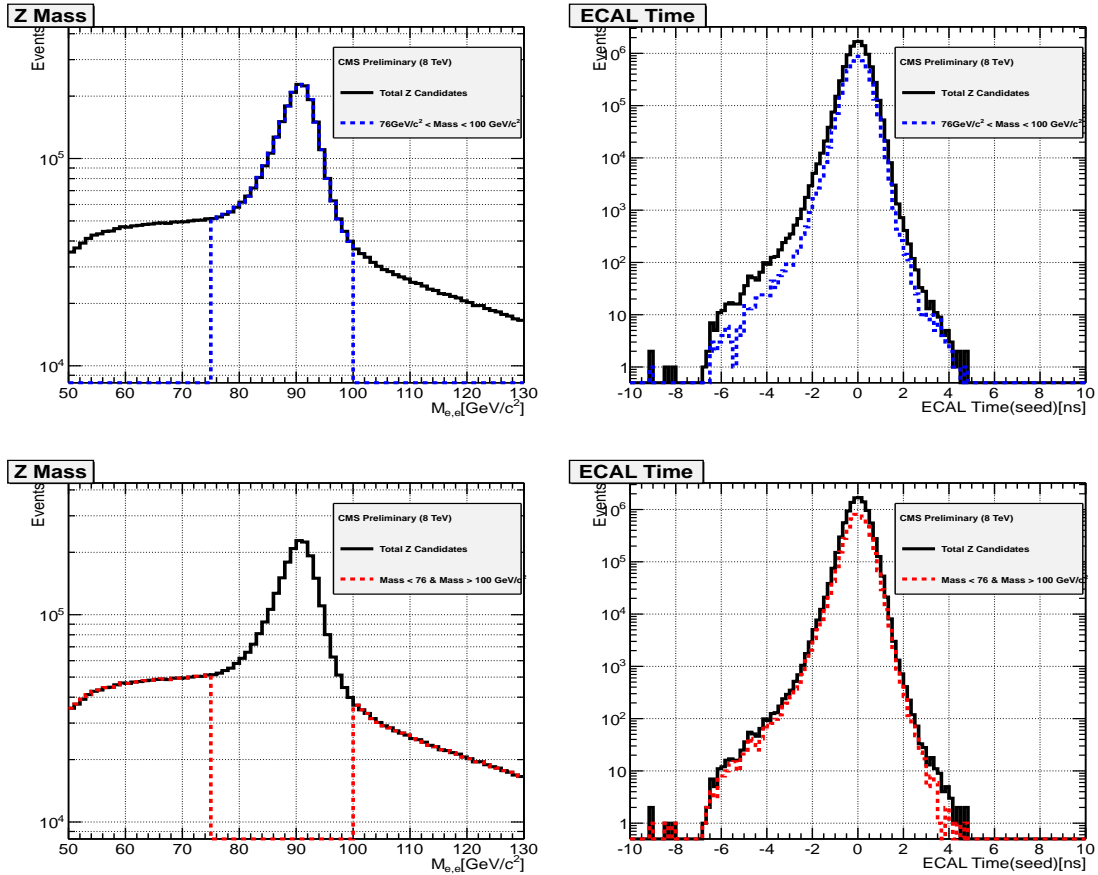


Figure 6.14: Di-electron candidate mass distribution and the time of both electrons for the signal  $76 < m_Z < 100$  GeV/ $c^2$   $Z$  boson sample(left) and similar distributions from the Control ( $50 < m_Z < 76$  GeV/ $c^2$  and  $100 < m_Z < 130$  GeV/ $c^2$ ) sample (right). Candidates events from the DoubleElectron dataset.

Using the background  $Z$  control sample, we estimate its contribution to out-of-time events using a simple scaling methods which can also be understood as an ABCD method. The method is applied as follows:

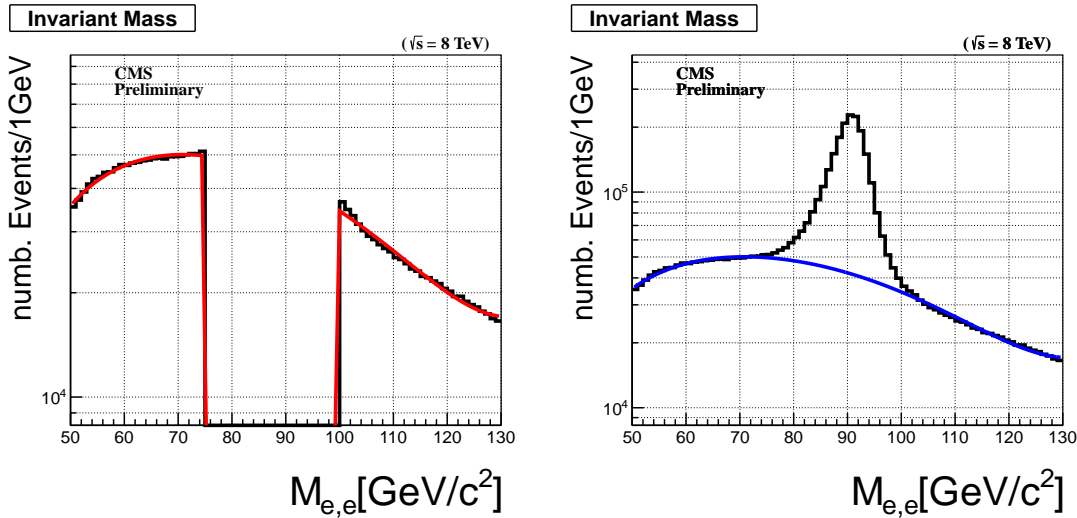
- Using a polynomial function, we fit the di-electron candidate mass distribution of the background control sample to extract a set of fit parameters,

- Using these fit parameters to define our polynomial function, we use this function to extract a scaling factor use to determine the true contribution of the background control region events in the signal region which in this case are  $Z$  bosons with possible large ECAL timing,  $|t| > 3$  ns.
- We scale the background control sample timing distribution (electrons time) using the extracted scale factor. This scale factor is defined as,

$$\text{Scale Factor} = \frac{N}{M_1 + M_2}$$

- By subtracting the scaled background control sample  $Z$  candidates timing distribution from the signal sample  $Z$  candidate timing distribution, we are left with the real  $Z$  boson events whose electron time can fluctuate into larger timing region.
- Comparing the total number of observe electron candidates with  $t > 3$  ns to those in-time,  $|t| < 2$  ns, their ratio i.e  $N_{t>3\text{ ns}}/N_{|t|<2.0\text{ ns}}$  gives us an estimate of the possible genuine electromagnetic objects from collision with large ECAL timing.

A simple picture showing the above procedure with distributions is shown in figure 6.15.



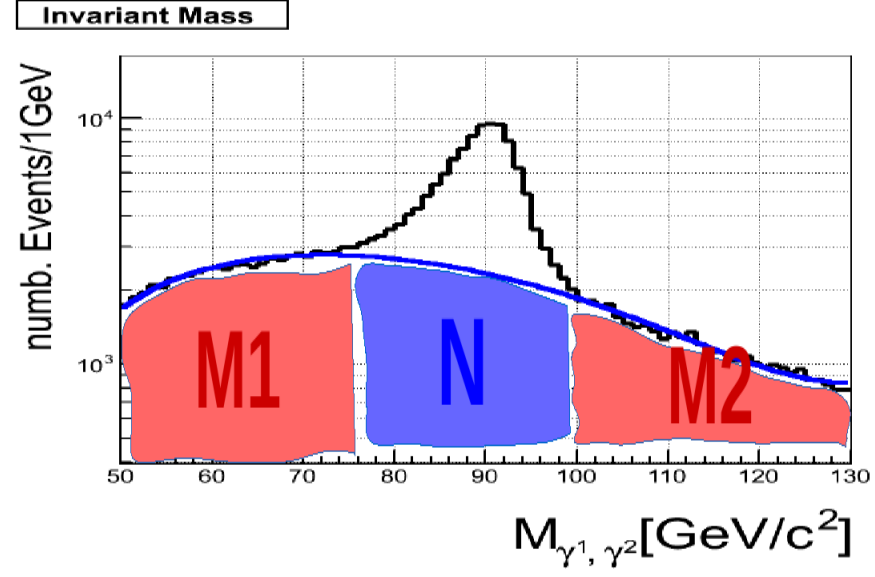


Figure 6.15: *Top:* Control sample (left) and signal sample (right) of di-electron candidate mass distribution. *Bottom:* Figure showing definition of scale factor use in estimating the contributions from control sample in signal sample.

The result of the final timing distribution for genuine  $Z$  boson events is shown in figure 6.16. It is not difficult to see that the ratio  $N_{t>3 \text{ ns}}/N_{|t|<2.0 \text{ ns}} < 10^{-5}$  confirming that indeed the contribution of electromagnetic objects with large timing  $t > 3$  ns is negligible and in agreement with our assumption that most collision events contain photons which are mostly in-time,  $|t| \leq 2$  ns. Its important to note that, we have not applied any  $E_T^{\text{miss}}$  selection cuts here. A simple cut,  $E_T^{\text{miss}} > 60 \text{ GeV}$  could further reduce this ratio to an even smaller number as assumed in our above background estimation.

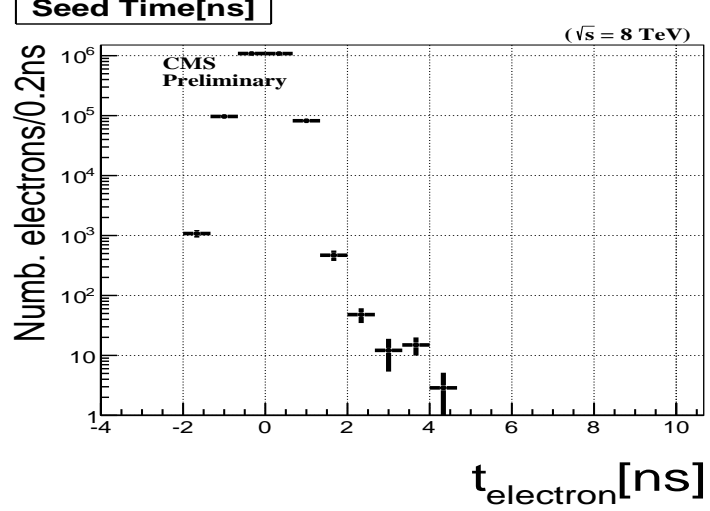


Figure 6.16: Timing distribution of genuine  $Z$  bosons after background contribution has been subtracted.

## 6.4 Results

Finally, we perform our background estimation on signal samples which are events with at least 2 jets, at least one high  $p_T > 80 \text{ GeV}/c$  isolated photon with ECAL time  $3.0 < t_\gamma < 13.0 \text{ ns}$  or  $-10.0 < t_\gamma < -3.0 \text{ ns}$  and  $E_T^\gamma > 60 \text{ GeV}$ ,  $E_T > 60 \text{ GeV}$ .

We observed 1 event and expected  $0.0888^{+0.1869}_{-0.0444}$  background events within our statistical uncertainties. Our complete result is shown in table 6.10 and in table 6.11, we show the number of GMSB SPS8 signal events passing our final selection for  $\Lambda = 180 \text{ TeV}$  with different  $c\tau$  values of the neutralino.

Non-Collision	$E_T < 60 \text{ GeV}$	$E_T > 60 \text{ GeV}$
$3.0 < t_\gamma < 13.0 \text{ ns}$	$C(0)$	$D(1)$
$-10.0 < t_\gamma < -3.0 \text{ ns}$	$A(5)$	$B(1)$
Collision	$E_T < 60 \text{ GeV}$	$E_T > 60 \text{ GeV}$
$3.0 < t_\gamma < 13.0 \text{ ns}$	$D'(5)$	$D \ 0.0888^{+0.1869}_{-0.0444}$
$-2.0 < t_\gamma < 2.0 \text{ ns}$	$F'(657663)$	$F(30242)$
$-10.0 < t_\gamma < -3.0 \text{ ns}$	$B'(1)$	$B \ 0.23^{+0.092}_{-0.118}$

Table 6.10: Result of observed events and estimated background from signal sample, events with at least 2-jets. Numbers in bracket represent our observed number of events while numbers not in bracket are our expected number of background events estimated using ABCD method.

<b>SPS8 GMSB Signal</b>	<b>Number of Events</b>
GMSB(SPS8) ( $\Lambda = 180 \text{ TeV}, c\tau = 250 \text{ mm}$ )	0.2096
GMSB(SPS8) ( $\Lambda = 180 \text{ TeV}, c\tau = 500 \text{ mm}$ )	4.5423
GMSB(SPS8) ( $\Lambda = 180 \text{ TeV}, c\tau = 1000 \text{ mm}$ )	6.3646
GMSB(SPS8) ( $\Lambda = 180 \text{ TeV}, c\tau = 2000 \text{ mm}$ )	6.3968
GMSB(SPS8) ( $\Lambda = 180 \text{ TeV}, c\tau = 4000 \text{ mm}$ )	6.1442
GMSB(SPS8) ( $\Lambda = 180 \text{ TeV}, c\tau = 6000 \text{ mm}$ )	4.6498
GMSB(SPS8) ( $\Lambda = 180 \text{ TeV}, c\tau = 12000 \text{ mm}$ )	2.918

Table 6.11: Final number for  $\Lambda = 180 \text{ TeV}$  GMSB SPS8 MC signal events passing our selection cuts.

## 6.5 Systematic Studies

The different sources of systematic which affect this analysis and the estimated contribution of each identified source of systematic is shown in table 6.12. These systematic is also used in the calculation of the upper limit on observed signal cross-section. We obtained these systematic percentage by varying each individual source and see how that affects the number of events passing our selection cuts. The systematic uncertainty on luminosity measurement has the recommended value of 2.2% provided by CMS and LHC luminosity measurements. The uncertainty for the jet energy corrections (JEC) and jet energy scale (JES) has also been measured using the standard CMSSW tool by [52] and provided by the CMS JEMET working group. The uncertainty on the photon energy scale in barrel was estimated to be 1.0% and based on the final-state radiation (FSR) in  $Z \rightarrow \mu\mu\gamma$  events [53]. The uncertainty from parton density functions (PDF) evaluated using the re-weighting technique using the Master Equation of CTEQ65 model set described in [54]. The uncertainty on the  $E_T^{\text{miss}}$  resolution uses a conservative estimate from [55]. The uncertainty on the ECAL timing obtained by comparing the peak in the timing distribution between  $\gamma +$  jet sample and data events with time  $|t| < 2 \text{ ns}$  is found

to be of the order of 200 ps per event and from a study of high  $p_T$  photons beyond gain transitions has agreed by ECAL DPG to be a conservative estimate. Another important source of systematic is in the selection of the background control samples and our background estimation and individual systematic in the tagging and miss-tagging of non-collision background and estimating background contributions from collisions. We combined these separate systematic contributions into a single background estimation systematic referred here as our background estimation systematic. This is our largest source of uncertainty in our analysis which we estimate to vary from 50% to 200%.

<b>Source</b>	<b>Uncertainty on <math>\sigma_{UL}^{Exp}(\%)</math></b>
Photon energy scale (1.0%)	< 3.0%
Jet energy scale	< 0.05%
Jet energy resolution (10%)	< 1.90%
PDF uncertainty (10%)	< 1.70%
$E_T^{\text{miss}}$ resolution (10%)	< 2.8%
ECAL time uncertainty (0.5 ns)	< 5.0%
Background estimation uncertainty (50.0)	< 51.0%
Luminosity (4.5%)	< 2.2%

Table 6.12: Summary of systematic uncertainties used in this analysis and applied to our cross-section upper limit,  $\sigma_{UL}$  calculation.

## Chapter 7

# Statistical Analysis

### 7.1 Limit Computation

The upper limit calculation procedure used in this analysis is the CLs technique. We fed carefully estimated amounts of background and signal with systematic to obtain the limit. The variable for which the 95% upper limit is set unlike previous experiments is based entirely on the neutralino proper decay length,  $c\tau_{\tilde{\chi}_1^0}$ .

The method we used in our upper limit calculation is by first performing a Hypothesis test and then use the result of this test to derived our confidence intervals. We do the following:

- We define a NULL hypothesis ( $H_0$ ) and the Alternate hypothesis ( $H_1$ ). If we had several other hypothesis, we will defined them also.
- Select a Test statistics ( $t(x)$ ), where  $x$  is the data.
- Select a corresponding test statistics calculator.
- Use the result of the hypothesis test to compute the interval by inverting the result of the hypothesis test.

First, we describe the acceptable technique in experimental high energy physics for computing *p-values* used in any search and discovery experiment.

### 7.1.1 CLs Technique

The  $CL_s$  technique [59] is attributed as the standard technique or framework for computing the confidence or exclusion intervals in a search and discovery experiment. It has been shown to work during the search for the Higgs boson at LEP and recently in the discovery of the scalar boson in 2012, by both CMS and ATLAS experiments with the mass of this boson being:  $m_H = 125.36 \pm 0.37(\text{stat.Unc}) \pm 0.18(\text{syst.Unc})$ .

This method has been implemented in a unique statistical software package called *HiggsCombine* with the goal of providing direct access to a variety of robust statistical methods with optimised performance for computing limits or confidence intervals. *HiggsCombine* [61] is the official standard tool recommended by the CMS statistical committee and CMS Higgs group for calculating limits in any CMS search and discovery analysis. It takes as input estimates on the number or distribution of signal and background and the observed number or distribution from data and produces an upper limit in the production cross section of a given physics process for a given value of a parameter of interest (POI). *Higgscombine* tool has the advantage in that, it allows for the possibility to use several different statistical methods of calculating the upper limit. This way, one can make comparison and simple checks for any inconsistency. In this analysis, we used an Asymptotic [62] and HybridNew (a hybrid of Frequentist and Bayesian methods),[61], to calculate our observed upper limits. The purpose of the using the  $CL_s$  method is to compute reliable upper limits in a search scenario when the observed signal is very small compared to the background. In the  $CL_s$  technique, one uses not the p-value ( $CL_{s+b}$ ) but rather divide this by  $CL_b$  (which is 1 minus the p-value for background only hypothesis). The reason for this is to define a conditional probability conditioned to the scenario of observing only background or background only hypothesis. The  $CL_s$  is formally defined as:

$$CL_s = \frac{CL_{s+b}}{CL_b} = \frac{p_{s+b}}{1 - p_b} \quad (7.1)$$

where  $s + b$  means signal and background.

### 7.1.2 Statistical Test Formalism

The Neyman-Pearson Theorem states that the likelihood ratio gives the most powerful hypothesis test. Therefore, we construct our test statistics  $t_\mu$  as a function of the observed data, as a likelihood ratio. In a search analysis, one defines the null hypothesis  $H_0$  describing only known processes, or the background only which is to be tested against an alternate hypothesis  $H_1$  defined as a background and signal. However in the computation of upper limits:

- $H_0$  being the NULL hypothesis includes the background and signal ( $s + b$ ) while
- $H_1$  being the ALTERNATE hypothesis includes only the background ( $b$ ).

Using these, two hypothesis we quantify the level of agreement between our observed data with either of the hypothesis by computing a  $p$ -value ( $p$ -value if the probability under the assumption of a given hypothesis, of finding data of equal or greater incompatibility with the predictions of the given hypothesis). A given hypothesis is then regarded as being excluded if its  $p$ -value is observed below a given threshold. In particle physics, this threshold value for the  $p$ -value is 0.05 corresponding to 95% of confidence level (CL). The CMS accepted method of computing upper upper limit is based on mix of frequentist-hybrid significance test using the profilelikelihood ratio as a test statistics (HybridNew method). The parameter of interests in in our case the rate (cross section) of signal process as well as *nuissance parameters* as systematics for the background and signal models. This parametrized systematics effects results, as is always the case, to loss in sensitivity.

In this search experiment, for each event in the signal, we measured the timing of the photon as our observable. We use this value to construct a histogram  $\mathbf{n} = (n_1, \dots, n_N)$ . The expectation value for each value of  $n_i$  can be written as:

$$E[n_i] = \mu s_i + b_i \quad (7.2)$$

where  $\mu$  is the parameter which determines the signal strength, when  $\mu = 0$  means background-only and when  $\mu = 1$  then we have the signal and background hypothesis.

The the mean number of entries in the  $i$ th bin from signal and background are given as:

$$s_i = s_{tot} \int_{bin,i} f_s(t; \theta_s) \quad b_i = b_{tot} \int_{bin,i} f_b(t; \theta_b) \quad (7.3)$$

with the functions  $f_s(t; \theta_s)$  and  $f_b(t; \theta_b)$  being the probability density functions (Pdfs) of the variable  $t$  for the signal and background events and  $\theta_s$  and  $\theta_b$  representing the parameters which characterise the shapes of the pdfs.  $s_{tot}$  and  $b_{tot}$  represents the total mean numbers of signals and backgrounds while the integrals represent the probabilities for an event to be found in bin  $i$ .  $\theta = (\theta_s, \theta_b, b_{tot})$  denote all nuisance parameters (systematic uncertainties) while  $s_{tot}$  is the signal normalization is fixed to the value predicted by the nominal signal model.

The likelihood function is the product of the Poisson probabilities for all bins:

$$\mathcal{L}(\mu, \theta) = \prod_{r=1}^N \frac{(\mu s_r + b_r)^{n_r}}{n_r!} e^{-(\mu s_r + b_r)} \cdot \mathcal{G}(\theta) \quad (7.4)$$

where  $\mathcal{G}(\theta)$  is a discrete (Poisson) distribution of the nuisance parameters. This distribution can be different for different nuisance parameter.

Using the likelihood function, the profilelikelihood ratio is then defined as:

$$\lambda(\mu) = \frac{\mathcal{L}(\mu, \hat{\theta})}{\mathcal{L}(\hat{\mu}, \hat{\theta})} \quad (7.5)$$

Here  $\hat{\theta}$  is the the value of  $\theta$  that maximizes  $\mathcal{L}$  for a specified  $\mu$ , thus, it is referred to as the *conditional maximum-likelihood estimator* (CMLE) of  $\theta$  (given as a function of  $\mu$ ). While  $\mathcal{L}(\hat{\mu}, \hat{\theta})$  is the maximized (unconditional) likelihood function with  $\hat{\mu}$  and  $\hat{\theta}$  being its *maximum likelihood* (ML) estimators. The nuisance parameters broadens the profilelikelihood as a function of  $\mu$  relative to what is expected if their values where fixed and this reflects in the loss of sensitivity or information about  $\mu$  due to the systematic uncertainties.

### 7.1.3 Test Statistics and $p$ -values

The above expression for  $\lambda(\mu)$  shows that  $0 \leq \lambda \leq 1$ , where  $\lambda$  close to 1 indicates a very good agreement between the data and hypothesis value of  $\mu$ . The test statistics to be used for our statistical test is defined as:

$$t_\mu = -2 \ln \lambda(\mu) \quad (7.6)$$

It is important to note that the test statistics approach to any statistical test is favourable because just by looking at the values of the test statistics, higher values corresponds to increasing incompatibility between the data and the value of  $\mu$  which is from the signal hypothesis. This incompatibility or disagreement between the data and a given hypothesis is quantified by calculating the probability or  $p$ -value as:

$$CL_{s+b} = p_u = \int_{t_{\mu,obs}}^{\infty} f(t_\mu|\mu) dt_\mu \quad (7.7)$$

where,  $t_{\mu,obs}$  is the value of the test statistics  $t_\mu$  obtained from the data and  $f(t_\mu|\mu)$  is a pdf constructed from  $t_\mu$  depending on the signal strength  $\mu$ . The set of values for  $\mu$  that are rejected because their  $p$ -value is below a specified threshold value  $\alpha$  lying on either sides of those not rejected gives a two sided confidence interval of  $\mu$  and if just on one side of the ones not rejected gives an upper limit on the rejected values of  $\mu$ .

In the background only scenario i.e  $\mu = 0$ , the test statistics is defined as:

$$q_\mu = \begin{cases} -2 \ln \lambda(0), & \hat{\mu} \geq 0 \\ 0, & \hat{\mu} \leq 0 \end{cases}$$

where  $\lambda(0)$  is the profilelikelihood ratio for  $\mu = 0$  defined in 7.5. and again to quantify the disagreement between the background-only hypothesis ( $\mu = 0$ ) and the data is given by the  $p$ -value as:

$$CL_b = p_0 = \int_{q_{0,obs}}^{\infty} f(q_0|0) dq_0 \quad (7.8)$$

where  $f(q_0|0)$  denotes the pdf if the test statistics  $q_0$  under the background-only ( $\mu = 0$ ) hypothesis. Figure 7.1 shows a sampling distributions of the test statistics and how the

*p*-values can be extracted from these distributions.

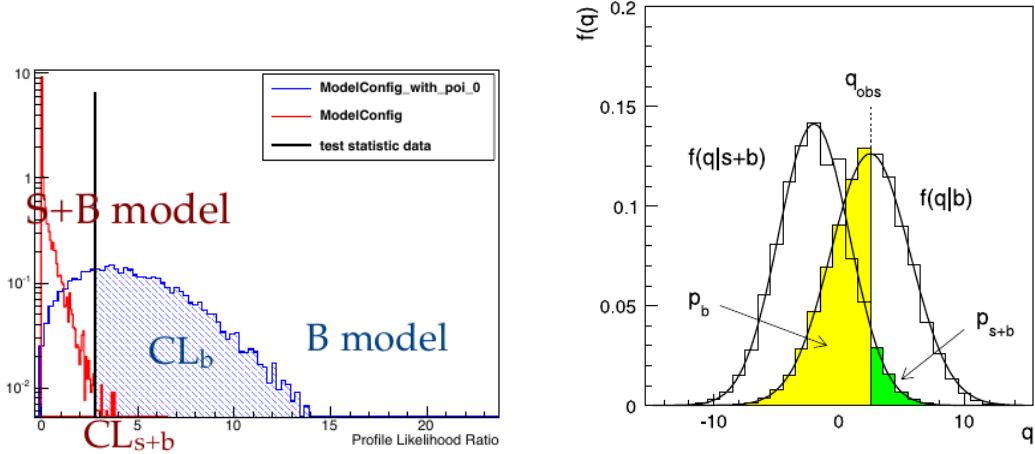


Figure 7.1: Sampling distributions for  $f(t_\mu|\mu)$  showing how one extracts the  $p$ -values. left: is the using a analytic of the Asymptotic method and right: is from the HybridNew method.

In addition to the  $p$ -value, for expressing the disagreement between the data and a given hypothesis, the Higgscombine tool also provides a quantity known as the *significance* ( $\mathcal{Z}$ ).  $\mathcal{Z}$  and the  $p$ -value have a very non-linear relation. Once can defined that relation using a two-sided fluctuation if a Gaussian variable  $\sigma$ , with  $5\sigma$  significance corresponding to a  $p$ -value of  $p = 5.7 \times 10^{-7}$  to denote a discovery. Since, we have not observed any significant excess of events over our standard model background, we will not mention a lot about significance in this thesis, but rather talk about  $p$ -values as they are indispensable in computing limits.

The important question is always, how does one obtain an expression or a distribution of the test statistics and  $f(t_\mu|\mu)$  from the likelihood function? To answer this question, the HiggsCombine tool was developed which consist of various ways of both analytically (e.g the Asymptotic statistical method [62]) or through numerical integration or Monte Carlo computation ( e.g the HybridNew statistical method) obtain the test statistics and  $f(t_\mu|\mu)$ . We have shown the limit computation results of both methods as used in this analysis. As an example, the pdf  $f(q_\mu|\mu)$  of the test statistics ( $q_\mu$ )

obtained through the **Asymptotic** statistical method as given in [62] is:

$$f(t_\mu|\mu') = \Phi\left(\frac{\mu - \mu'}{\sigma}\right)\delta(t_\mu) + \frac{1}{2}\frac{1}{\sqrt{2\pi}}\frac{1}{t_\mu} \exp\left[-\frac{1}{2}\left(\sqrt{t_\mu} - \frac{\mu - \mu'}{\sigma}\right)^2\right] \quad (7.9)$$

where result to a half-chi-square distribution when  $\mu = \mu'$ .

In subtle point worth mentioning is that in the HybridNew approach, systematics uncertainties are taken into account through the Bayesian prior density  $\pi(\theta)$ , and the distribution of the test statistics is computed under the assumption if the Bayesian model of average given as:

$$f(q) = \int f(q|\theta)\pi(\theta)d\theta$$

and the prior pdf  $\pi(\theta)$  is obtained from some measurements characterised by a given likelihood function  $\mathcal{L}_\theta(\theta)$  which is then used to find the prior using Bayes' Theorem. Unlike other cases where systematic uncertainties are taking as being part of the data and incorporated directly through  $\mathcal{G}(\theta)$  as shown in equation 7.4. Nevertheless, they arrive at the same result.

In summary, the hypothesis test is performed using a given statistical method on each value of a chosen parameter of interest (POI)(usually denoted  $\mu$ ). The  $p$ -value if obtained from the sampling distribution of the test statistics being used. Can either obtain this test statistics analytically or through Monte Carlo computation and numerical integration. By plotting the p-value as a function of the POI, we obtain the p-value curve (in this case the  $CL_s = \frac{CL_{s+b}}{CL_b}$ ). The value of  $\mu$  which has a p-value  $\alpha$  ( e.g 0.05) is the upper limit (for 1-dimensional limits, 2-dimensional limits gives lower and upper limits) of  $1 - \alpha$  confidence interval (e.g 95%).

## combined result

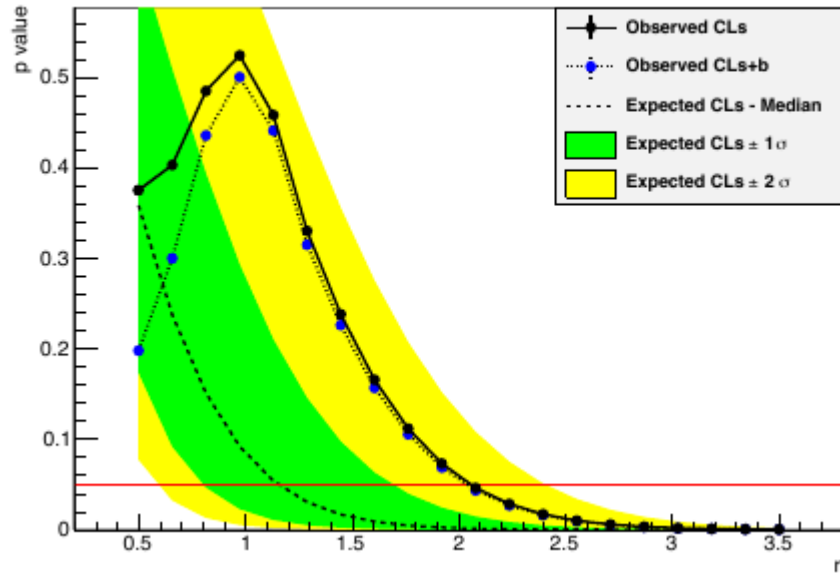


Figure 7.2: Distribution of  $p$ -values showing how upper limit on  $\mu$  is extracted for a given threshold probability.

# Chapter 8

## Limit Interpretation

Using the  $CL_s$  technique, the HiggsCombine tool produces an upper limit along with the expected limit at different quantiles as the signal strength computed which is a ratio of Number of Signal events over the Number of Expected signal events i.e

$$r = \frac{N^{Obs}}{N_{expect}} \quad (8.1)$$

and using the equation as given in chapter 3 on the cross-section  $\sigma = \frac{N}{\varepsilon \cdot A \cdot \mathcal{L}}$  and hence the observed cross-section upper limit is given as:

$$\sigma_{UL}^{Obs} = \frac{r \cdot N^{expect}}{\varepsilon \cdot A \cdot \mathcal{L}} \quad (8.2)$$

where  $\mathcal{L}$  is the integrated luminosity ( $19 \text{ fb}^{-1}$ ) and  $\varepsilon$  and  $A$  are the signal selection efficiency and Acceptance respectively. In addition to the observed limits (Solid black line), the uncertainties on the expected limits at 68%/16% ( $\pm 1\sigma$ ) and at 98%/2.5% ( $\pm 2\sigma$ ) provide the **GREEN** and **YELLOW** respectively, the error from the median (50%) expected limits (dashed red line) shown in figure 8.2.

### 8.1 Signal Efficiency and Acceptance

The efficiency times acceptance ( $\varepsilon \times A$ ) combined as one is seen the figure 8.1.

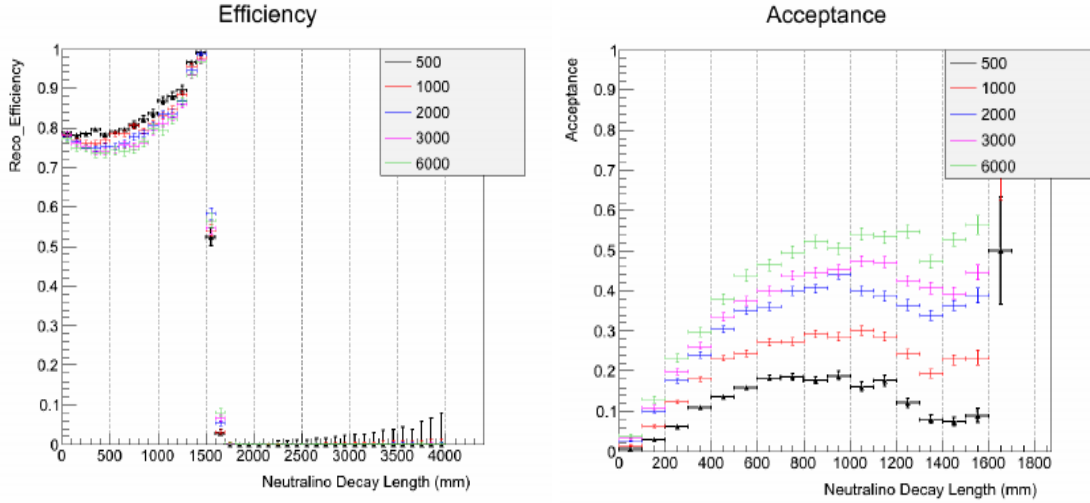


Figure 8.1: The reconstruction and selection efficiency (left)  $\times$  Acceptance ( $t > 3$  ns) (right) against transverse decay length in laboratory frame for different  $c\tau$  points.

The  $\frac{N_{expet}}{\mathcal{L}}$  defines the expected signal cross section which is obtained from a given signal model. In our scenario, our choice of signal model we want to produce exclusion limits on the possible production and decay of a long-lived particle described by this signal model is GMSB. Thus the interpretation of our search analysis is given within the context of any GMSB model with a long-live neutral particle decaying to a photon and gravitino. Such a model is the minimal GMSB or the SPS8 model and the general GMSB model. However, the results provided are based on interpretation within the context of the SPS8 model. In GMSB, the neutralino  $\tilde{\chi}_1^0$  is the NLSP and decays to the gravitino  $\tilde{G}$  the LSP (as a result of R-parity conservation) in association with a very energetic photon  $\gamma$ . Because of the smallness in mass difference between the  $\tilde{\chi}_1^0$  and the  $\tilde{G}$  as well as the coupling, the  $\tilde{\chi}_1^0$  decay to  $\tilde{G}$  is delayed and as a result, the photon emitted can arrive late in the calorimeter crystals. Measuring the arrival time of the photon on ECAL crystals, we can extract important parameters of theory of GMSB.

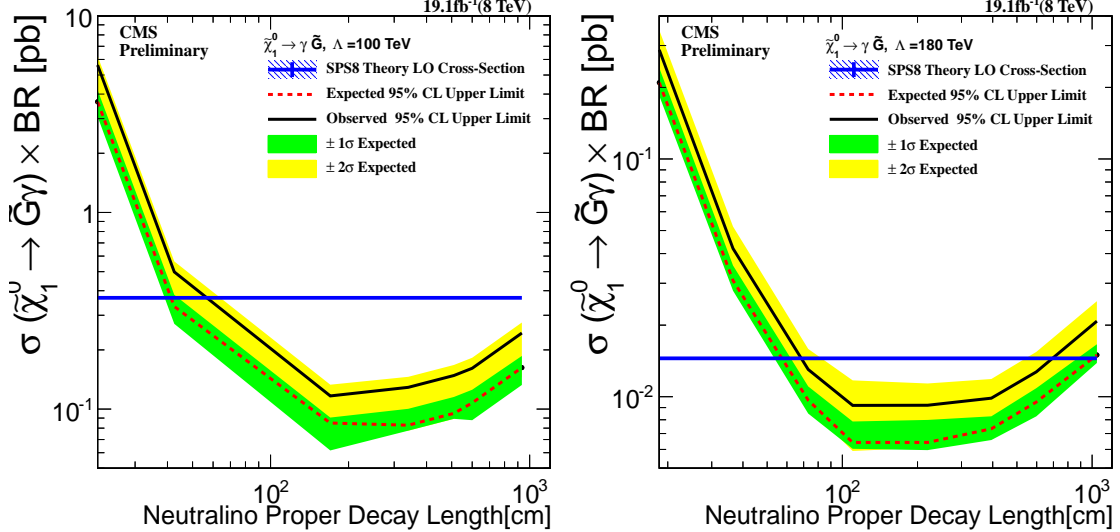


Figure 8.2: Neutralino production cross section against proper delay length upper limit interpretation in SPS8 model. (Left)  $\Lambda = 100$  TeV, (Right)(left)  $\Lambda = 180$  TeV

In the SPS8 model, the parameter space for long-live neutralinos is governed by  $\Lambda_m - c\tau$  2-dimensional parameter space. For each  $\Lambda_m$  point, we have a fixed neutralino mass with different proper lifetimes  $c\tau$ . We have obtained limits for  $\Lambda_m$  ranging from 100 TeV to 180 TeV corresponding to lightest neutralino mass  $m_{\tilde{\chi}_1^0}$  between 90 to 255  $GeV/c^2$  and proper lifetime  $c\tau$  ranging from 250 to 12000 mm corresponding to  $\tau_{\tilde{\chi}_1^0}$  from 0.8 ns to 40 ns.

For a given value of  $\Lambda_m = 180$  TeV, we have a lightest neutralino production cross section times branching ratio plot shown in figure 8.2, showing that the ECAL detector is sensitive to lightest neutralinos of mass  $m_{\tilde{\chi}_1^0} = 255$   $GeV/c^2$  and life time upto 30 ns and we are 95% confident that we have not missed any neutralino whose mass is  $m_{\tilde{\chi}_1^0} = 255$   $GeV/c^2$  and lifetime is  $\tau \leq 30$  ns.

For a given lifetime of  $\tau = 20$  ns, we can also obtain upper limits on the production cross section times branching ratio when compared against their theoretically expected values for a lightest neutralino with mass ranging from  $m_{\tilde{\chi}_1^0} = 90$   $GeV/c^2$  to  $m_{\tilde{\chi}_1^0} = 255$   $GeV/c^2$ . The observed upper limit on this cross section is  $\sigma_{\tilde{\chi}_1^0}^{UP} \geq XX$  pb with proper lifetime of  $\tau = 30$  ns.

Using both the mass and proper lifetime of the lightest neutralino, we present possible

2-dimensional limits simultaneously on  $m_{\tilde{\chi}_1^0}$  or  $\Lambda_m$  and  $c\tau$  or  $\tau$  in the SPS8 model, comparing this with the result of previous experiments. This is shown in figure 8.3.

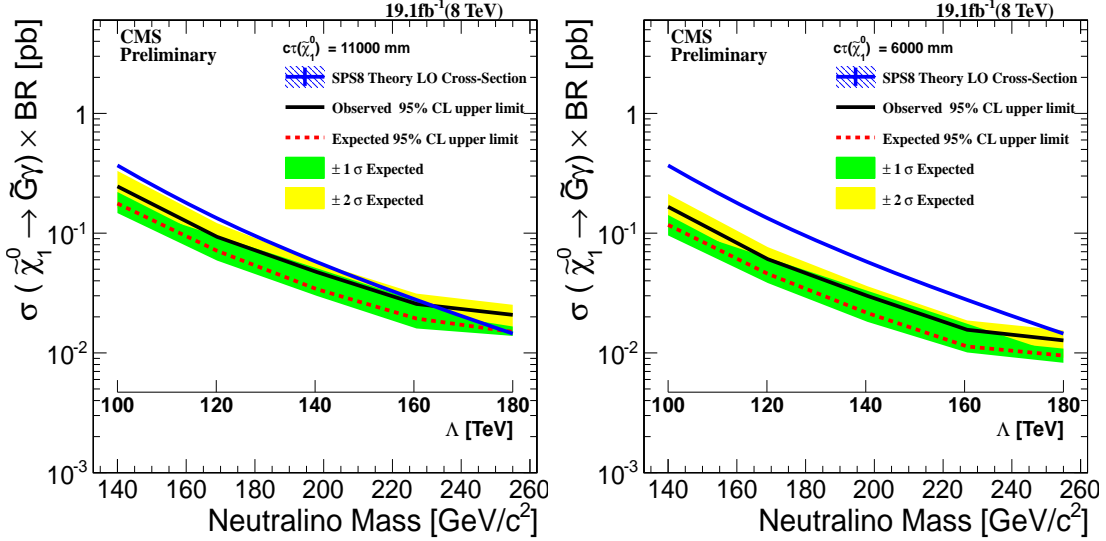


Figure 8.3: Neutralino production cross section against neutralino mass upper limit at 95% confidence levels interpretation in SPS8 model. (Left)  $C\tau = 11000$  mm, (Right)  $C\tau = 6000$  mm

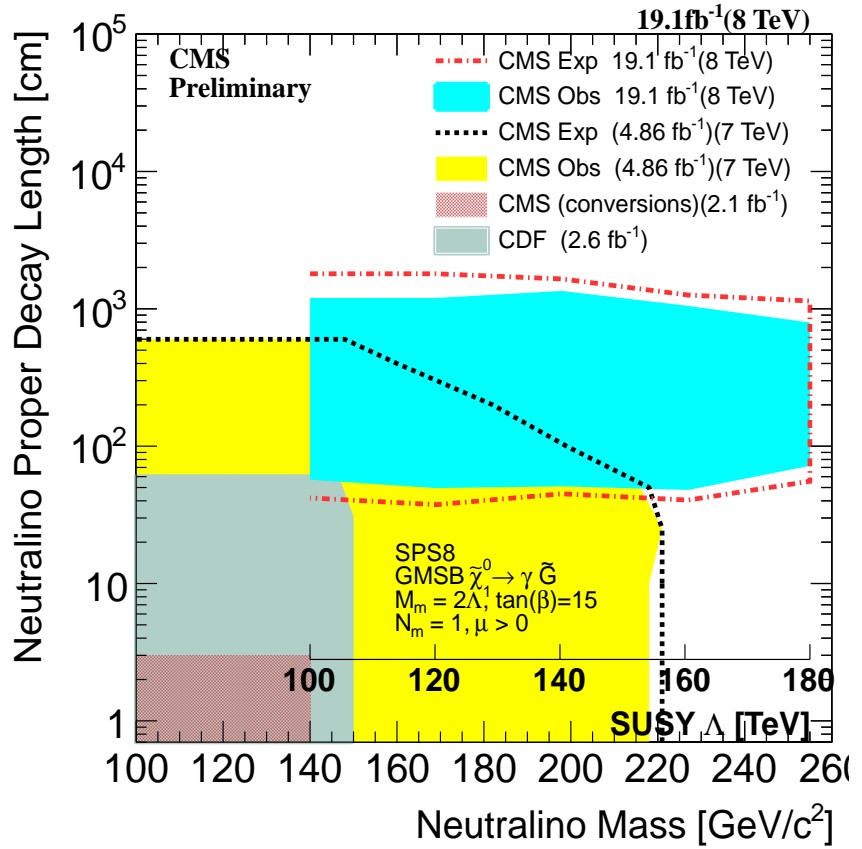


Figure 8.4: Neutralino two dimensional exclusion limit of neutralino mass ( $\Lambda$ ) against proper delay length upper limit interpretation in SPS8 model in the decay  $\tilde{\chi}_1^0 \rightarrow \gamma + \tilde{G}$  with limits from previous experiments shown.

## Chapter 9

# Conclusion

We have performed a search analysis for NMLLP decaying to photons using the time of arrival of the photon as measured by the ECAL sub detector of the CMS detector. Haven fail to find any significant signal of delayed photons over the standard model background, we interpreted our results in SUSY models with NMLLP like SPS8 of minimal GBSM or general GMSB models. We showed that, neutralinos whose production and decay mechanism is described in the SPS8 mGMSB model, with  $m_{\tilde{\chi}_1^0} \leq 235 \text{ GeV}/c^2$  and  $\tau_{\tilde{\chi}_1^0} \leq 35 \text{ ns}$  are ruled out of existence at 95% confidence level using the 2012 8 TeV LHC dataset. This corresponds to an upper limit of  $\sigma_{\tilde{\chi}_1^0}^{UP} \geq 0.02 \text{ pb}$  on the production cross section times branching ratio in a hadron collider. In addition, we mention some of the limitations in this particular analysis from a detector point of view and how in future studies can be improved. We hope that in the future, with increase in center of mass energy of the LHC collider as well as luminosity and an improve in timing resolution beyond what is already very reliable, we will surely find a new fundamental particle whose dynamics cannot be described by the already very successful standard model of particle physics.

# Bibliography

- [1] N. Jarosik et al. (WMAP), *Astrophys. J. Suppl.* **192**, 14 (2011); Overview: K.A. Olive et al.(PDG), *Chin.Phys.C***38**,090001(2014).
- [2] M. Kuhlen, M Vogelsberger, R. Angulo, *Phys.Dark Univ.***1**,50(2012).
- [3] Ellis John, Olive Keith A. (2010). “Supersymmetric Dark Matter Candidates”. arXiv:1001.3651 [astro-ph]
- [4] Laura Covi “Gravitino Dark Matter confronts LHC” *Journal of Physics: Conference Series* 485 (2014) 012002
- [5] J.Ellis, J.Hagelin, D. Nanopoulos, K.A. Olive and M. Srednicki; *Nucl. Phys.* B238 (1984) 453; H. Goldberg, *Phys. Rev. Lett* 50 (1983) 1419; J. Ellis, T. Falk, G. Ganis, K.A. Olive and M. Srednicki, *Phys. Lett. B* 510 (2001) 236, arXiv: hep-ph/0102098.
- [6] B.Allanach et al,arXiv:hep-ph/0202233v1;
- [7] “*Observation of a new boson at a mass of 125 GeV with the CMS experiment at LHC*”, *Phys. Lett. B* 716 (2012) 30-61
- [8] Steven Weinberg, “A Model of Leptons”, *Phys. Rev. Lett.* 19, 12641266 (1967)
- [9] “Observation of a Charged Charmoniumlike Structure in  $e^-e^+ \rightarrow \pi^+\pi^-J/\psi$  at  $\sqrt{S} = 4.26\text{GeV}$ ” M. Ablikim et al. *Phys. Rev. Lett.* 110, 252001 (2013), “Study of  $e^-e^+ \rightarrow \pi^+\pi^-J/\psi$  and Observation of a Charged Charmoniumlike State at Belle”, Z. Q. Liu et al. *Phys. Rev. Lett.* 110, 252002 (2013);

- [10] Peter W. Higgs “Broken symmetries and the masses of gauge bosons”, *Phys.Rev.Lett.* 13.508, 19 October, 1964;
- [11] Haag,Rudolf; Sohnius, Martin; opuszaski, Jan T. “All possible generators of supersymmetries of the S-matrix”, *Nuclear Physics B* 88: 257274 (1975);
- [12] S.Mathin, arXiv:hep-ph/9709356;
- [13] Howard Baer, Xerxes Tata “Weak Scale Supersymmetry: From Superfields to Scattering Events”
- [14] S. Ambrosanio 1 , Graham D. Kribs 2 , and Stephen P. Martin hep-ph/9703211 arXiv:hep-ph/9703211v2.
- [15] G.F. Giudice and R. Rattazzi “ Theories with Gauge-Mediated Supersymmetry Breaking” arXiv:hep-ph/9801271v2
- [16] J.Dann et al.(LEPSUSY Working Group), Internal note LEPSUSYWG/97-04(1997), P. Janot, talk at the EPS Conference, Jerusalem, 1997.
- [17] CDF Collaboration, “Search for Supersymmetry with Gauge-Mediated Breaking in Diphoton Events with Missing Transverse Energy at CDFII “, *Phys. Rev. Lett.*
- [18] ATLAS Collaboration “Search for Diphoton Events with Large Missing Transverse Momentum in  $1 fb^{-1}$  of 7TeV Proton-Proton Collision Data with the ATLAS Detector”, arXiv:1111.4116v1, 17th Nov 2011.
- [19] CMS Draft Analysis, “Search for Long-Lived Particles using Displaced Photons in  $PP$  Collision at  $\sqrt{S} = 7TeV$  ”, CMS AN AN-11-081 104(2010)011801,
- [20] ATLAS Collaboration, J. High Energy Phys. 1212, 124 (2012), arXiv:1210.4457 [hep-ex]
- [21] The LHC Machine, Lyndon Evans and Philip Bryant *Jinst*,
- [22] CMS Collaboration, “CMS Physics: Technical design report, Volume 1” CERN-LHCC-2006-001
- [23] The CERN Brochure 2009-003-Eng

- [24] CMS Collaboration, “The CMS experiment at the CERN LHC”, JINST 0803:S08004, 2008.
- [25] CMS uses a right-handed coordinate system, with the origin at the nominal interaction point, the  $x$ -axis pointing to the center of the LHC, the  $y$ -axis pointing up (perpendicular to the LHC plane), and the  $z$ -axis along the counterclockwise-beam direction. The polar angle,  $\theta$ , is measured from the positive  $z$ -axis and the azimuthal angle,  $\phi$ , is measured in the  $x$ - $y$  plane.  $\eta = -\ln \tan(\theta/2)$ . The transverse energy and momentum are defined as  $E_T = E \sin \theta$  and  $p_T = p \sin \theta$  where  $E$  is the energy measured in the tracking system.  $E_T^{\text{miss}} = | - \sum_i E_T^i \vec{n}_i |$  where  $\vec{n}_i$  is a unit vector that points from the interaction vertex to the transverse plane.
- [26] “Timing Distribution at the LHC”, B.G. Taylor Colmar, 9-13 September 2002
- [27] “An FPGA based multiprocessing CPU for Beam Synchronous Timing in CERNs SPS and LHC”. *Proceedings of ICAL EPICS 2003, Gyeongju, Korea ICAL EPICS 2003*
- [28] “Timing and Synchronization in the LHC Experiments”, Varela, J. Krakv, 11-15 September 2000.
- [29] <http://ttc.web.cern.ch/TTC/intro.html>
- [30] “Study of the LHC ghost charge and satellite bunches for luminosity calibration.”, CERN-ATS-Note-2012-029 PERF
- [31] “LHC bunch current normalisation for the April-May 2010 luminosity calibration measurements.”, CERN-ATS-Note-2011-004 PERF
- [32] CMS Collaboration, “The electromagnetic calorimeter. Technical design report”,. CERN-LHCC-97-33
- [33] Bo Lofstedt, “The digital readout system for the CMS electromagnetic Calorimeter”, *Nucl. Inst. Methods in Physics Research*, A 453 (2000) 433-439
- [34] CMS Electromagnetic Calorimeter Collaboration, “Energy resolution of the barrel of the CMS Electromagnetic Calorimeter”, JINST 2(2007)P04004.

- [35] CMS Collaboration, “Time Reconstruction and Performance of the CMS Crystal Electromagnetic Calorimeter”, CFT-09-006, 2009.
- [36] <https://twiki.cern.ch/twiki/bin/viewauth/CMS/ECALDPGTimeCalibration>
- [37] <https://twiki.cern.ch/twiki/bin/viewauth/CMS/ECALDPGHWTimeCalibration>
- [38] CMS Collaboration, “The CMS ECAL performance With examples”, JINST 9 C02008, 2014.
- [39] CMS-DP-2014/011: “*ECAL Timing Performance Run1*”
- [40] <https://twiki.cern.ch/twiki/bin/view/CMSPublic/EcalDPGResultsCMSDP2014011>
- [41] <https://twiki.cern.ch/twiki/bin/view/CMSPublic/EcalDPGResultsCMSDP2014012>
- [42] “Characterization and treatment of anomalous signals in the CMS Electromagnetic Calorimeter” CMS AN AN-10-357
- [43] “ Mitigation of Anomalous APD signals in the CMS ECAL”, 2013, *JINST 8 C03020*, W.Bialas and D.A. Petyt
- [44] CMS Collaboration, “CMS trigger and data taking in 2010 ”, *CMS CR-2011/051*.
- [45] CMS Collaboration, “Reconstruction of the signal amplitude of the CMS electromagnetic Calorimeter”, Eur.Phys.J. C46S1(2006)23-35.
- [46] D.del Re et al “An algorithm for the determination of the flight path of long-lived particles decaying into photons” CMS AN -2010/212.
- [47] CMS Collaboration, “Particle-Flow Event Reconstruction in CMS and Performance for Jets, taus and  $\cancel{E}_T$ ”, CMS Physics Analysis Summary CMS-PAS-PFT-09-001(2009).
- [48] CMS Collaboration, Missing Transverse Energy Performance in Minimum-Bias and Jet Events from Proton-Proton Collisions at  $\sqrt{s} = 7$  TeV , CMS Physics Analysis Summary CMS-PAS-JME-10-004 (2010).
- [49] MET JINST (arXiv:1106.5048)

- [50] CMS Collaboration, “Missing transverse energy performance of the CMS detector”; arXiv:1106.5048v1
- [51] CMS Collaboration, “CMS Physics: Technical design report, Volume 2” CERN-LHCC-2006-001.
- [52] CMS Collaboration, “Determination of Jet Energy Scale in CMS with pp collisions at  $\sqrt{S} = 8$  TeV”, *JME-10-010(2012)*
- [53] “<https://twiki.cern.ch/twiki/bin/viewauth/CMS/EGamma2012>.”
- [54] “Parton distributions for the LHC” *Eur.Phys.J C63(2009) 189-285* or arXiv:0901.0002
- [55] CMS Collaboration, “Search for ADD Extra-dimensions with Photon + MET signature”, *AN-11-319(2011)*
- [56] ISAJET 7.84 F.E. Paige, S.D. Protopopescu, H. Baer and X. Tata, <http://www.nhn.ou.edu/~isajet/>
- [57] T. Sj ostrand, S. Mrenna, and P. Skands, PYTHIA 6.4 physics and manual, *JHEP 05 (2006) 026*, doi:10.1088/1126-6708/2006/05/026, arXiv:hep-ph/0603175
- [58] GEANT4 Collaboration, GEANT4a simulation toolkit, *Nucl. Instrum. Meth. A 506(2003) 250*, doi:10.1016/S0168-9002(03)01368-8.
- [59] “Presentation of search results: the CLs technique”, *A. L Read 2002 J. Phys. G: Nucl. Part. Phys. 28 2693*
- [60] “Computation of confidence levels for search experiments with fractional event counting and the treatment of systematic errors”, *Peter Bock JHEP01(2007)080*
- [61] <https://twiki.cern.ch/twiki/bin/viewauth/CMS/>
- [62] “Asymptotic formulae for likelihood-based tests of new physics” *G. Cowan et al, arXiv:1007.1727v3*
- [63] N.-E. Bomark and L. Roszkowski “3.5 keV x-ray line from decaying gravitino dark matter” *Phys. Rev. D 90, 011701(R)* Published 18 July 2014

## Appendix A

# Glossary and Acronyms

Care has been taken in this thesis to minimize the use of jargon and acronyms, but this cannot always be achieved. This appendix defines jargon terms in a glossary, and contains a table of acronyms and their meaning.

### A.1 Glossary

- **Cosmic-Ray Muon (CR  $\mu$ )** – A muon coming from the abundant energetic particles originating outside of the Earth’s atmosphere.
- **SUSY** – A theoretical model based on a fundamental symmetry called supersymmetry in which the fermions and bosons can exchange their spin, extending the standard model to account for the stability in the observed Higgs boson mass and to also predicting the existence of many extra new particles which could be candidates of dark matter.

### A.2 Acronyms

Table A.1: Acronyms

NMLLP	Neutral Massive Long-Lived Particles.
DM	Dark Matter.
DE	Dark Energy.
GMSB	Gauge Mediated Supersymmetry Breaking
LHC	Large Hadron Collider
CMS	Compact Muon Solenoid
CR $\mu$	Cosmic-Ray Muon